FLUX PINNING AND CONNECTIVITY IN POLYCRYSTALLINE HIGH-TEMPERATURE SUPERCONDUCTORS

Cover: Flux penetration at 30 K in a 1.2 µm thick YBCO coated conductor that is produced with metal-organic-deposition. The flux penetration is visualized with magneto-optical imaging when a magnetic field of 70 mT is applied perpendicular to the conductor.

FLUX PINNING AND CONNECTIVITY IN POLYCRYSTALLINE HIGH-TEMPERATURE SUPERCONDUCTORS

PROEFSCHRIFT

ter verkrijging van
de graad van doctor aan de Universiteit Twente,
op gezag van de rector magnificus,
prof. dr. F.A. van Vught,
volgens besluit van het College voor Promoties
in het openbaar te verdedigen
op vrijdag 30 januari 2004 om 13.15 uur

door

Daniël Cornelis van der Laan

geboren op 10 juli 1975
te Rheden

Dit proefschrift is goedgekeurd door:

Prof. dr. ir. H.H.J. ten Kate (promotor),
Dr. ir. B. ten Haken (assistent-promotor).

Contents

1. Introduction

Almost two decades after the discovery of high-temperature superconductors, one could ask why they are only applied on a relatively limited scale. The work presented in this thesis addresses this question by showing why the critical current density of polycrystalline high-temperature superconductors is below expectations when the superconductors are produced in long lengths. The effect of the granularity of polycrystalline superconductors on the current carrying capabilities is dealt with in the first part of this thesis. In the second part, the role of flux pinning and the influence of grain boundaries are discussed. The results contribute to a better understanding of current flow in high-temperature superconductors, which hopefully supports the development of conductors with an increased quality.

1.1. High-temperature superconductors

Large magnets as for instance for accelerators, detectors, MRI-, NMR- and SMES-systems are build from low-temperature superconductors. Low-temperature superconductors have a transition temperature below 30 K (table 1.1) and are mostly cooled with liquid helium, although cryocoolers can cool the conductor in some applications where in particular Nb_3Sn is used. High critical current densities at 4.2 K in the presence of a magnetic field can be achieved as 3 kA/mm^2 at 5 T for NbTi. Nb_3Sn carries this current density at 12 T. The applications are limited to magnetic fields below the upper critical field: 10.4 T for NbTi and 21-26 T for Nb_3Sn.

System	Conductor	Critical temperature [K]	Upper critical field B_{c2} at 4.2 K [T]	In-plane coherence length $\xi(0)$ [nm]	Critical current density [kA/mm^2]
NbTi	Wire	9.8	10.4	4	3 (4.2 K, 5 T)
Nb_3Sn	Wire	18.1	21-26	3	3 (4.2 K, 12 T)
$Bi_2Sr_2Ca_2Cu_3O_x$	Tape	110	> 100	1.5	3 (4.2 K, 0 T)
$Bi_2Sr_2CaCu_2O_x$	Tape	92	> 100	1.5	5 (4.2 K, 0 T)
$YBa_2Cu_3O_x$	Coated conductor	92	> 100	1.5	200 (4.2 K, 0 T)

Table 1.1. Properties of various low- and high-temperature superconductors for large scale applications.

Ceramic superconductors with critical temperatures above the boiling point of liquid nitrogen were discovered soon after the discovery of superconductivity in $LaBa_2CuO_x$ at about 30 K by Bednorz and Müller in 1986 [1]. Among the copper-oxide high-temperature superconductors are $YBa_2Cu_3O_x$ with a critical temperature (T_c) of approximately 93 K, $Bi_2Sr_2CaCu_2O_x$ (T_c~92 K), $Bi_2Sr_2Ca_2Cu_3O_x$ (T_c~110 K), $HgBa_2Ca_2Cu_3O_x$ (T_c~135 K) and $Tl_2Ba_2CaCu_2O_x$ (T_c~118 K).

Since the discovery of high-temperature superconductors, applications at higher temperatures are possible due to the elevated critical temperatures of these superconductors. Liquid nitrogen with a boiling point of 77 K can be used as coolant, which makes large scale applications more attractive. High-temperature superconductors can be applied to replace copper in for instance generators, transformers and power transmission cables and therefore reduce energy loss significantly. Due to the resistive nature of the normal-conducting metals Cu and Al, about 6 % of electrical loss occurs with the production and transportation of electrical power. It is estimated that replacement of Cu-based technology with superconducting devices will decrease the loss by half,

representing an enormous energy saving and having corresponding environmental benefits. Applications as for instance motors, generators and transformers can be made more compact with high-temperature superconductors, due to the high critical current densities already obtained (table 1.1).

For applications in magnetic fields above 25 T, high-temperature superconductors are the only candidates because they have an upper critical field higher than 100 T at 4.2 K. Applications as high-field NMR (25-30 T at 4.2 K), but also applications that operate at intermediate magnetic fields at a temperature range of 20-30 K are now possible.

In order to make ceramic copper-oxide superconductors technically and economically suitable for the applications mentioned above, it has to be available in long lengths. The complex polycrystalline nature of the material makes the formation of extended current paths challenging. Special procedures are developed in order to obtain wires and tapes that are able to carry a supercurrent across several meters. Nowadays, long lengths of $Bi_2Sr_2CaCu_2O_x$ (Bi-2212) and $Bi_2Sr_2Ca_2Cu_3O_x$ (Bi-2223) tapes are produced by the oxide-powder-in-tube method [2]. Silver or silver-alloy tubes filled with precursor powder are drawn into wires, stacked in a multifilament configuration and rolled into a tape (figure 1.1). The image of the cross section of a 4 mm wide tape with 65 superconducting filaments is shown, together with stainless steel strips that are soldered on both sides of the tape for an improved mechanical strength. The superconducting phase is formed when the tape is heat treated at around 800°C in an oxygen atmosphere. $YBa_2Cu_3O_x$ coated conductors (YBCO CC), on the other hand, are produced as thin films on a buffered metal substrate [3]. Although very high critical current densities can be obtained (table 1.1), the multi-layer configuration with low deposition rates results in a difficult and expensive production.
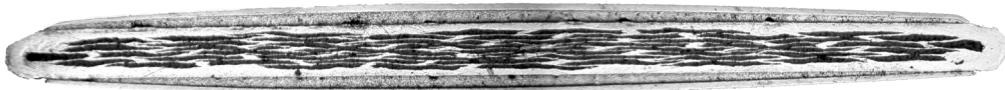
Figure 1.1. Optical photograph of the cross-section of a 4 mm wide Bi-2223 tape.

The required multi-layer structure makes the production of YBCO coated conductors rather difficult and expensive, while the connectivity in Bi-based tapes is estimated to be below 10 % of its maximum. The price/performance ratio of Bi-based tapes and YBCO coated conductors can be further improved by increasing the critical current density of the conductor and improving the production process. Therefore it is crucial to understand how the critical current density is limited by for instance grain-to-grain connectivity and flux pinning.

1.2. Motivation and goal

The granularity of polycrystalline high-temperature superconductors gives rise to a poor grain-to-grain connectivity, which results in a rather complex network of current paths. The critical current density is limited significantly because current is carried by a small fraction of the available conductor cross-section.
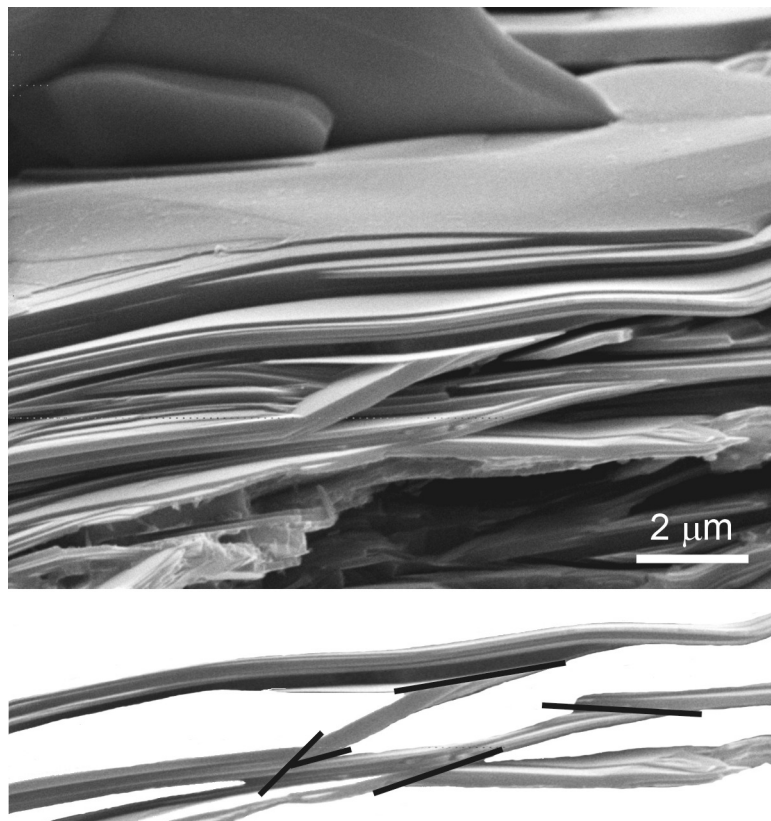
Figure 1.2. SEM-image of the grain structure of a typical high-quality Bi-2223 tape. Part of the grain structure is shown below the SEM-image where two different types of current paths are outlined. Long chains of well-connected grains are observed, together with a network of grains that are connected at low- and high-angles (black lines). Courtesy of R. Passerini.

The rather complex granular structure becomes evident when the cross-section of a high-quality Bi-2223 tape is visualized with SEM (figure 1.2). A large number of grains is observed that are connected at low- (4-10 degrees) and high-angles (> ~10 degrees). Also large grain structures that are connected at angles smaller than 4 degrees are

observed. In-plane connectivity is important for high critical current densities because polycrystalline high-temperature superconductors have a very small coherence length in the *c*-direction, compared to the dimensions of the grains [4] (table 1.1). A transport current that runs from left to right in the image will be largely carried by chains of well-connected grains as outlined in figure 1.2. Current in the network of grains that are connected at a higher angle is largely suppressed at the grain boundaries [5].

The importance of the grain-to-grain connectivity for substantial critical current densities in high-temperature superconductors becomes evident when the increase in conductor performance over the years is regarded. In the early 90's, bulk samples of YBCO were developed. Although this was the first step towards the development of conductors for large-scale applications that are operated at liquid nitrogen temperature, their in-field performance was rather disappointing [6]. A sharp decrease in critical current density as function of magnetic field is observed (figure 1.3). This is attributed to a poor connectivity of the individual grains in the conductor. A supercurrent has to cross a large number of low- and high-angle grain boundaries due to the absence of chains of well-connected grains. High-angle grain boundaries have poor current-carrying capabilities, especially when a magnetic field is applied.
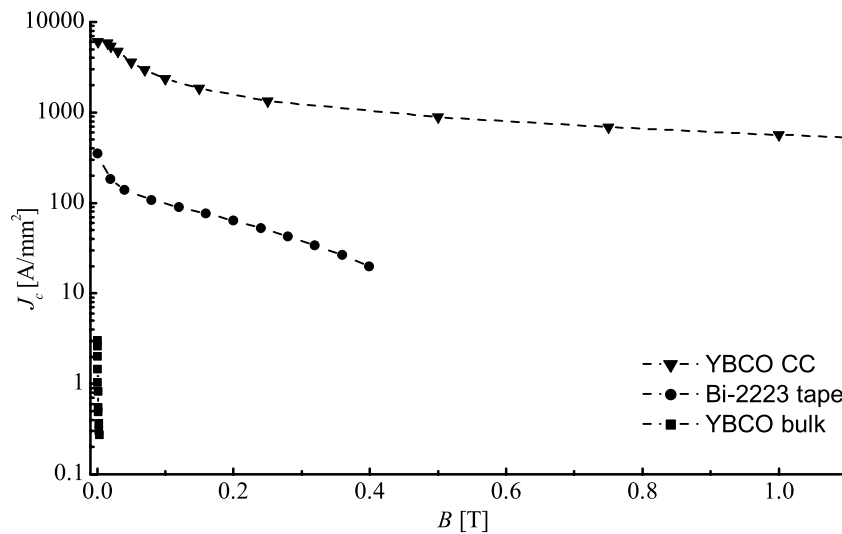
Figure 1.3. Critical current density versus magnetic field of an early YBCO bulk sample, a high-quality Bi-2223 tape and YBCO coated conductor at 77 K. The magnetic field is applied perpendicular to the wide side of the tape. The dashed lines are a guide to the eye.

A refinement of the production process results in a better connectivity in Bi-based tapes [7]. The *c*-axis texture required for good connectivity has improved rather quickly. Chains of well-connected grains can sustain a supercurrent even when a magnetic field of 0.4 T is applied at 77 K (figure 1.3). Although high-field applications

will be operated around 4.2 K, the temperature of 77 K in this example is chosen because the effect of grain connectivity can be observed within a relatively small magnetic field at this temperature. The grain-to-grain connectivity is improved even further in YBCO coated conductors [8]. The in-plane texture that is required in this type of conductor is difficult to obtain but is made possible due to improvements in thin film deposition technology. The effect of a high degree of connectivity is reflected by the small field-dependence of the critical current at high field (figure 1.3). Although the critical current density of YBCO coated conductors is over one order of magnitude higher than that of Bi-2223 tapes, the overall critical current is comparable. The thickness of the superconducting layer in YBCO coated conductors ranges from 0.4 to 2 μm on a 50 μm thick substrate, resulting in a relatively low filling factor of 1-2 %, while the filling factor of Bi-2223 tapes exceeds 40 %.

The first goal of this thesis is to investigate how grain connectivity on a micrometer scale influences the critical current density over several millimeters of length in polycrystalline high-temperature superconductors. The second goal is to verify whether the behavior of the critical current density can be related to known mechanisms as flux pinning and Josephson behavior. Is the critical current density limited by flux motion in the grains, at the grain boundaries, or due to Josephson behavior at high-angle grain boundaries? The third goal is to study how the mechanisms that limit the critical current density in polycrystalline high-temperature superconductors can be affected. Does a coupling between different mechanisms exist? The fourth goal is to verify whether a model can be developed, based on the results obtained with Bi-2223 tapes, that describes current flow in polycrystalline high-temperature superconductors in general.

1.3. Scope of this thesis

The main objective of this work is to study the mechanisms that limit the critical current density in polycrystalline high-temperature superconductors. Several new experimental methods are combined in order to obtain a detailed understanding of how a macroscopic supercurrent is influenced by local variations in critical properties. The formation of multiple current paths as a result of a poor grain-to-grain connectivity is studied. The effect of grain boundaries on flux pinning and how flux pinning affects the macroscopic critical current density is investigated.

In chapter *two*, several techniques are introduced to study the behavior of the critical current density of polycrystalline high-temperature superconductors on length scales ranging from 5 μm to 10 mm. A combination of novel techniques is used to investigate the influence of grain connectivity and flux pinning on the critical current density. The spatial variations in critical current density are measured on a macroscopic

level with the so-called "magnetic knife", while flux penetration on a micrometer scale in the grain structure of high-temperature superconductors is visualized with "magneto-optical imaging".

In chapter *three*, the correlation between grain connectivity and macroscopic critical current density in YBCO coated conductors and Bi-based tapes is investigated. The results obtained with the magnetic knife and with magneto-optical imaging are combined to extract the influence of large defects and of concentrations of grain boundaries on the macroscopic critical current density of YBCO coated conductors. The weak links in the current path of Bi-based tapes are located indirectly by combining magneto-optical imaging and the application of tensile strain. This combination of experimental techniques is applied to relate the similarities and differences between Bi-based tapes and YBCO coated conductors to their structure and production method.

In chapter *four*, several theoretical models that describe dissipation in Bi-2223 tapes are studied to reveal what mechanisms limit the critical current density in these tapes. The magnetic field, temperature and field angle-dependence of the critical current density of carefully selected samples are studied to reveal the influence of flux pinning and of the Josephson effect.

In chapter *five*, it is investigated how the mechanisms that limit the critical current density in Bi-2223 tapes can be influenced. Also the interaction between individual mechanisms is studied. Finally, it is investigated whether the knowledge regarding the mechanisms that limit the critical current density in Bi-2223 tapes is applicable to polycrystalline high-temperature superconductors in general.

In chapter *six*, the conclusions regarding the influence of flux pinning and connectivity in polycrystalline high-temperature superconductors are presented.

2. Experimental techniques and sample preparation

The techniques that are applied throughout this thesis to study the influence of for instance grain connectivity and flux pinning on the critical current density of polycrystalline high-temperature superconductors are presented in this chapter. Existing techniques including transport and dc-magnetization methods are applied to measure the dependence of the macroscopic critical current density on magnetic field, temperature and applied strain on the average length scale of 5-10 mm. Variations in critical current density due to poor grain connectivity are studied by more advanced techniques. The spatial distribution in macroscopic critical current density across the width of the conductor is measured with the magnetic knife method over several millimeters with a resolution of 50-100 μm. The variations in local critical current density are then related to the grain structure of the conductor by studying flux penetration with magneto-optical imaging on a length scale of approximately 5 μm. The correlation between grain structure and variations in macroscopic critical current density is obtained by combining the results of both techniques.

2.1. Macroscopic critical current density

Existing techniques to measure the dependence of the macroscopic critical current (I_c) of $Bi_2Sr_2Ca_2Cu_3O_x$ (Bi-2223) tapes and $YBa_2Cu_3O_x$ (YBCO) coated conductors (table 2.1) on magnetic field, temperature and axial strain on a length scale of 5-10 mm are introduced. The dependence of the critical current density on magnetic field and temperature is measured using both transport and dc-magnetization methods. The effect of applied longitudinal strain on the grain structure and on the critical current of Bi-based tapes and YBCO coated conductors is studied in chapter 3 and is measured with the transport current method.

	Superconductor	Matrix/ Substrate	Filament #/ Layer thickness	Production method	I_c at self-field [A]
B-5	$Bi_2Sr_2Ca_2Cu_3O_x$	Ag	19	PIT	65 (77 K)
T-1	$Tl_2Ba_2CaCu_2O_x$	$LaAlO_3$	1.2 µm	Sputtering	-
T-2	$Tl_2Ba_2CaCu_2O_x$	$LaAlO_3$	0.3 µm	Sputtering	-
H-1	$HgBa_2Ca_2Cu_3O_x$	Ag	-	PBS	-
Y-1	$YBa_2Cu_3O_x$	Ni	0.4 µm	PLD	15 (77 K)

Table 2.1. Selected properties of the samples studied in chapter 2.

2.1.1. Transport critical current as function of field and temperature

A four-probe method is applied to determine the critical current of Bi-based tapes and YBCO coated conductors with the transport method. A transport current runs through the sample while the voltage across the sample is measured simultaneously. Superconducting samples are mounted on a brass sample holder, which provides sample support and a relatively large thermal mass for a stable sample temperature. Bi-based tapes are soldered to the sample holder with indium solder at 450 K, while YBCO coated conductors are glued at 300 K. A transport current is introduced in the sample by soldering current leads to both ends of the conductor and is measured with an accuracy of 0.01 % using a zeroflux current meter. The voltage across the sample is measured with an accuracy of approximately 1 nV. The voltage taps are soldered in between the current leads with a typical spacing of one centimeter. The voltage taps are located at least one centimeter away from the current leads, to ensure that the measured voltage is not significantly influenced by the voltage required for current transfer.

The temperature of the sample holder is varied to measure the critical current between 4.2 K and 110 K. The sample and sample holder are placed underneath a kapton cup that is emerged in liquid cryogen, creating a gas environment around the sample [9]. The temperature of the sample is controlled by two heaters that are located at both legs of the sample holder (figure 2.1). Temperature sensors located at both sample ends provide the feedback for the temperature controller that powers the heaters. It is ensured that the temperature gradient across the sample is kept below 0.5 K by balancing both heaters independently. The gradient arises from a difference in Ohmic heating in both current leads. The sample temperature at the location of the voltage taps is measured with an accuracy of 0.1 K using a third temperature sensor.
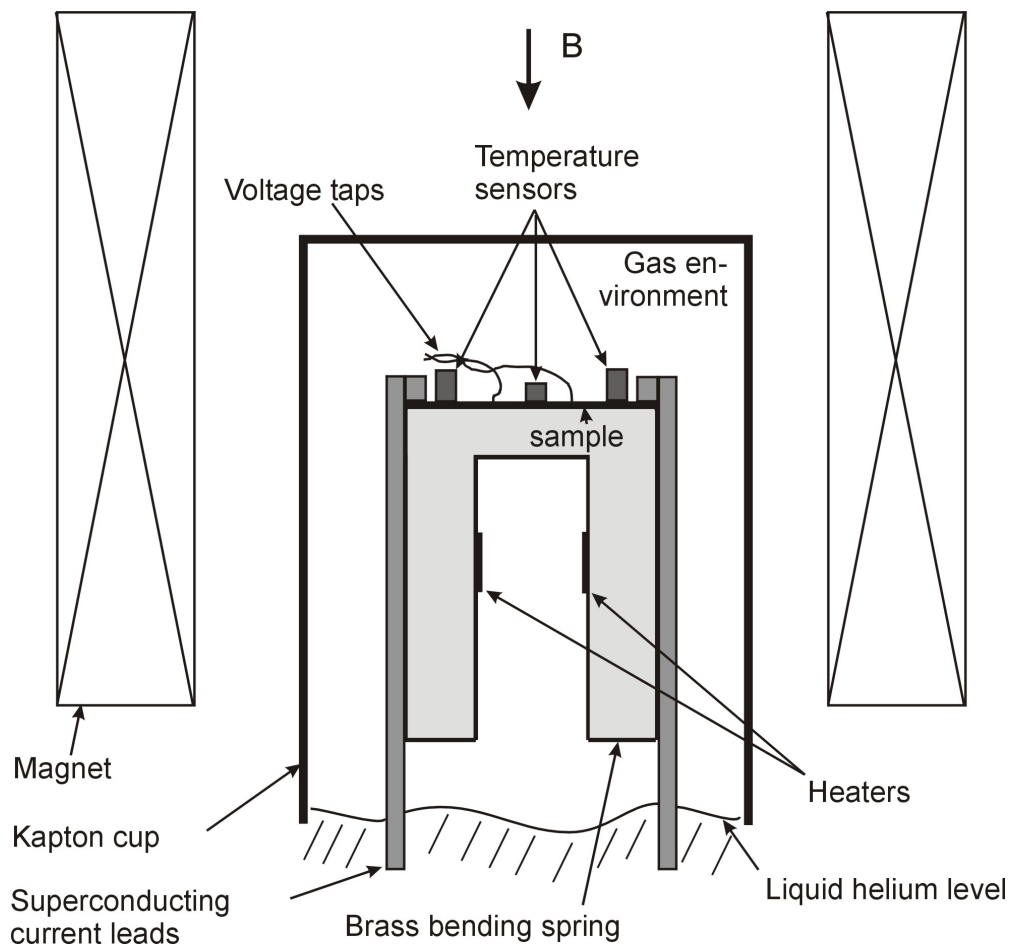
Figure 2.1. Setup to measure the critical current of superconducting tapes as function of magnetic field and temperature. A gas environment insulates the sample and sample holder from the liquid cryogen that surrounds the Kapton cup.

The critical current of the sample is measured as function of magnetic field by applying a maximum field of 8 T with a superconducting magnet for sample temperatures below 77 K. Liquid helium is used to cool the sample in this temperature range. For the temperature range above 77 K where liquid nitrogen is used as cryogen, a maximum field of 400 mT is applied by a copper magnet. The magnetic field is applied either perpendicular or parallel to the wide side of the sample but always perpendicular to the transport current. The uncertainty in magnetic field is due to the misalignment of the sample with the applied field and the hysteresis of the magnet. Its value is estimated at 0.3 % (misalignment of 4 degrees), with a minimum of 2 mT for the superconducting magnet and 1 mT for the copper magnet.

The critical current as function of field for different temperatures is measured within 1% accuracy by the following procedure. The sample is cooled in zero field to the temperature at which the experiment takes place. The magnetic field is first ramped to its maximum value and back to zero to ensure that the sample is no longer in its virgin state. The critical current is now determined by measuring the voltage across the sample as function of current as is shown in figure 2.2 for sample B-5 at 30 K. The properties of the sample are listed in table 2.1. The current is increased stepwise until the voltage per meter exceeds the electric field of 1×10^{-4} V/m. A correction is applied for the voltage offset in the experiment before the critical current is determined. This procedure is repeated at various magnetic fields, for increasing and decreasing field, at selected temperatures within the desired temperature range.
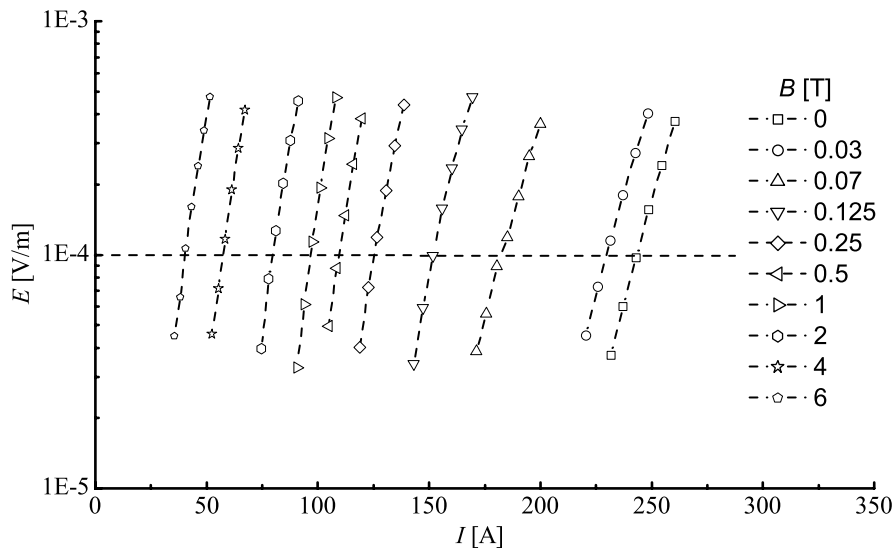
Figure 2.2. Electric field versus current characteristics of sample B-5 at 30 K for various magnetic fields. The dashed lines through the data points are a guide to the eye, while the horizontal dashed line is the electric field criterion.

2.1.2. Transport critical current as function of applied strain

The dependence of the critical current on longitudinal strain is measured with a four-probe method on a length scale of 5-10 mm. Longitudinal strain is applied after Bi-based tapes are soldered and YBCO coated conductors are glued to a brass U-shaped bending spring [10]. The critical current is measured in a similar way as is described in the previous section by soldering current leads and voltage taps on top of the sample (figure 2.3). The bending spring with sample is inserted in a cryostat, where the sample is strained in liquid nitrogen at 77 K or in liquid helium at 4.2 K. Strain is applied to the sample by bending the legs of the bending spring inwards, using a stepper motor. The strain of the sample is measured with an accuracy of 0.02% [11], using two strain gages that are glued to the sample holder.

Thermometer

Strain gage

Tape

Sample Holder

Strain device

45

Strain Adjustment
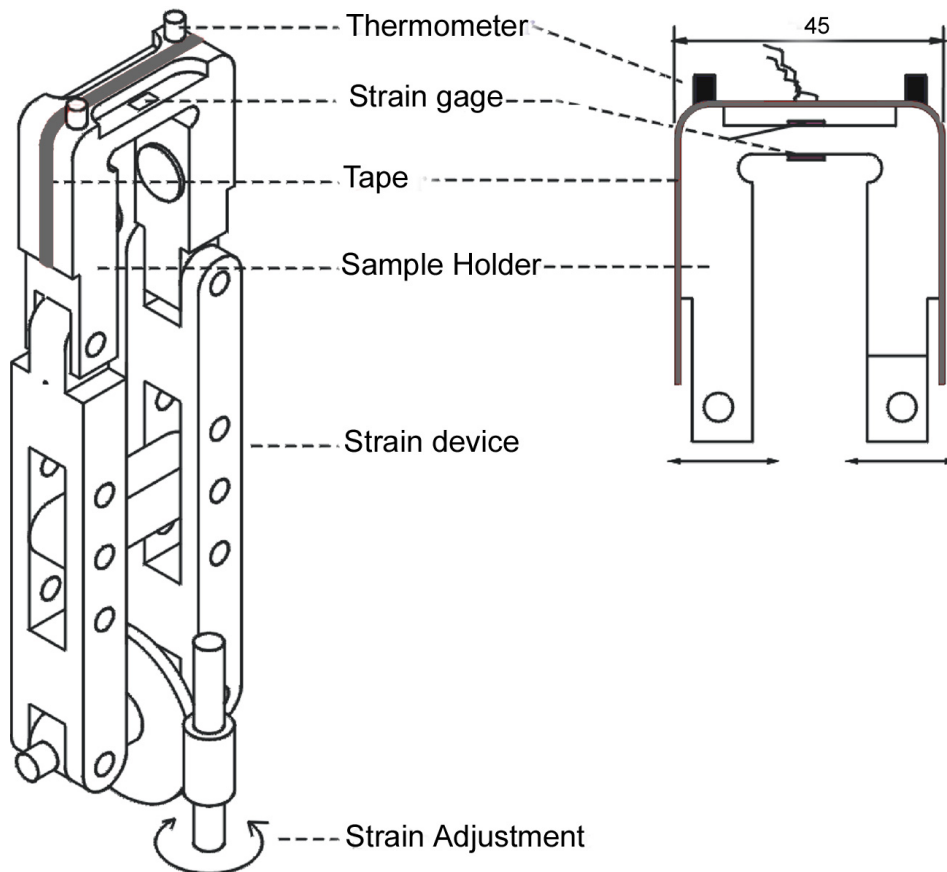
Figure 2.3. Bending spring with brass sample holder where strain is applied to superconducting tapes at different temperatures.

2.1.3. Dc-magnetization

Next to the transport method, the dependence of the critical current density (J_c) of technical high-temperature superconductors is obtained using the dc-magnetization method. This method is selected because of several advantages over the transport method. Much smaller samples can be studied because there is no need for the attachment of current leads and voltage taps. Furthermore, all superconducting parts of the sample contribute to the magnetic moment, while with the transport method only chains of connected grains that form an uninterrupted current path determine the critical current density.

The magnetic moment of superconducting samples is measured using in a SQUID magnetometer with a sensitivity for the magnetic moment as low as 1×10^{-4} A/m, in a temperature range of 4.2 K to room temperature (0.5 % accuracy). A magnetic field up to 5.5 T is applied to the sample with field homogeneity of 0.01 % in a 4 cm long sample space. The accuracy of the applied magnetic field depends on the alignment of the sample and is estimated to be within 0.5 %, with a minimum of 2 mT due to the hysteresis in the magnet. Samples with a maximum size of 5 mm by 5 mm are inserted in the system, after they are glued to an aluminum disk. In the case of Bi-based tapes, several pieces are glued on top of each other to increase the overall magnetic moment.
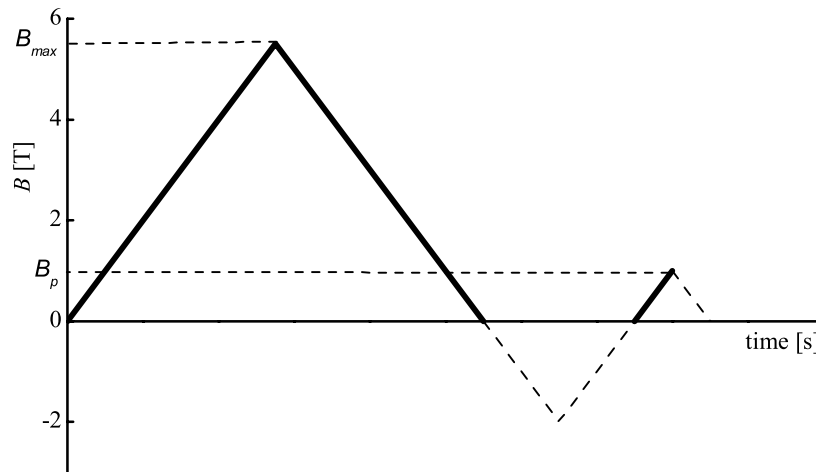
Figure 2.4. Applied magnetic field as function of time during the measurement of the magnetic moment. The solid lines indicate the parts of the field excursion where the magnetic moment is measured.

In order to measure the magnetic moment as function of magnetic field and temperature accurately and reproducibly, the following steps are taken. First the magnetic flux that is trapped in the sample while it passed through the magnet during insertion is

released by warming the sample to above its critical temperature. The sample is now in its virgin state. The sample is then cooled to the temperature at which the experiment takes place, and the magnetic moment of the sample is measured stepwise as function of field for increasing and decreasing field (solid lines in figure 2.4). The magnetic moment is measured in a time frame of three seconds after the magnetic field has reached the desired value.

After the maximum magnetic field value is reached, the magnetic moment of the sample is measured for decreasing field. A magnetic field of 2 T is applied in the opposite direction, to completely reverse the field profile in the sample after the field is switched off. The magnetic moment of the sample is again measured for the same magnetic field values for increasing field as in the virgin state, until the magnetic field has reached a value larger than the penetration field (B_p) of the sample (figure 2.5). This is the magnetic field at which the magnetic moment of the sample in the non-virgin run is equal to the one in the virgin run. The field at which the irreversible magnetization vanishes is the irreversibility field (B_{irr}) [12], and is defined as the field at which the irreversible magnetization becomes smaller than 0.01 A/m. The sample no longer has the ability to carry a supercurrent above this field. The irreversibility field of sample B-5 at 40 K is 3.4 T, while at 15 K, B_{irr} is located outside the experimental range (> 5.5 T).

The measurement is stopped after completion of the field sweep. The magnetic field is switched off and the sample is warmed to above its critical temperature. After the trapped flux is released, the sample is cooled to the next temperature after which the magnetic moment is measured as function of field, following the same procedure.
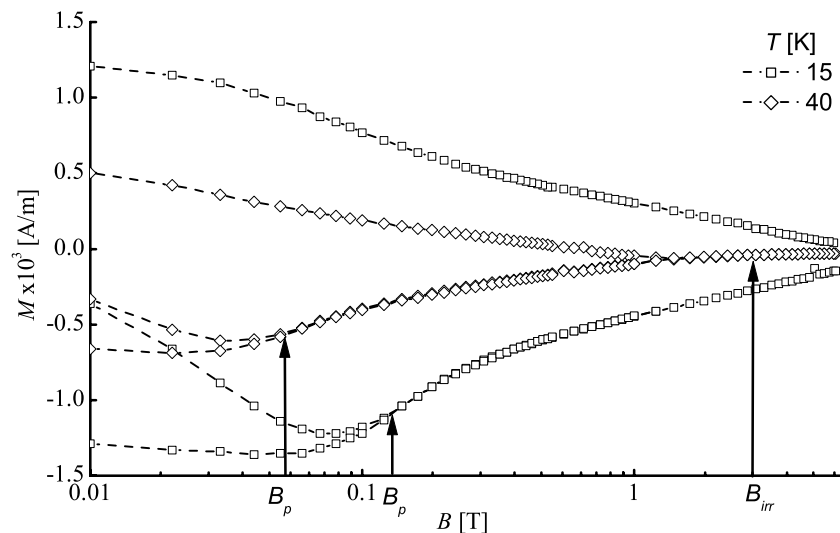
Figure 2.5. Magnetic moment of sample B-5 as function of magnetic field at 15 K and 40 K. The magnetic field is applied perpendicular to the tape surface. The dashed lines are a guide to the eye.

The overall critical current density of the sample is obtained from the irreversible magnetization for magnetic fields above the penetration field. Although the exact value of the irreversible magnetization depends strongly on the sample size and shape, its (relative) field and temperature dependence above the penetration field is determined by the behavior of the critical current density with magnetic field and temperature.

An important difference between the transport and magnetization methods is the electric field across the sample at which the experiment takes place. With the transport method, the critical current is defined as the current at which the voltage across the sample equals the voltage criterion (in our case 10^{-4} V/m). In the case of dc-magnetization, the electric field across the sample at which the magnetic moment is measured is lower. The exact value is related to flux creep and depends on the time in between the field change and the measurement. A time scale of three seconds, as is the case for the experiments in this thesis, results in an electric field of roughly 10^{-5} V/m [13].

2.2. Magnetic knife

The spatial distribution in macroscopic critical current density of YBCO coated conductors is obtained with the magnetic knife technique. This is a first step to study the influence of grain connectivity on the macroscopic critical current density. Variations in critical current density across the width of the sample can be determined with a resolution of 50 μm.

The critical current is measured with a standard four-probe technique which results in an averaging of the variations in critical current density over 1-5 mm along the tape length. The resolution with which variations are determined across the sample width depends on the sharpness of the knife and is in the order of 50 μm. The magnetic knife suppresses the critical current density in most of the sample with an applied magnetic field. The extent of the suppression depends on the magnetic field dependence of the critical current density, which is measured in the same setup in which the magnetic knife experiment is performed. The magnetic field is applied perpendicularly to the sample surface by a copper magnet that generates a magnetic field up to 200 mT. Sample damage due to temperature shocks and soldering is kept to a minimum by using the same sample holder, and moving the sample directly in the magnetic knife after the critical current density as function of applied field is measured.

The magnetic knife produces a field profile that leaves a narrow path along the conductor length for a transport current to pass through the sample. The critical current density is largely suppressed, except for a local area where the profile goes through zero. The macroscopic critical current density is largely determined by the properties of the conductor at the location of the narrow path [14]. The field profile is created by two

copper coils that are wound around two iron cores (figure 2.6a). The profile switches from a relatively large positive value to a relatively large negative value in a narrow region (figure 2.6b).
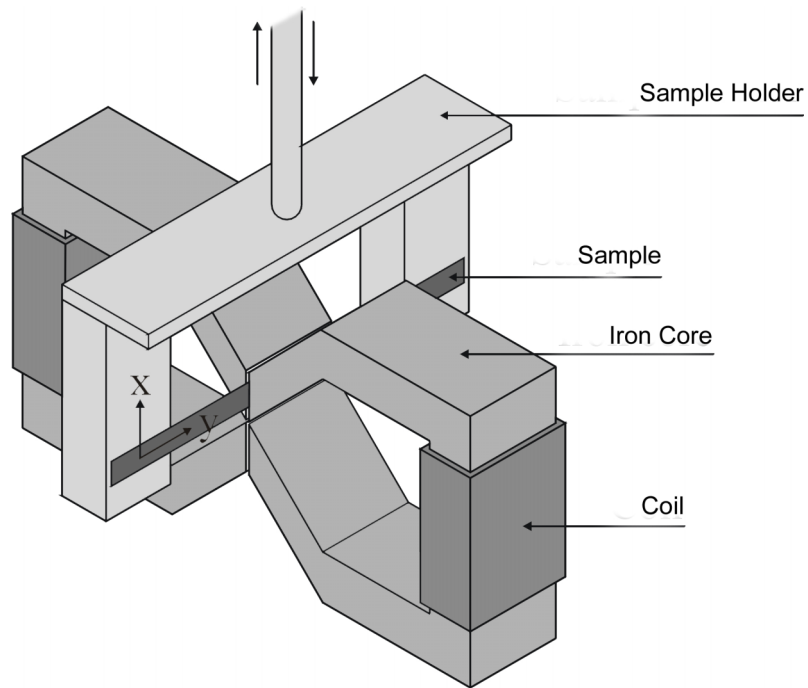
Figure 2.6. a) Magnetic knife with sample and sample holder.
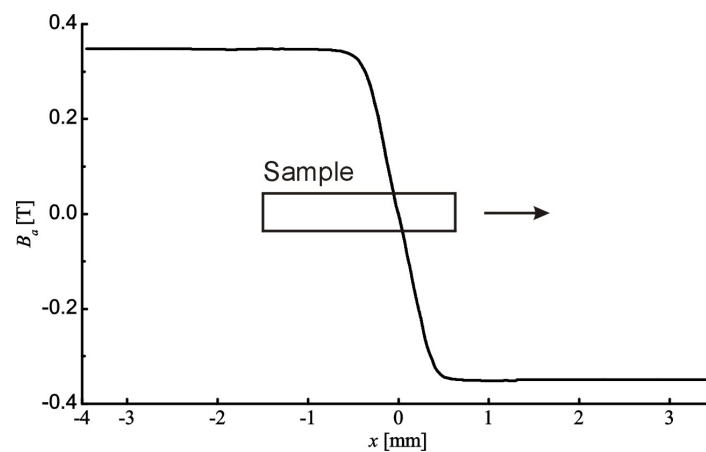
Figure 2.6. b) Field profile within the magnetic knife.

YBCO coated conductors move between both cores with steps of 50 μm and thus pass through the field profile. The critical current density is measured after each step. Current is introduced by soldering the sample to the sample holder using low temperature indium/bismuth solder at 400 K. The solder is applied on a hot plate to the 1-2 μm thick silver cap layer that is deposited on top of the YBCO layer. Voltage taps are glued to the silver cap layer using silver paste. Care is taken that the sample is mounted straight on the holder to prevent it from rubbing against the iron core of the magnetic knife.

The critical current as function of position x of the sample is measured by a four-point measurement at 77 K. In this case, x is the position along the tape width where the field profile goes through zero. Large variations in critical current are measured across the width of for example YBCO coated conductor Y-1 (figure 2.7). The sample details are listed in table 2.1. The results will be analyzed in more detail in section 3.2. The non-zero values of I_c at the edges of the sample are due to the fact that the magnetic field between the iron cores suppresses the critical current density only to some extend.
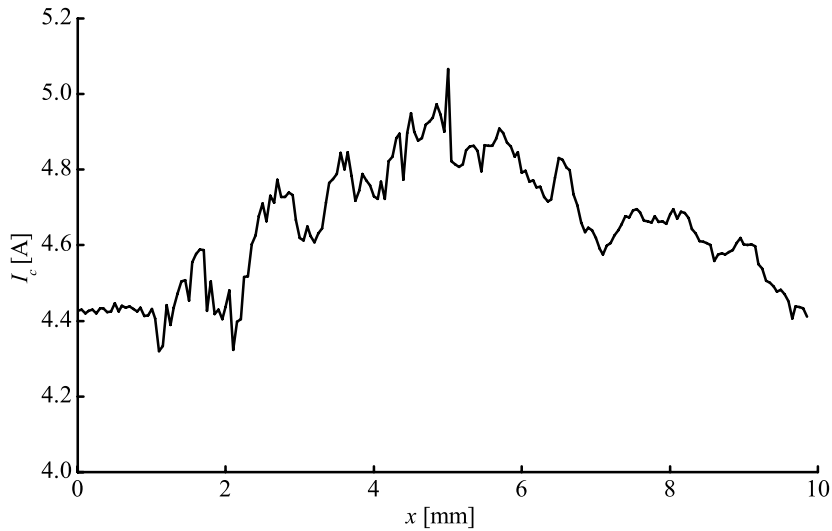
Figure 2.7. Distribution in critical current of YBCO coated conductor Y-1 across the tape width measured with the magnetic knife at 77 K.

For the analysis of the results of the magnetic knife experiments it is assumed that the YBCO layer is thin and that the critical current density is z-invariant (z being the direction perpendicular to the tape surface). The distribution in critical current density is obtained from the spatial variation in critical current. The critical current is defined as:

$$I_c = \int\limits_{-w/2}^{w/2} d(x) J_c(x, B) dx, \tag{2.1}$$

where w is the width of the sample, and $d(x)$ is the thickness of the superconducting layer at position x. A constant thickness is assumed in case of YBCO coated conductors, which have a thin superconducting layer that does not vary in thickness.

The critical current density as function of x_0 is defined by the deconvolution integral, given by equation 2.2. In this case, x_0 is the location in the sample where the applied field B_a is zero.

$$I_c(x_0) = \int\limits_{-w/2}^{w/2} d(x) J_{c0}(x) j_c(B_a(x - x_0)) dx$$

$$= \int\limits_{-w/2}^{w/2} d(x) J_{c0}(x) g(x - x_0) dx. \tag{2.2}$$

The response function (g) is created in order to obtain the distribution in critical current density from the measured critical current over the width of the sample. The response function is needed because the critical current density in the tape is only partly suppressed by the local magnetic field in the knife and the field profile is not perfectly steep. It is obtained by using the field profile over the width of the sample and the field dependence of the critical current density on magnetic field.

2.3. Magneto-optical imaging

Magneto-optical imaging (MOI) is applied to study the influence of the grain connectivity on the microscopic critical current density of polycrystalline high-temperature superconductors with a spatial resolution of approximately 5 μm and a resolution in magnetic field of 10 μT. A direct correlation between local grain connectivity and variations in macroscopic critical current density is obtained. A method to average the variations in microscopic critical current density over a length scale of several millimeters is presented. The method is based on a feature of magneto-optical imaging to distinguish between trapped and returning flux in the grain structure of YBCO coated conductors. Changes within the grain structure of high-temperature superconductors due to the application of longitudinal strain and the influence on the critical current density are studied real-time with magneto-optical imaging. A detailed

description of the experimental setup that includes the strain apparatus as well as of the sample preparation is presented.

2.3.1. Experimental setup used with MOI

Magneto-optical imaging is based on the Faraday Effect and is applied to visualize magnetic fields on a microscopic scale in superconducting samples non-destructively. An indicator film, existing of a thin layer of $(Y,Bi,Pr,Lu)_3(Fe,Ga)_5O_{12}$ deposited on a Gadolinium Gallium Garnet substrate [15,16], is pressed on the sample under investigation. The whole is illuminated with a source of polarized white light and the light reflected from the substrate is recorded through a microscope. The angle of polarization of the reflected light is rotated in the presence of a magnetic field perpendicular to the indicator film. The angle of polarization of the reflected light is rotated over α degrees in a magnetic field B_z perpendicular to the film and is largely determined by the Verdet constant V of the indicator film of thickness d:

$$\alpha = VB_z 2d .$$
(2.3)

The local magnetic field in the superconductor is obtained from the intensity of the reflected light. The intensity of each image is calibrated by applying a known magnetic field (accuracy 0.5%) and measuring the intensity of the reflected light some distance from the sample. The calibration takes the effect of reflections within the cryostat and the microscope into account. The magnetic field inside the sample is calculated with expression 2.3, after the calibration is performed.

Superconducting samples are cooled below their critical temperature within a helium flow cryostat, in which their temperature is regulated. The cryostat contains a vacuum space in which the sample holder is cooled by a mixed flow of cold helium gas and liquid (figure 2.8). A vacuum of at least 3×10^{-3} mbar is required to insulate the cold sample holder from the warm environment outside the cryostat.

The upper part of the sample holder where the sample is mounted on is connected to the cold base by a sapphire neck (figure 2.9). The temperature of the sample is regulated by a temperature controller that powers a heating wire. The temperature is measured with a diode and can be changed from room temperature to approximately 25 K. The minimum temperature depends on the pressure in the helium dewar at the input of the cryostat. The liquid helium consumption is limited to 1 liter per hour due to the high flow resistance of the helium channel. Pressure variations in the channel cause the temperature to oscillate around its set point with amplitude of approximately 1 K.
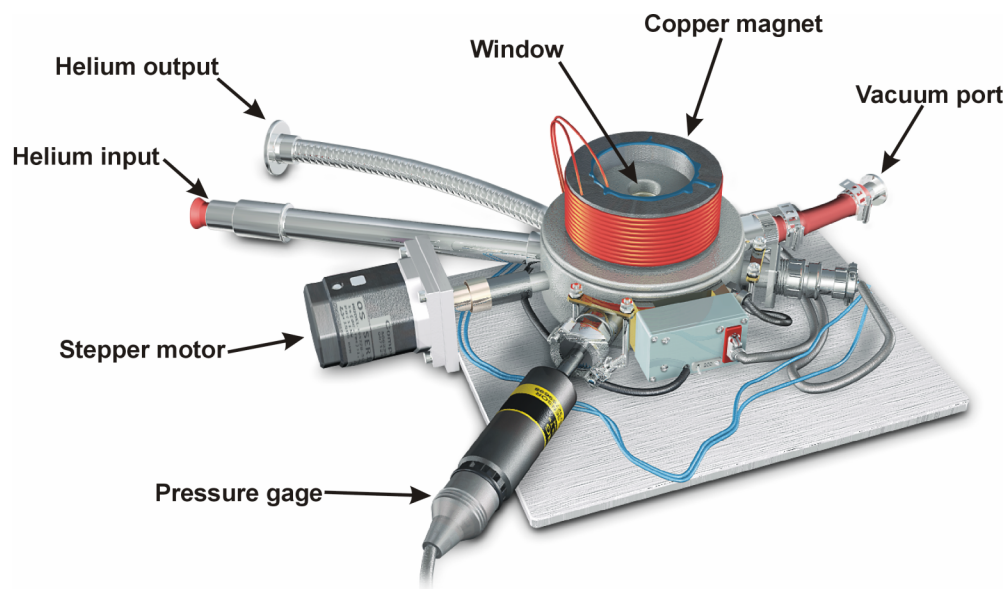
Figure 2.8. Helium flow-cryostat in which the superconducting samples are cooled for the MOI experiments. The cryostat and magnet are placed under a microscope.
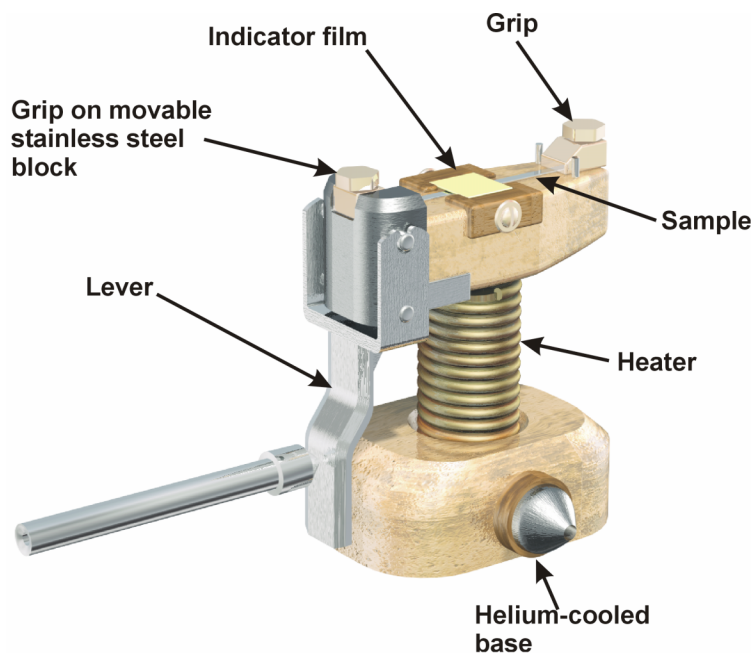
Figure 2.9. Sample holder containing a strain apparatus, heater and temperature sensor. The indicator film is placed on top of the sample.

A magnetic field of up to 120 mT is applied perpendicular to the sample surface by a copper magnet located on top of the cryostat. The cryostat together with sample and indicator film is placed under a microscope with a digital camera for the imaging part of the setup.

Strain to the conductor is applied inside the cryostat, while the change in magnetic field in the sample is observed with MOI. The sample is clamped between one stationary grip and one movable grip, which slides along a rail and is operated by a lever. The lever is driven by a stepper motor. The applied strain is measured with a strain gage on the sample, as explained in section 2.4. The formation of cracks in the ceramic grain structure is observed by a change in the flux pattern when shielding currents are interrupted due to the breaking of superconducting current paths (chapter 3).

2.3.2. Flux trapping and shielding

The ability of MOI to visualize magnetic flux in superconductors is used to study the correlation between grain connectivity and local critical current density in technical high-temperature superconductors. The different aspects of flux trapping and shielding in type-II superconducting samples are explained to demonstrate the possibilities of the technique.

Superconducting shielding currents cancel the field in the interior of type-II superconductors when an external magnetic field is applied. Magnetic flux starts to penetrate the bulk of the superconductor after the field exceeds the lower critical field. The distance over which the magnetic field penetrates the sample is related to the local critical current density [17]. Part of the flux that entered the superconductor remains trapped when the magnetic field is removed. The flux profiles in the superconductor are visualized with MOI.

A typical experiment where flux is visualized with MOI starts with mounting the sample on the sample holder at room temperature. To ensure a good thermal contact, the samples are either clamped at both ends in the grips of the sample holder, or glued to the sample holder with silver paste. After the indicator film is placed on top of the sample, the cryostat is closed and evacuated. The sample is cooled to the desired temperature and a magnetic field is applied perpendicular to the sample surface.

An example of flux shielding in type-II superconductors is presented in figure 2.10, where flux penetration in a thick $Tl_2Ba_2CaCu_2O_x$ (Tl-2212) film at 40 K is shown (sample T-1). The film is 1.2 μm thick, 3 by 3 mm wide and is grown on a single crystal substrate [18,19]. Its properties are listed in table 2.1. The penetration of flux at the edge of the film (bright line) is shown at different applied magnetic fields (figure 2.10a-d). The sample is located at the lower part of the images. Bright areas correspond to a higher magnetic flux density.
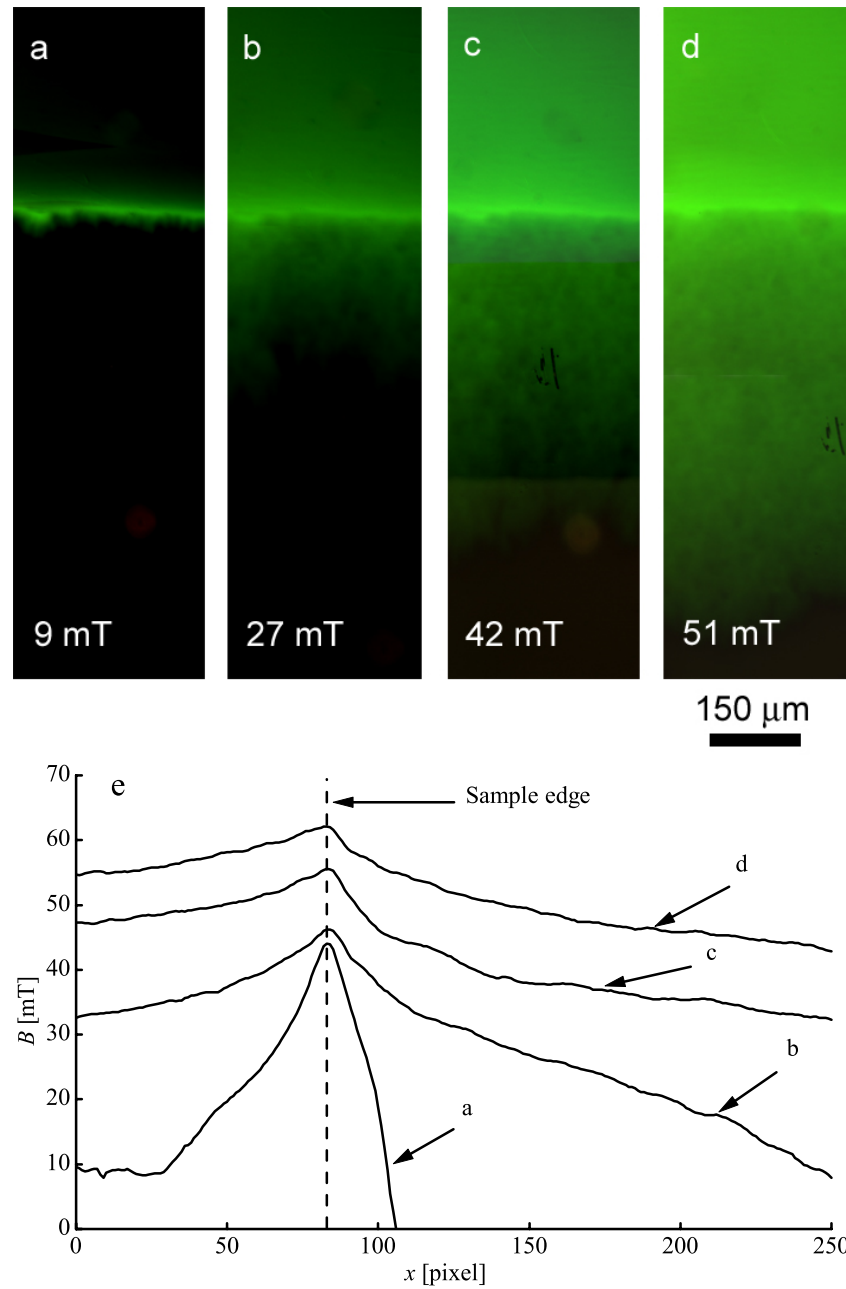
Figure 2.10. MO-images of Tl-2212 thick film T-1 at 40 K. (a-d). Magnetic fields of different strengths are applied perpendicular to the sample surface. Flux penetrates the sample deeper when the magnetic field is increased. (e). Magnetic field profiles are obtained from the intensity of the MO-images in (a-d). Pixel 0 is located at the top of the images in figures (a-d), while pixel 250 is at the bottom of the images.

Flux penetrates deeper into the sample when the external magnetic field is increased. Spatial variations in critical current density of the sample are small, which follows from a homogeneous penetration of magnetic field. The shielding field in the film enhances the external field and results in a higher intensity in the MO-images at the edge of the sample. Due to the demagnetization, the magnetic field at the sample edge is higher than the applied magnetic field.

The magnetic field profiles of the sample are obtained from the intensity of the MO-image by using expression 2.3 (figure 2.10e). The angle between the analyzer and the polarizer of the microscope in this case is set to 90 degrees. This configuration ensures that the absence of magnetic field corresponds to the lowest intensity in the MO-image. The magnetic field profiles are calibrated some distance away from the sample when a field of 9 mT is applied (figure 2.10a). The magnetic field at the top of the MO-image equals the applied field.
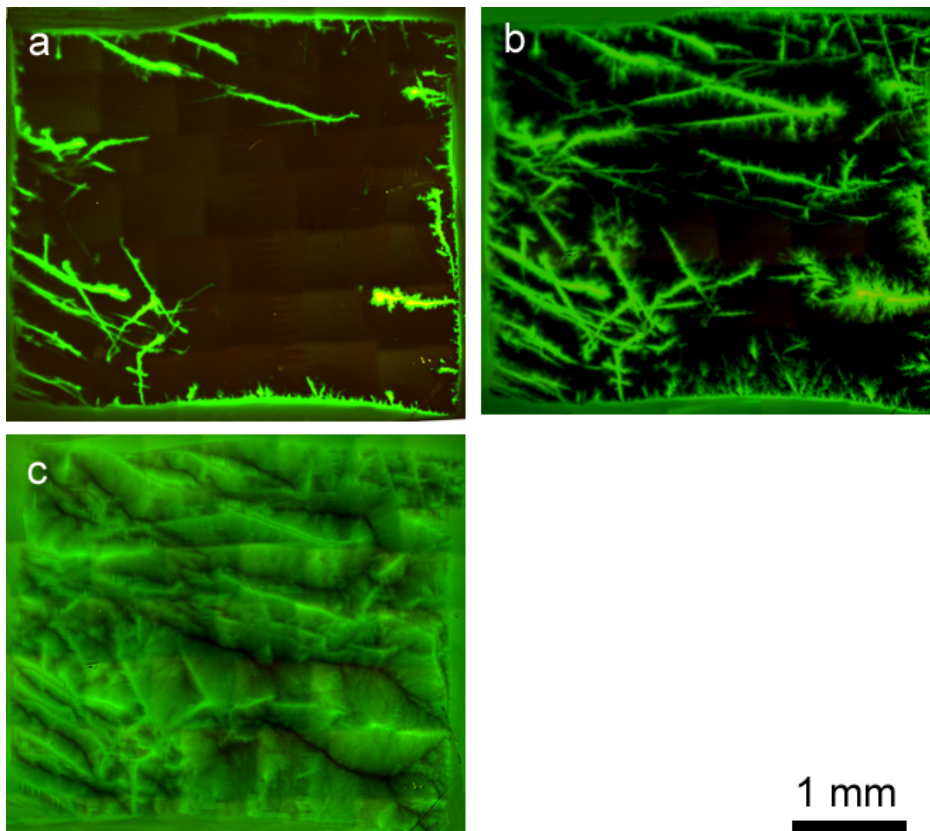
Figure 2.11. MO-images of Tl-2212 thin film T-2. An external magnetic field penetrates the film through large defects. (a) A magnetic field of 7 mT is applied at 25 K. (b) A magnetic field of 22 mT is applied at 25 K. (c) A magnetic field of 22 mT is applied at 77 K.

Defects in the grain structure are revealed by an uneven penetration of flux, as can be seen in MO-images taken from sample T-2 (figures 2.11a-c). Bright lines appear throughout the sample when a magnetic field of 7 mT is applied perpendicular to its surface at 25 K (figure 2.11a), indicating the presence of flux that penetrated the sample through crystalline defects that block shielding currents. Demagnetization of the sample enhances the magnetic field in the defects and at the edges of the sample. Flux penetrates the sample deeper through the defects and also starts to penetrate the interior of the polycrystalline structure itself when the magnetic field is increased to 22 mT (figure 2.11b). Flux penetration is increased at elevated temperatures due to a decrease in critical current density (figure 2.11c). The MO-image shows that at 22 mT the film is almost completely filled with flux that entered from the sample edges and through the crystalline defects.
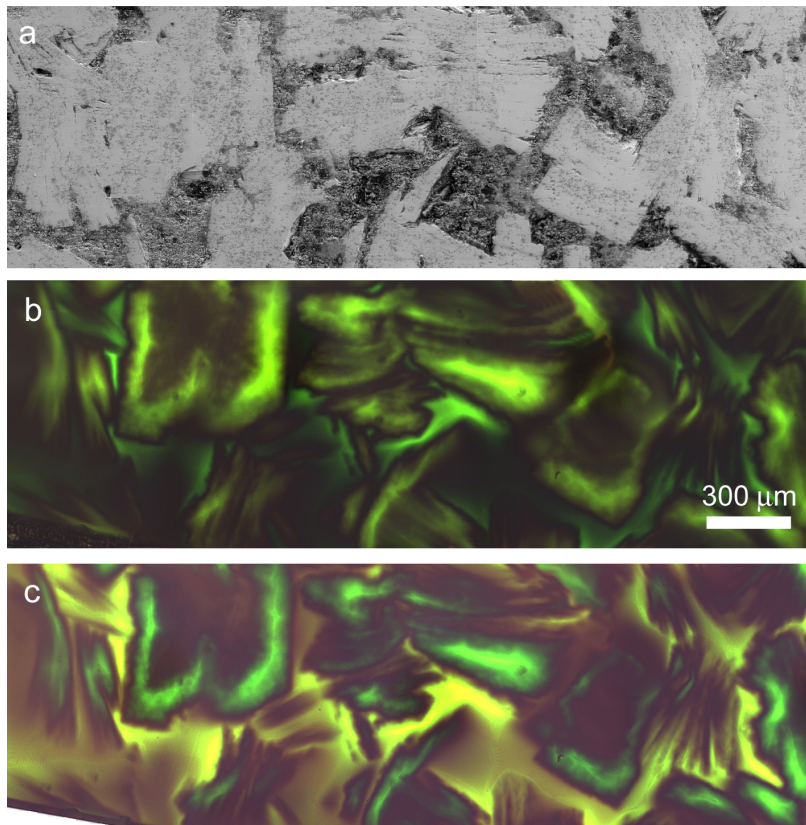
Figure 2.12. (a) SEM image of Hg-1223 bulk sample H-1. (b) MO-image of the same area at 30 K. A magnetic field of 120 mT is applied perpendicular to the sample surface to trap magnetic field in the superconducting colonies. The angle between analyzer and polarizer is set to 90 degrees. (c) A color difference between trapped flux (green) and returning flux (yellow) is observed when the angle between the analyzer and polarizer is set to 88 degrees.

Microstructural details are not only revealed by the ability of type-II superconductors to shield an applied magnetic field, but also by their ability to trap flux. This is demonstrated by comparing the MO-image of trapped flux (figure 2.12b) in a polycrystalline bulk sample with the SEM-image of its grain structure (figure 2.12a). The details of sample (H-1), which is a $HgBa_2Ca_2Cu_3O_x$ (Hg-1223) sample produced by pressing precursor powder between two silver sheets (PBS) [20], are listed in table 2.1.

The superconducting regions that appear light gray in the SEM-image trap flux after the sample is cooled within the MOI setup to 30 K and an external magnetic field of 120 mT is applied and removed. The MO-image is taken after the magnetic field is turned off. Large superconducting grains are not completely penetrated by magnetic field, which results in the absence of flux in their interior. Areas between the superconducting grains contain returning flux and appear bright as well.

Visualizing flux shielding and trapping with MOI is a useful method to study the grain structure of polycrystalline superconducting samples. Special attention should be paid to samples where the complex grain structure makes it difficult to distinguish between superconducting regions that trap flux and non-superconducting areas where flux is returning. This issue is addressed in the next section.

2.3.3. Special techniques in MOI

Regions where magnetic fields of opposite directions are present in polycrystalline high-temperature superconductors can be distinguished with magneto-optical imaging. This feature is very helpful when trapped flux in granular samples is studied and enables one to define superconducting regions.

Whether a distinction can be made between areas of opposite field depends on the angle between analyzer and polarizer in the MOI-setup. Normally, when the angle between the analyzer and polarizer of the microscope is set to 90 degrees, no information regarding the direction of the local magnetic field is obtained from the MO-image and the intensity of the reflected light is directly related to the intensity of the magnetic field. The color of the reflected light in the MO-image carries the information regarding the direction of the magnetic field when the angle between analyzer and polarizer is set unequal to 90 degrees. The difference in color is caused by the sharp dependence on wavelength of the Verdet constant of the indicator film and has a maximum for green light. The intensity of the reflected light is still related to the intensity of the magnetic field, but a shift in intensity is observed compared to the situation where the angle is 90 degrees (figure 2.13). The differences between trapped and returning flux in granular high-temperature superconductors becomes evident when the trapped flux in sample H-1 is visualized with the angle between analyzer and polarizer set to 88 degrees (figure 2.12c). The superconducting regions where flux is trapped appear green and areas of returning flux are yellow.
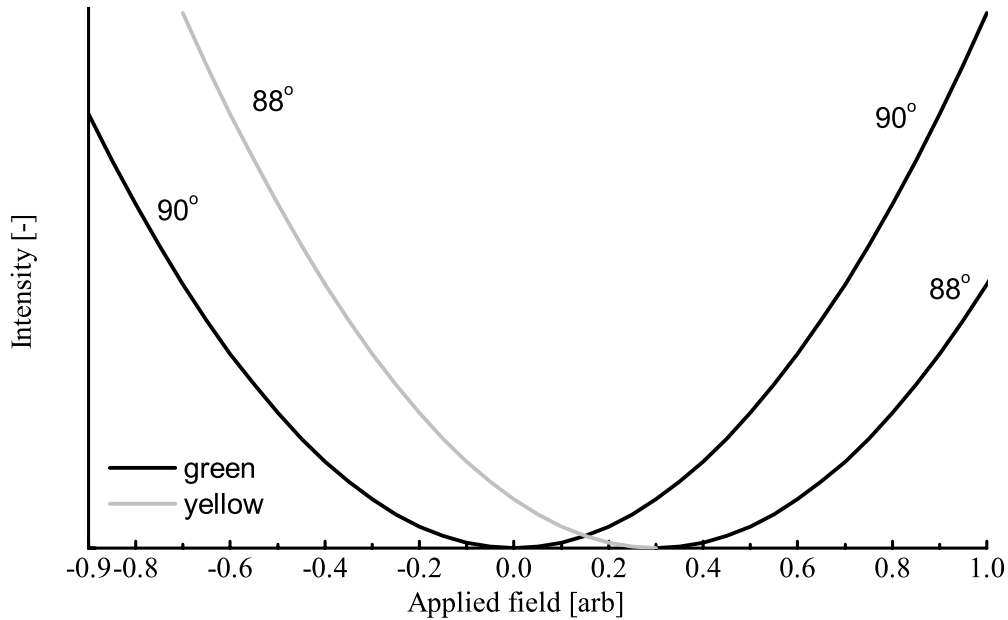
Figure 2.13. Intensity of the reflected light as function of applied magnetic field. The angle between the analyzer and the polarizer is set equal to 90 degrees or 88 degrees. The color of the reflected light is included.

MOI is also applied to obtain a qualitative image of the grain structure of YBCO coated conductors over several millimeters of conductor length. Such a qualitative image can then be used to correlate variations in macroscopic critical current density that are measured with the magnetic knife with the grain structure of the conductor. The local quality of the conductor is largely determined by the amount and size of grain colonies and the boundaries between them. A qualitative map is therefore obtained by averaging the intensity of the trapped flux in the colonies between the voltage taps along the direction of the transport current, as is demonstrated next.

The trapped and returning flux in the grain structure of YBCO coated conductor Y-1 is visualized with MOI (figure 2.14a). The properties of the sample are listed in table 2.1. The image is taken at 30 K, after flux is trapped by applying an external magnetic field of 120 mT. A large amount of colonies is visible, together with returning flux in the colony boundaries. The angle between the analyzer and polarizer is 92 degrees, which results in trapped flux that is yellow and returning flux that is green in the image.

The returning flux between the colonies is removed from the MO-image before the intensity is averaged. The original color image is converted into gray scale, using the color "red" as an indicator for the intensity (figure 2.14b). The information regarding trapped and returning flux is lost when this image is converted into gray scale without

filtering (figure 2.14c). A qualitative image is obtained from the colony map when the average intensity of the trapped flux in the *x*-direction (direction of a transport current) is calculated as function of position along the width *y* (figure 2.14d).
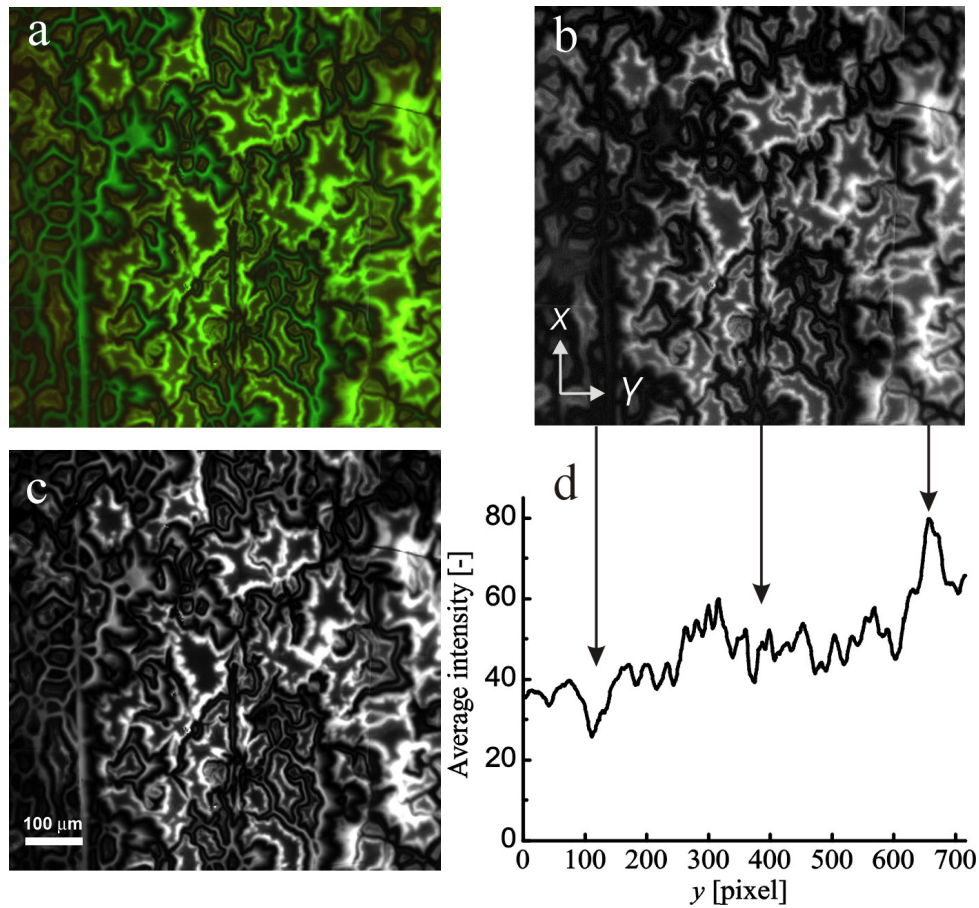
Figure 2.14. MO-image of sample Y-1, when the sample is cooled to 30 K and a magnetic field of 120 mT is applied to trap flux in the grains. The original color image (a) is converted into gray scale, using the overall intensity (c), and using the intensity of the color "red" (b). (d) The intensity, averaged over *x*, of the gray scale image of (b).

A comparison between the MO-image of the grain structure and average intensity of the trapped flux show that large colonies along the tape length correspond to a peak in the intensity. The same holds for large colony boundaries that correspond to a minimum intensity. The correlation between the colony map and the distribution in intensity shows that MOI can be applied to obtain a qualitative image of the grain structure of YBCO coated conductors.

2.3.4. Sample preparation for MOI

The sample preparation is discussed when MOI is applied to study current transport in polycrystalline high-temperature superconductors in relation to grain structure and applied strain. The image quality and resolution are largely determined by the sample properties and its installation. Since the resolution of MO-experiments is determined by the distance between sample and indicator film, a slightly bend sample will lift the indicator film away from the sample surface. The resolution will be reduced from ideally 5-10 μm to over 20 μm. The preparation also has a large impact on the outcome of the experiment. The crack structure that develops in superconducting tapes under the influence of longitudinal strain is a good example. Removing part of the matrix or gluing a strain gage on the surface can influence the crack pattern while it develops.

The magnetic field that causes a rotation of the polarization angle of the reflected light in the indicator film is not exactly equal to the magnetic field at the sample surface. Its value depends on the distance between the film and the source of the magnetic field, and the thickness of the active layer of the indicator film. The effective component of the magnetic field perpendicular to the indicator film decreases when the distance increases. Bulk samples are polished in order to reduce the distance between the sample and the indicator film and obtain the highest possible resolution. Sample alignment is important as well since the indicator film is placed directly on top of the sample. The light is reflected under an angle and the image is lost as soon as the indicator film is no longer oriented perpendicular to the incoming beam of light.

The superconducting filaments in Bi-based tapes are surrounded by a relatively thick silver matrix (here 20 μm), resulting in a large distance between the indicator film and the filaments and therefore lowering the image resolution. Part of the silver matrix is removed by etching with a NH_4OH/H_2O_2 solution to reduce the distance between the filaments and the indicator film and thereby increasing the resolution of the technique to approximately 10 μm. The silver cap layer of YBCO coated conductors is not removed, since it is only 1-2 μm thick.

The strain that is applied to Bi-based tapes is not measured at the sample holder due to space limitations. It is measured using a strain gage that is glued to the bottom of the sample (figure 2.15). The reinforcement of the tape by the strain gage prevents the tape from failing under the gage. The tape will develop a single crack at the border of the gage due to stress concentrations. Fiberglass patches are glued on the tape to avoid failures outside the indicator film. One set of patches is glued next to the strain gage, on the bottom of the sample, while another set is glued on top. The patches on top of the sample run from the effective area of the strain gage to the point where they overlap the patches located at the bottom. This configuration ensures the absence of stress concentrations due to the strain gage. The absence of stress concentrations due to either

sample etching or the application of a strain gage is verified by comparing the observed crack pattern with that of an intact tape.
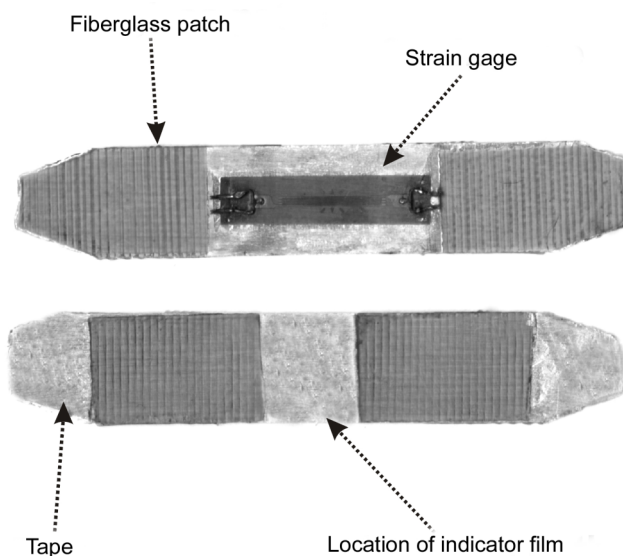
Figure 2.15. A strain gage is glued underneath the superconducting tape to measure the applied strain. Fiberglass patches are used to reinforce the tape next to the gage.

2.4. Conclusions

Several experimental techniques are developed in order to measure the influence of grain connectivity and flux pinning on the critical current density of polycrystalline high-temperature superconductors. The effect of for instance flux pinning is studied by measuring the critical current density as function of applied field and temperature over a length-scale of 5-10 mm using transport current and dc-magnetization methods.

A correlation between grain connectivity and macroscopic critical current density in Bi-based tapes can be made by comparing the effect of longitudinal strain on the critical current and grain connectivity. The effect of applied longitudinal strain on the critical current is measured using a U-shaped bending spring. The effect on the grain structure is studied with MOI with a resolution of approximately 10 μm. The applied strain in both cases cannot be measured directly. Strain is measured by strain gages that are placed on the sample holder (bending spring) or on the sample itself (magneto-optical imaging).

The correlation between grain connectivity and macroscopic critical current density in YBCO coated conductors can be investigated by combining two techniques. The spatial variation in the critical current density is measured with the magnetic knife, with a resolution of 50 μm. This non-destructive method uses a transport current to measure the critical current. The distribution in critical current density is then compared to the local grain structure, by constructing a detailed map of the colonies with MOI. A special technique in MOI is described that distinguishes between trapped and returning flux. A qualitative image of the colony structure in YBCO coated conductors is obtained when the returning flux is eliminated from the MO-image. This makes a direct comparison between the colony structure and the spatial distribution of the critical current density possible.

3. Grain structure and current distribution in polycrystalline high-temperature superconductors

The overall critical current density in bulk superconductors like $Bi_2Sr_2Ca_{y-2}Cu_{y-1}O_x$ and $YBa_2Cu_3O_x$ is limited by their inhomogeneous grain structure. Different mechanisms in different parts of the conductor play a role in limiting the critical current density. The objective of this chapter is to answer two important questions. The first question is how the local variations in critical current density influence the global transport behavior. This question is addressed by measuring the spatial variation in critical current density in $YBa_2Cu_3O_x$ coated conductors with the magnetic knife. The local properties are studied with magneto-optical imaging, which visualizes the penetration of magnetic flux in the conductor. The combination of both novel experimental methods makes a direct comparison between the spatial distribution of current density and the grain structure of the conductors possible. The second question addressed is whether the microstructural features that are responsible for the "weak-link" behavior can be distinguished clearly and unambiguously. The location of the (mechanical) weak links in the current path in Bi-based tapes is revealed by studying the changes in magneto-optical images while applying longitudinal strain. A comparison of the crack pattern in $Bi_2Sr_2Ca_2Cu_3O_x$, and $Bi_2Sr_2CaCu_2O_x$ tapes as well as $YBa_2Cu_3O_x$ coated conductors is made in order to relate the grain structure to the production process of the conductors.

3.1. Introduction

The result of extensive studies on the current limiting mechanisms of $Bi_2Sr_2CaCu_2O_x$ (Bi-2212) and $Bi_2Sr_2Ca_2Cu_3O_x$ (Bi-2223) tapes shows that the granular microstructure allows a supercurrent to flow along multiple current paths. An example of the grain structure of a Bi-2223 tape is shown in figure 3.1, where a complex structure of platelets is observed. Grains that are stacked together with their *c*-axis aligned are forming so-called colonies. A large number of colonies are seen, as well as long chains of well-connected grains.
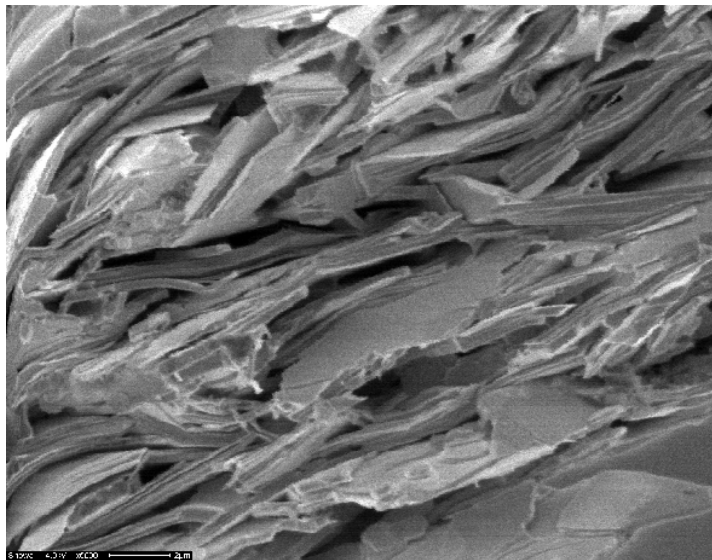
Figure 3.1. SEM-image of the grain structure of a typical Bi-2223 tape.
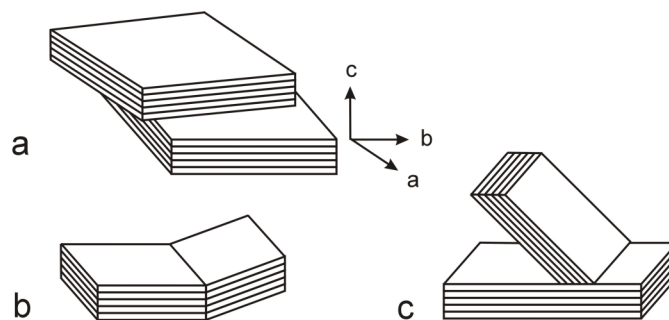
Figure 3.2. Boundaries between grains and colonies of well-connected grains that are often observed in Bi-based tapes are: a) OABTWIST, b) ECTILT and c) SCTILT.

The most common boundaries between grains are shown schematically in figure 3.2 and are boundaries where two grains with the *ab*-plane parallel partly overlap (OABTWIST), edge-on *c*-axis tilt (EC-TILT) and small-angle c-axis tilt (SCTILT) boundaries [21]. The boundary shown in figure 3.2a is often observed in colonies, while the boundaries in figures 3.2b and 3.2c are colony boundaries.

Recently, industry has focused their attention on the production of $YBa_2Cu_3O_x$ coated conductors (YBCO CC). High-quality films on metal substrates have been produced, using various deposition methods. Texture in nickel or nickel-alloy substrates is induced using for instance the "rolling assisted biaxial textured substrates" (RABiTS) - approach. Buffer layers are deposited on top of the substrate in order to improve the texture and to protect the YBCO layer from the metal substrate. The conductor is produced as a thick film of YBCO, ranging from 400 nm to several micrometers in thickness, deposited on a buffered metal substrate. Several deposition techniques are applied; vacuum techniques as for instance pulsed-laser-deposition (PLD), or non-vacuum techniques such as metal-organic-deposition (MOD) [22,23,24]. The YBCO layer consists of a thin layer of grains that has copied the grain structure of the substrate [25]. This is shown schematically in figure 3.3, where a detailed view of the architecture of a typical YBCO coated conductor as produced with PLD is presented. The granular structure of the YBCO layer may lead to a similar mechanism for transport current, as in Bi-based tapes. The main difference compared to the grain structure of Bi-based tapes is the more or less two-dimensional structure of the superconducting layer in YBCO coated conductors.
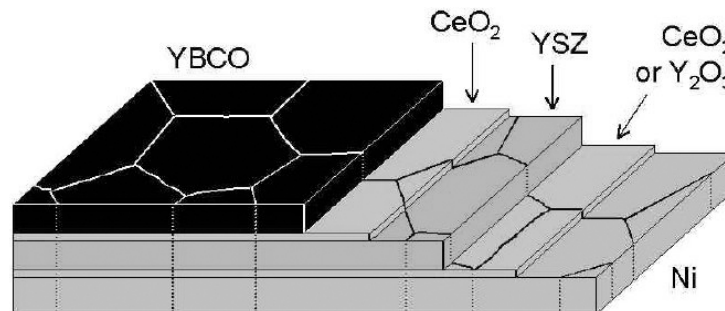
Figure 3.3. Structure of a YBCO coated conductor produced with pulsed-laser-deposition on RABiTS. Courtesy of D.M. Feldmann.

A large amount of experiments over the last decade has led to a general semi-empirical picture of current flow in these highly inhomogeneous structures. The question what exactly limits the critical current density in the bulk of high-temperature superconductors and what role the grain structure is playing is still not satisfactory answered. The development of several new experimental techniques enables detailed

analysis of the influence of the local grain structure on the transport properties of high-temperature superconductors. The magnetic knife is such a novel technique to measure the spatial distribution in critical current density (J_c) of Bi-based tapes and YBCO coated conductors [26,27]. The technique described in detail in section 2.2 is applied to investigate the link between the macroscopic critical current (I_c) and the local variations in J_c. Magneto-optical imaging (MOI) is refined in the last decade and is applied to visualize magnetic flux inside high-temperature superconductors on a micrometer scale [28,29,30]. It is a relevant technique in studying the correlation between grain structure and local J_c. Several studies where MOI is applied to visualize flux penetration in YBCO CC have shown that the critical current density at grain boundaries is several orders in magnitude lower than inside the grains [31,32]. This result is supported by experiments on YBCO bi-crystals [33,34], where the inter-granular critical current density becomes smaller than the intra-grain critical current density when the angle of the grain boundary exceeds 3-5 degrees. Although, based on these results, it is expected that grain boundaries limit J_c on a macroscopic scale as well, a direct comparison between grain structure and J_c in polycrystalline samples has not yet been made successfully. MOI and the magnetic knife are combined to correlate the macroscopic critical current density and grain structure.

Magnetic flux can be visualized with MOI with a resolution of several micrometers. However the technique is not able to identify directly which part of the grain structure is forming the weak link in the current path. In this study a more detailed investigation is made by combining MOI with tensile strain. The dependence of the averaged critical current density of Bi-2223 tapes on magnetic field is described as a network with multiple current paths. As is mentioned in chapter 1, the critical current at low magnetic fields is largely carried by a network of weakly-linked grains, while at high field the current is carried by a strongly-linked backbone. The relation between weak links in the current path and tensile strain is known from several experimental results [35,36,37]. The critical current in Bi-2223 tapes at low field degrades more rapidly than that at high field when the longitudinal strain exceeds the critical strain at which the critical current (I_c) degrades irreversibly. The observed degradation at low field as function of applied strain is an indication that the microstructural damage mostly occurs within the weakly-linked network [38].

Magneto-optical imaging is applied to visualize the mechanically weak spots in the grain structure, which are thus correlated to the weak links in the current path. Ultrasonic fracturing experiments on filaments extracted from Bi-2223 tapes [39] showed that the intermediate rolling steps in the production process cause microcracks that are partly healed by subsequent heat treatments. In this study the crack formation in Bi-2212 tapes is investigated to reveal the similarities and differences of the grain structures of both Bi-based conductors and to correlate the results to particular differences in production process. Because YBCO is a ceramic superconductor, an irreversible

degradation in J_c is expected in YBCO coated conductors, as is the case with Bi-based tapes. It is also investigated whether the crack pattern in the YBCO layer is dominated by the relatively thick substrate. When this is the case, a different degradation in I_c under tensile strain compared to Bi-based tapes is expected.

3.2. Distribution of the critical current density in YBCO coated conductors

The influence of the production process on the grain connectivity in YBCO coated conductors that are produced with pulsed-laser-deposition and metal-organic-deposition is studied. A quantitative image of colony boundaries in the conductor is generated on a macroscopic scale, based on flux penetration that is visualized with magneto-optical imaging. The spatial distribution in macroscopic critical current density is measured with the magnetic knife. The combination of both techniques is applied to make a correlation between grain structure and macroscopic critical current density. The length scale over which colony boundaries and defects in the grain structure reduce the macroscopic critical current is investigated. Also, the influence on a macroscopic current of large defects that run along the longitudinal direction of the conductor is studied.

3.2.1. Flux penetration in YBCO coated conductors

To give a first impression on how high-angle grain boundaries and defects form easy pathways for flux to penetrate the conductor, the penetration of magnetic flux in YBCO coated conductors that are produced with PLD and MOD is studied with MOI.

Several studies showed that the misalignment with the neighboring grains is responsible for the relatively low critical current density in YBCO coated conductors [31, 32]. A large number of studies on YBCO bi-crystals were performed in the past [40,41,5,42]. Similar studies have only been performed on Bi-2212 crystals [43,44]. The results show that the critical current density in grain boundaries decreases rapidly when the misalignment angle between the grains exceeds 4 degrees, while the decrease is only marginal when this angle is less than 4 degrees [45]. It is demonstrated in earlier studies [31] that the critical current density in YBCO coated conductors is not limited by their intra-grain properties, but by inter-granular currents. It was shown on a local scale that a transport current percolates around high-angle grain boundaries. In this work, a direct correlation between such local variations and the macroscopic transport current in YBCO coated conductors is obtained.

The layered structure of YBCO coated conductors makes it possible to obtain a clear image of the grain structure with MOI. Similar to Bi-based tapes, colonies of well-aligned grains are connected through colony boundaries in YBCO coated conductors. The

grain structure of Bi-based tapes can not be visualized in such detail, because the powder-in-tube method used for the production of Bi-based conductors results in a much more complex grain structure. Each filament in the matrix consists of multiple layers of grains that are connected in a three-dimensional fashion, while the thin YBCO layer of coated conductors forms a two-dimensional colony structure.

	Superconductor	Matrix/ substrate	# of filaments or layer thickness	Production method	I_c [A] in self-field
B-1	Bi-2223	AgMg	19	PIT	30 (77 K)
B-2	Bi-2223	Ag	65	PIT	20 (77 K)
B-3	Bi-2212	Ag	19	PIT	400 (4.2 K)
Y-1	YBCO	Ni	0.4 μm	PLD	15 (77 K)
Y-2	YBCO	NiW	1.2 μm	TFA-MOD	75 (77 K)

Table 3.1. Relevant properties of the samples investigated in chapter 3.

An illustration of the magnetic field penetration of a YBCO coated conductor through high-angle grain boundaries is shown in figure 3.4a. The 0.4 μm thick YBCO layer is deposited with PLD (sample Y-1). Some key properties are listed in table 3.1. The image is taken while a magnetic field of 12 mT is applied perpendicular to the sample surface at 30 K. It is observed that magnetic flux penetrates through high-angle colony boundaries. Penetration starts from the edge of the tape, which is located at the bottom of the image. The interior of the colonies is completely shielded from the magnetic field and appears dark in the image. The magnetic field between the colonies is indicated by the higher intensity in the image and is actually higher than the applied magnetic field. This is seen by a higher intensity at the grain boundaries in the MO-image in figure 3.4a, compared to the area next to the sample where the field equals the applied field. The enhancement of the magnetic field in the colony boundaries is due to the demagnetization of the colonies, as is the case with the Tl-based samples discussed in chapter 2.

Figure 3.4b shows the same area of sample Y-1, after a magnetic field of 120 mT is applied perpendicular to the tape surface. The magnetic field is removed before the image is taken, revealing not only the high angle colony boundaries, but also showing magnetic flux that is trapped within the colonies. From these results it is clearly demonstrated that flux easily penetrates high-angle colony boundaries, which have a J_c that is several orders in magnitude lower than that the critical current density inside the grains.
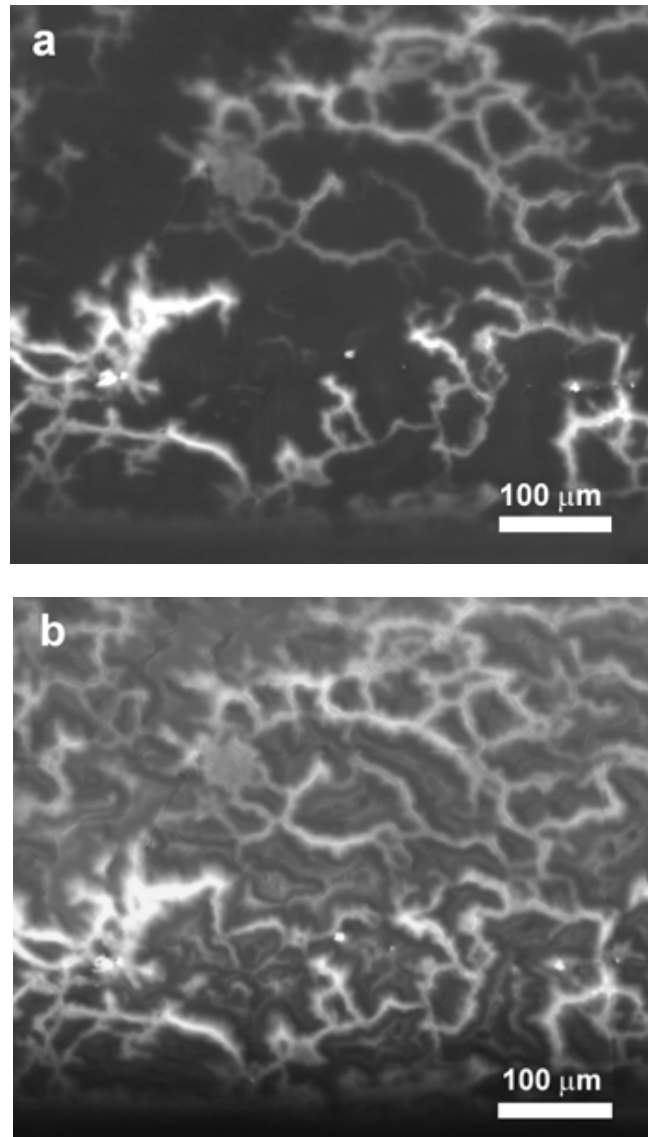
Figure 3.4. (a) MO-image of magnetic flux penetrating the colony boundaries of sample Y-1 at 12 mT, at 30 K. (b) Flux is trapped in part of the colonies after 120 mT is applied and removed.

As shown previously, flux penetrating in colonies and colony boundaries is clearly visible with MOI in samples that are produced with PLD. This is not the case for samples produced with MOD, where a different field penetration is observed. The field penetration of sample Y-2 at 30 K is shown in figures 3.5a and 3.5b. The properties of this sample are also listed in table 3.1.
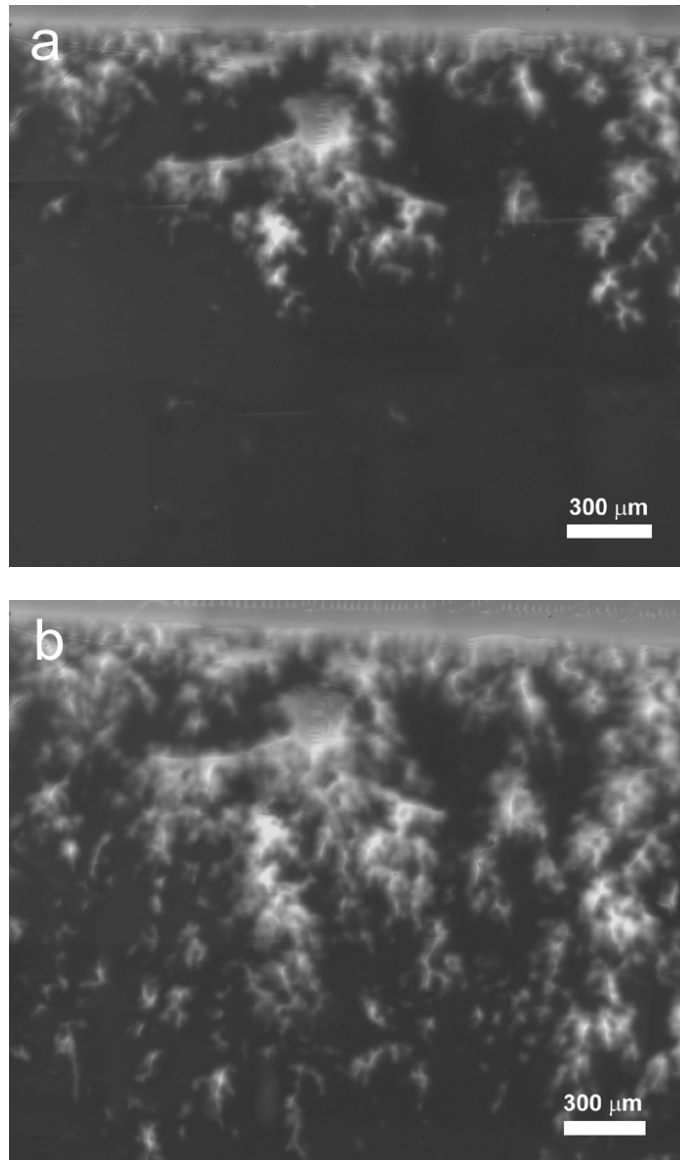
Figure 3.5. (a) MO-image of magnetic flux penetrating sample Y-2 at 30 K for an applied field of 10 mT. (b) 18 mT.

The difference in field penetration between both types of coated conductors is evident from the MO-image in figure 3.5a, where an external magnetic field of 10 mT is applied perpendicular to the tape surface. The edge of the tape is located at the top of the figure. Flux still penetrates the conductor through high-angle colony boundaries, but the

boundaries are no longer seen as clearly as in sample produced with PLD (Y-1), even when the field is increased to 18 mT (figure 3.5b). The difference in penetration is mainly caused by the thicker YBCO layer of sample produced with MOD (Y-2), although a different substrate material is used in its production [23] as well. The YBCO layer of sample Y-2 consists no longer of one single layer of connected grains, but is more three-dimensional. The flux penetration characteristics as shown indicate a much better grain-to-grain connectivity in YBCO coated conductors which are produced with MOD.

3.2.2. Distribution in critical current density of YBCO coated conductors

It is demonstrated in the previous section that the grain structure of YBCO coated conductors results in large variations in the local critical current density. In order to study the effect of the local variations on the macroscopic transport current, the spatial distribution in critical current density across the width of the conductor is measured with the magnetic knife technique, as is discussed in section 2.2. The spatial distribution of the critical current density of YBCO coated conductors produced with pulsed-laser-deposition and metal-organic-deposition is compared to investigate the effect of the production process on the connectivity on a macroscopic level. Based on the difference in grain connectivity on a microscopic level that is observed with magneto-optical imaging and is described in the previous section, large differences between samples are expected.

Large variations in critical current across the width of a YBCO coated conductor that is produced with PLD (Y-1) are observed when the spatial distribution of the critical current is measured in the magnetic knife (figure 3.6). The distance between the voltage taps is 2 mm, which determines the longitudinal length scale over which the critical current is averaged. Variations in critical current of the conductor as function of position indicate a spatial variation in critical current density, because the thickness of the YBCO layer is taken as constant.

The variation is much more pronounced when the spatial distribution in J_c is regarded (figure 3.6) after deconvolution (expression 2.2). Deconvolution cancels the "smearing out" of the $J_c(x)$ profile in the $I_c(x)$ experimental data, so that the amplitude variations are pronounced. This is seen for instance when the sample is located entirely in one of the iron cores. An average value of J_c of approximately 5 kA/mm^2 is measured in sample Y-1. Large variations in local J_c, as expected from the results obtained with MOI in the previous section, result in areas where the critical current density is zero and in other areas where it is as high as 10 kA/mm^2.
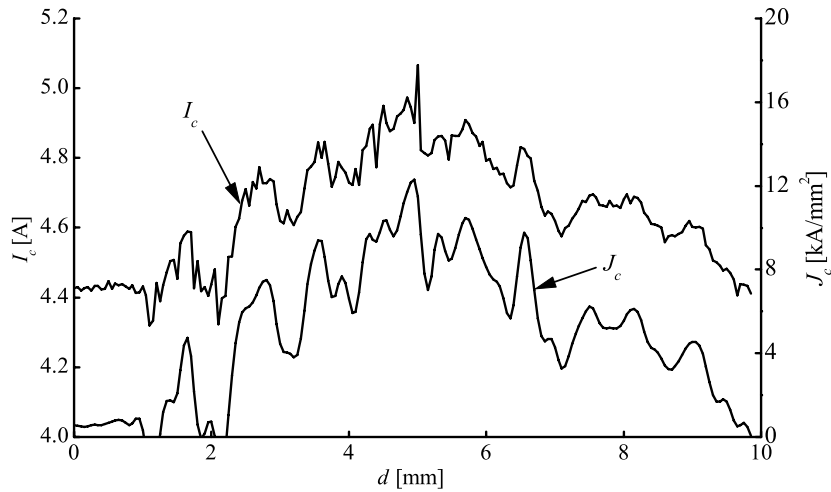
Figure 3.6. The critical current across the width of sample Y-1 measured with the magnetic knife technique at 77 K. The critical current density distribution is included in the figure.
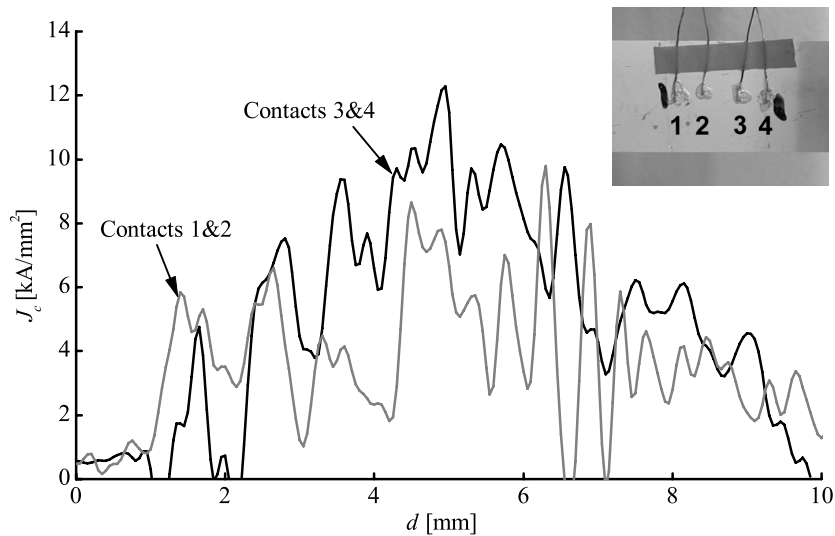
Figure 3.7. The critical current density distribution across the width of sample Y-1 at 77 K, measured at two different locations. The inset shows the location of the voltage taps on the sample.

The distribution in J_c of the same sample is measured at a second location in the conductor to determine whether the grain structure is responsible for the large variations in the spatial distribution of J_c or whether this is caused by defects that run in the longitudinal direction. A second set of voltage taps is applied, located 2 mm away from the initial set. Figure 3.7 shows the critical current density distribution across the width of

sample Y-1, for both sets of voltage taps. The critical current density at both locations not only shows variations of over 100 % of the mean value across the width of the sample, but also between the voltage taps. This indicates that the microstructural details that cause the variations are much smaller than the separation between the voltage taps. Some defects run along the longitudinal direction of the sample, over a larger scale than the voltage taps. This is concluded from the local minimum in J_c at corresponding location d (=7 mm) between both voltage taps. The presence of such defects is studied with MOI in section 3.2.3.

The large variation in spatial distribution in J_c of the sample that is produced with PLD is explained as follows. The YBCO layer is only 400 nm thick and consists of a single layer of colonies; current has to get around defects by flowing in a two-dimensional network. Small defects already have a large impact on the macroscopic J_c, when such a defect is located in the region of the magnetic knife where the field is zero. This is not the case for the sample that is produced with MOD (Y-2), which has a thicker YBCO layer that provides a transport current with more options to get around defects. Smaller variations in spatial distribution in J_c are the result, as is seen for two locations in figure 3.8.
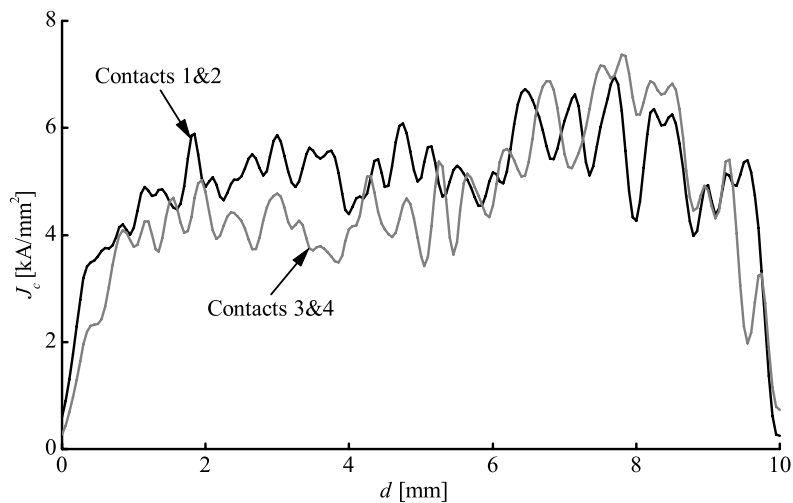
Figure 3.8. The critical current density distribution across the width of sample Y-2 at 77 K, measured at two different locations.

Even though much smaller variations are observed, some of the maxima and minima in J_c line up in some locations along the conductor, while no correlation is found in other locations. The cause of the variations in J_c is obtained when the grain structure of the conductor is analyzed. In order to provide a link between grain structure and

macroscopic J_c, a detailed investigation of the grain structure with MOI is presented in the next section.
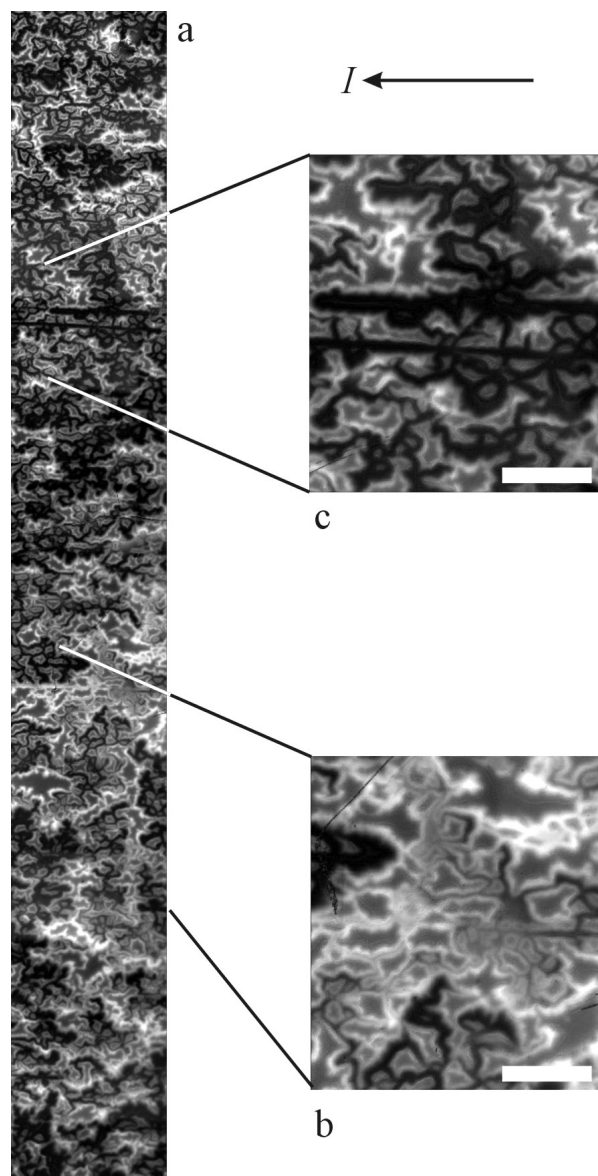
Figure 3.9. MO-image of the colony structure of sample Y-1 at 30 K, after flux is trapped at 120 mT. (a) The image is taken over the full width of the sample, which is 1 cm. Enlargements show; (b) large colony clusters, and (c) large colony boundaries. The scale bars in the enlargements are 200 μm. The arrow points in the direction of the transport current.

3.2.3. Comparing the grain structure and the critical current density distribution

A direct comparison between the results of magnetic knife and magneto-optical imaging is made to obtain a qualitative picture of the grain structure of YBCO coated conductors. The local penetration of magnetic flux is compared with the measured distribution of the macroscopic critical current density.

First, the grain structure of YBCO coated conductors that are produced with PLD on a nickel substrate (Y-1) is studied. A magnetic field of 120 mT is applied perpendicular to the conductor surface at 30 K to visualize flux that is trapped in the superconducting colonies (figure 3.9). The magnetic field is removed before the MO-image of the sample is taken over the full width, over 1 mm of its length. A detailed map of the colony structure is obtained, where part of the colonies appear bright due to the flux that is trapped in their interior. Darker areas correspond to colony boundaries where magnetic flux is absent.

Large differences in grain structure of the tape are revealed by variations in the intensity of the MO-image. The enlargement in figure 3.9b shows a stack of large colonies that, due to their size, are only slightly penetrated by magnetic field. A transport current that crosses the colonies from bottom to top is only partly obstructed at this location by a small number of colony boundaries. The enlargement in figure 3.9c shows a location where only very small colonies, connected over large colony boundaries, are present. Some of the colony boundaries are directed along the direction of the current and will reduce J_c over a larger length along the conductor.

A comparison between the local trapped flux as visualized with MOI and the spatial distribution in J_c shows that areas where flux is trapped corresponds to maxima in the macroscopic critical current density (figure 3.10). The MO-images show large areas where magnetic flux is trapped, indicating the presence of large clusters of colonies. Dark areas in the MO-image are correlated to the presence of large colony boundaries in between the clusters. From a visual comparison between the variations in J_c and the local intensity of the trapped flux, it is concluded that large areas where flux is trapped correspond to a maximum in local J_c. Areas where trapped flux is absent correspond to minima in J_c.

One of the most striking similarities between the electrically obtained distribution in J_c and the MO-image is the presence of dark lines that run along the length of the conductor in the MO-image at the same location where J_c is zero. The poorly connected colonies that are responsible for the low J_c at the locations of the dark lines are most likely due to defects in the substrate that run in the longitudinal direction of the sample. The length scale over which the defects affect the critical current is larger the distance

between both sets of voltage taps. This results in a minimum of the critical current density at the same location between voltage taps 1-2 and 3-4.
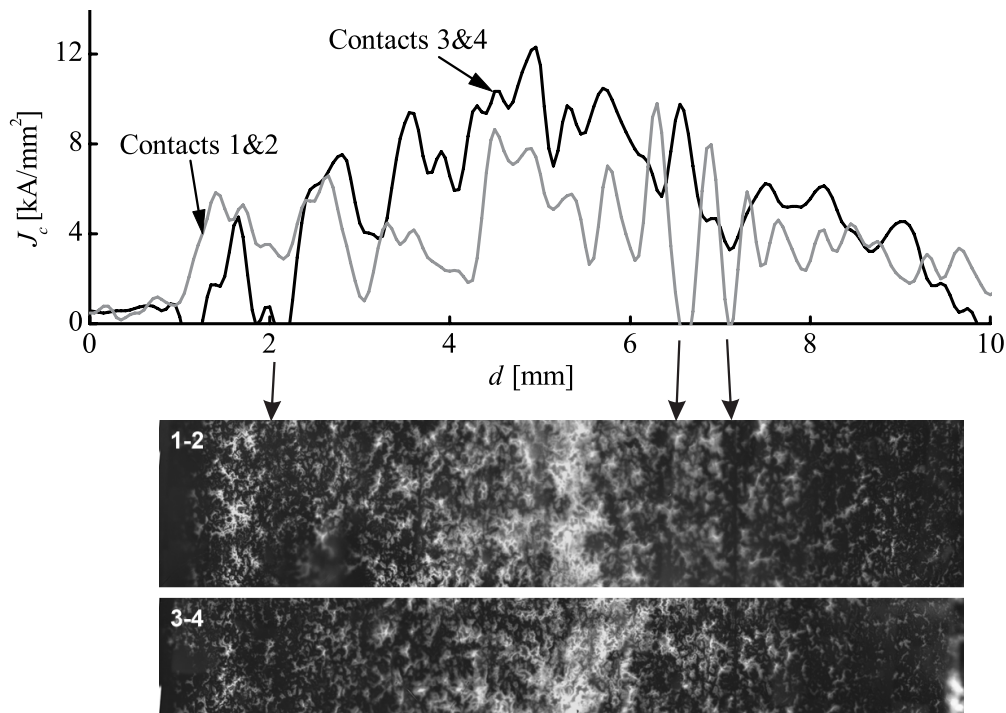

Figure 3.10. Critical current density distribution of a YBCO coated conductor produced with PLD (sample Y-1), measured at two locations. The MO-images are taken at the same locations as the voltage taps after flux is trapped at 120 mT.

Although the defects run along the tape length and therefore in the direction of the transport current, they still have a large effect on the local J_c. It is unambiguously concluded from this data that the current in YBCO coated conductors does not run entirely in the longitudinal direction of the tape, but has a significant component in the normal direction. Apparently the current meanders through the tape over a length scale of approximately 50-100 μm, bypassing defects in the grain structure.

In order to clarify the influence of the thickness of the YBCO layer and of the production process on the connectivity of the grains, the grain structure of YBCO coated conductors that are produced with MOD (Y-2) is studied with MOI. The MO-image of the flux trapped in the colonies (120 mT, 30 K) shows a much more evenly distributed flux pattern (figure 3.11). The distribution in J_c, measured with the magnetic knife at the same location, is included in the image for comparison. The presence of a large bright area in the MO-image at the centre of the tape indicates that a high degree of grain connectivity is present in the sample. This connectivity results in a "Bean-like" profile in

the trapped flux across the width of the conductor and indicates the existence of sample-wide shielding currents. A large number of smaller islands of trapped flux are present on top of the Bean-like flux profile, which shows that there are still local variations in connectivity of the colonies, although much smaller compared to the variations in connectivity in the sample that is produced with PLD (Y-1). It is not possible to make a direct comparison between the trapped flux and the local J_c of the sample, due to the high degree of grain connectivity and the absence of large-scale defects.
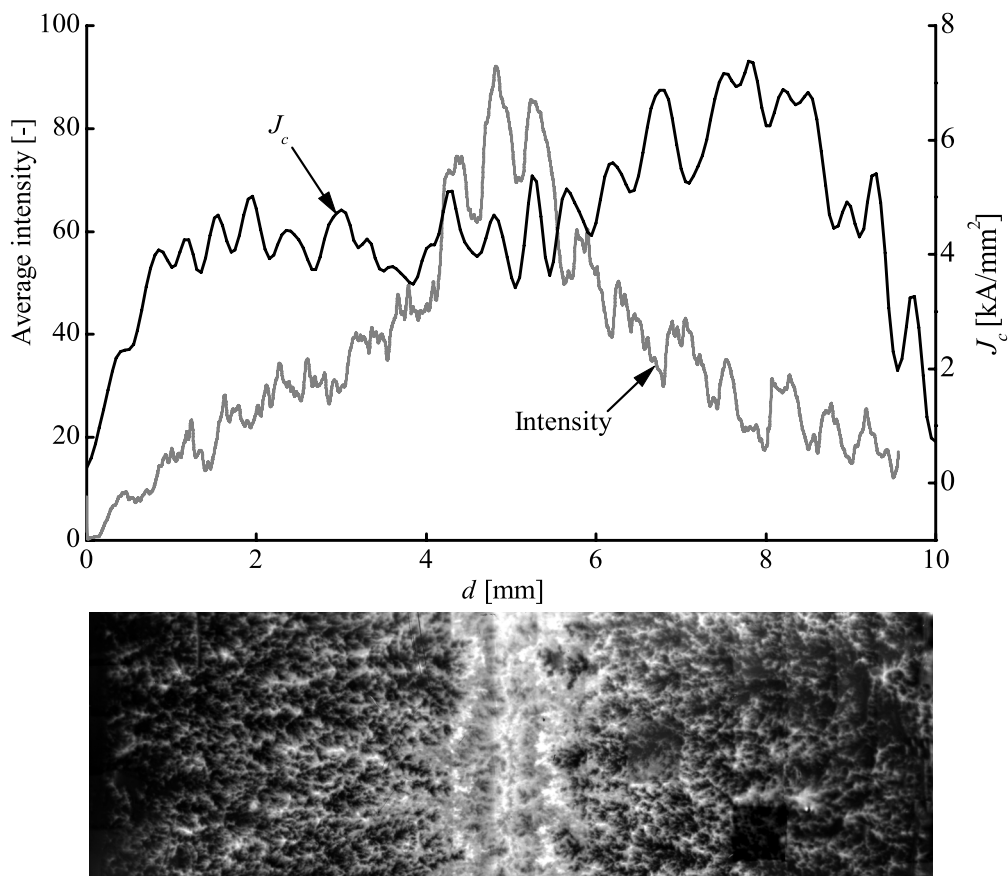
Figure 3.11. Critical current density distribution of sample Y-2, together with the MO-image at the same location as the voltage taps when flux us trapped at 120 mT. The average intensity of the MO-image is included in the graph.

A (more) quantitative comparison between both experimental methods is made after a quantitative picture is constructed from the MO-image of the trapped flux in the sample. The procedure how to obtain such a quantitative picture of the grain structure in YBCO coated conductors from the intensity of the MO-image is described in

section 2.3.3. The intensity of the trapped flux across the width of the samples produced with MOD, averaged along the direction of the current, is shown in figure 3.11. A large variation in trapped flux is seen on top of the "Bean-like" flux pattern in samples produced with PLD and MOD (figure 3.12). The much more pronounced "Bean-like" pattern of the trapped flux in sample produced with MOD indicates that shielding currents run across its entire width, while in the sample produced with PLD there are no sample-wide shielding currents present. Variations on top of this structure are due to local variations in critical current density. The variations appear over a comparable length scale of approximately 100 μm in both samples.
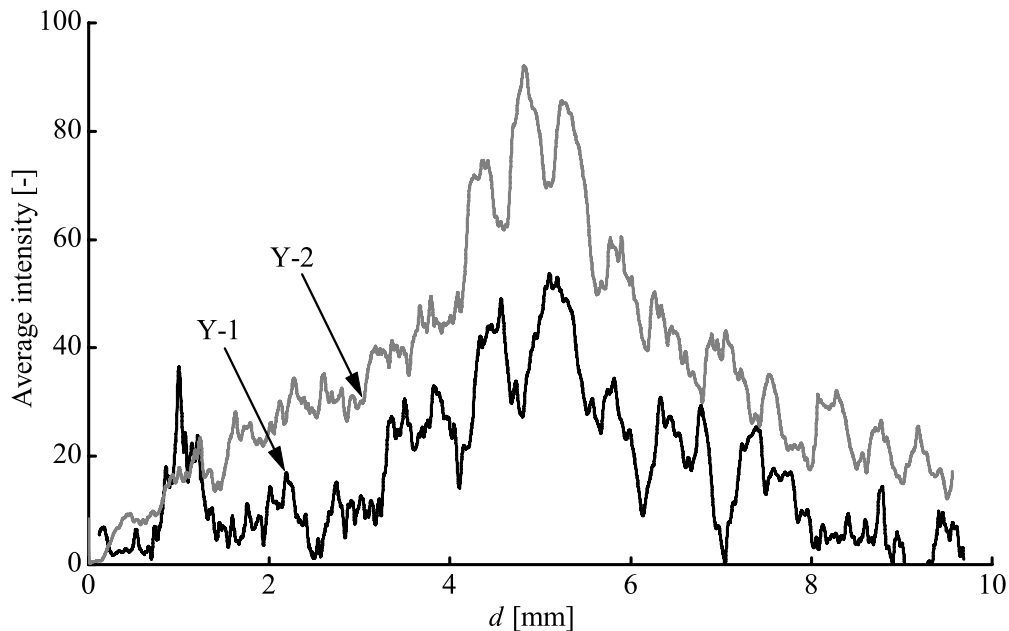
Figure 3.12. Intensity of the trapped flux in samples Y-1 and Y-2 as function of the position across the width of the tapes.

The variations in macroscopic critical current density correlate directly with the grain structure of the sample. Large clusters of colony boundaries result in a reduced critical current density. This can be concluded from figures 3.11 and 3.13, where the average intensity of the MO-images and the spatial distribution in macroscopic critical current density of samples that are produced with PLD and MOD are compared. It is concluded from these data that although a better connectivity is present in the sample that is produced with MOD, the variations in microscopic J_c are caused by colony boundaries and are of comparable length scale in both samples.
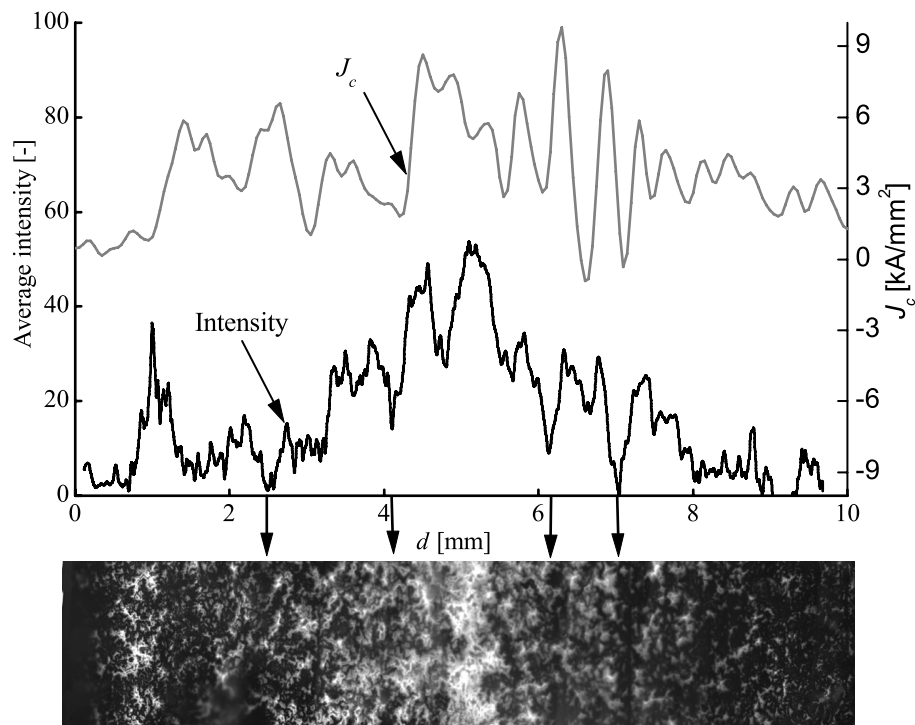
Figure 3.13. The average intensity of trapped flux in sample Y-1 is shown together with the distribution in critical current density. The MO-image of the flux trapped at the same location of the sample is shown as a reference.

3.2.4. Conclusions on critical current density in YBCO coated conductors

The most striking conclusion is that the current paths in YBCO coated conductors are not one-dimensional. Current meanders around defects on a length scale of approximately 50-100 μm, forming two-dimensional current paths. This is concluded from the correlation between macroscopic and microscopic critical current density in YBCO coated conductors obtained, by combining the results of two experimental techniques. From the comparison of trapped flux (MOI) and current distribution (magnetic knife) it is concluded that the macroscopic critical current density is limited by large concentrations of colony boundaries and defects that are related to the production process.

3.3. Crack formation in high-temperature superconductors

The second key question to be answered is whether the microstructural features that cause the weak-link behavior in the current path of high-temperature superconductors can be distinguished clearly. Although the resolution of magneto-optical imaging is not high enough to directly visualize the weak links, the locations of the weak links can be pointed out indirectly by combining magneto-optical imaging with tensile strain. The influence of the production process on the grain structure of Bi-based tapes and YBCO coated conductors is investigated in detail. The formation of weak links in Bi-2223 tapes is correlated to intermediate rolling steps in the production process. It is verified whether the absence of intermediate rolling steps in the production process of Bi-2212 tapes results in a different crack formation, compared to Bi-2223 tapes. The superconducting layer of YBCO coated conductors is thin compared to the substrate, which may result in a crack formation that is determined by the substrate and not by the superconducting layer.

3.3.1. Introduction

The effects of applied tensile strain on the transport critical current of ceramic high-temperature superconductors are outlined in this section. A model is introduced that relates the degradation of the critical current of Bi-based tapes to the precompression of the filaments by the matrix.

The critical current of Bi-based tapes degrades irreversibly when the applied tensile strain exceeds a certain value, which is called the critical strain (ε_c). Numerous publications relate ε_c to the pre-compression experienced by the superconductor [46,47,48,49]. The superconducting filaments in Bi-based tapes are compressed when the tape is cooled from its reaction temperature at ~1100 K to its operation temperature, ranging from 4.2 K to 77 K. The precompression is caused by the difference in thermal contraction of the BSCCO core and the silver or silver-alloy matrix. Although the filaments of Bi-2223 tapes can deform without damage [47], the critical current decreases irreversibly when the applied strain exceeds the precompression value of the filaments by an amount larger than their elastic strain limit. The relation between critical current and applied strain is shown schematically in figure 3.14. Different regimes where the filaments are either under compression or under tensile strain are pointed out in the figure. The dependence of the critical current on tensile strain and on the thermal history of the tape is indicated.
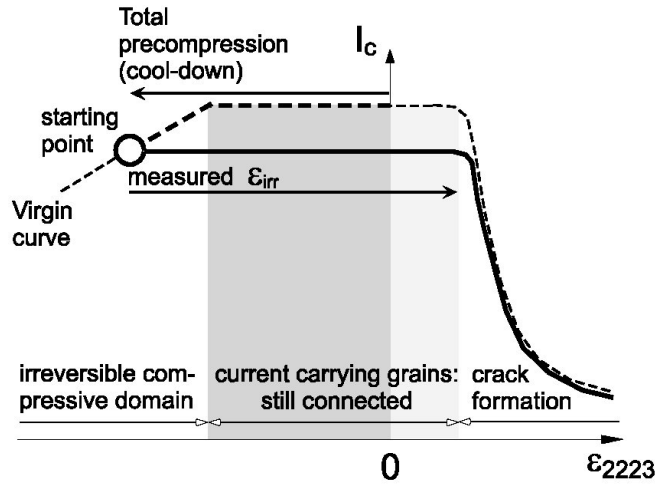
Figure 3.14. Schematic representation of the dependence of I_c of Bi-2223 tapes on applied strain. Courtesy of R. Passerini.
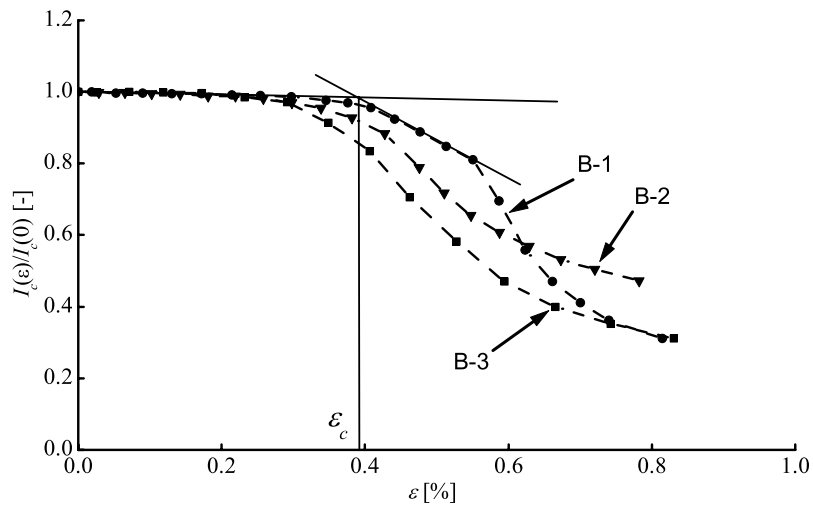
Figure 3.15. Normalized critical currents at self-field of Bi-2223 tapes B-1 and B-2 and Bi-2212 tape B-3 are shown as function of applied tensile strain. Samples B-1 and B-2 are measured at 77 K, while sample B-3 is measured at 4.2 K, due to its low I_c at 77 K. The solid lines indicate how the irreversible strain is obtained.

In order to study the effect of the different production processes (intermediate rolling steps, phase formation; section 3.3.3) of Bi-2223 and Bi-2212 tapes on their grain structure, the crack formation as function of applied strain is compared. The dependence of the critical current of Bi-2223 and Bi-2212 tapes on applied strain is measured on the

brass bending spring, as is described in section 2.1.2. The critical current of Bi-2223 tapes (samples B-1 and B-2) and Bi-2212 tapes (sample B-3) degrades irreversible when strain is applied (figure 3.15). Both Bi-2223 tapes vary in number of filaments and filament width and are chosen in order to study the influence of the filament configuration on the formation of cracks. The relevant sample properties are listed in table 3.1.

The critical current of the tapes is measured each time the applied strain is increased. The normalized critical current of the three samples show a similar dependence on applied strain. The three samples show a small irreversible degradation in critical current of -13 % per % strain before the critical strain is reached. This degradation is most likely due to the release of precompression which causes damage to the grain structure on a sub-micrometer scale. The critical strain is defined as the strain at which the first large decrease in critical current occurs, and is indicated by the solid lines in the figure. The Bi-2223 tapes with an AgMg matrix (sample B-1) and with silver matrix (sample B-2) both show a critical strain of approximately 0.4 %. Similar behavior in critical current as function of applied strain is observed in the Bi-2212 tape, where the critical strain is 0.3 %. Although strain is applied to Bi-2223 tapes at 77 K, while this is done at 4.2 K for the Bi-2212 tape, the difference in critical strain is mainly caused by the sample configuration and not by the difference in precompression. The thermal expansion becomes nearly zero below 100 K [50].

Information regarding the mechanical strength of the weak links in the current path of Bi-2223 tapes is obtained when the strain-dependence of the critical current is measured at various magnetic fields. The critical current density of Bi-2223 tape B-7 (table 4.1), normalized to its value at zero strain, is shown as function of tensile strain for magnetic fields ranging from 0.02 T to 0.28 T (figure 3.16). The magnetic field is applied perpendicular to the wide side of the tape. The critical current at low magnetic field degrades faster than at high field due to the application of strain after the critical strain is exceeded. It is concluded from these data that the weak links in the current path are also mechanically weak [35,37]. The initial degradation in critical current, which is observed before the critical strain is reached, is independent of magnetic field and is therefore not correlated to the weak links in the current path. For this reason the formation of cracks in Bi-based tapes is studied with MOI at an applied strain which exceeds ε_c. The results are presented in the next sections.
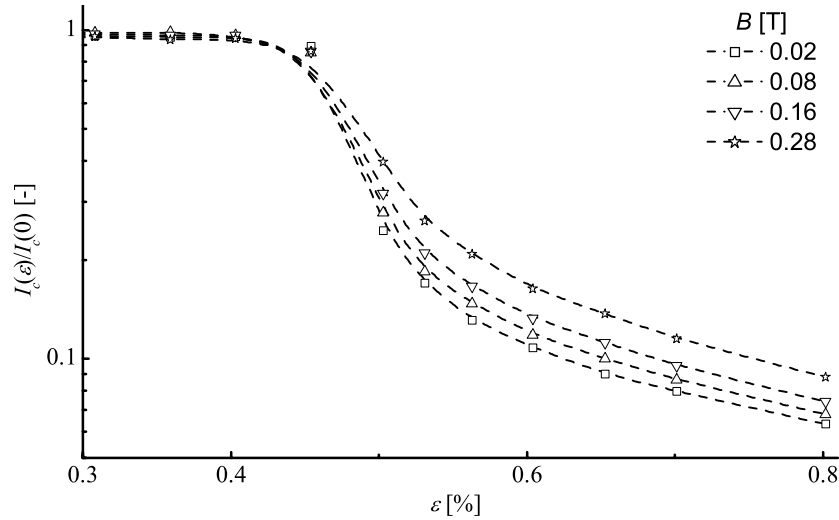
Figure 3.16. The critical current as function of strain of Bi-2223 tape B-7, measured with the transport current method for different magnetic fields at 77 K. The magnetic field is applied perpendicular to the wide side of the tape. The critical current is normalized to its value at zero strain. The dashed lines are a guide to the eye.

3.3.2. Crack formation in Bi-2223 tapes

The location of the weak links in the current path of Bi-2223 tapes is investigated by visualizing the formation and propagation of cracks in the grain structure due to applied strain with MOI. As is discussed in section 3.1, the irreversible degradation of the critical current occurs first in the weakly-linked network when the applied strain exceeds the critical strain. It is investigated whether microcracks that are related to the production process are visible with MOI before strain is applied and whether cracks develop before the critical strain is reached.

Earlier studies where MOI is applied in order to visualize the effect of applied strain on the grain structure of Bi-2223 tapes were performed by bending the mono-core tapes at room temperature [51,52]. The MO-images were taken after the tape is cooled to low temperatures. The effect of thermal cycling on the crack patterns in these experiments is not known. This unknown factor is eliminated in this work by applying the strain only when the sample is already at low temperature so that MOI can be taken simultaneously (in-situ). This way, a direct correlation between the damage in the grain structure and the degradation of the critical current is obtained.

Two sets of multifilament Bi-2223 tapes (B-1 and B-2) are investigated, which consist of a different number of filaments and filament configuration. The sample details are listed in table 3.1. The tapes are chosen in order to investigate the influence of the

filament structure on the crack formation and propagation as well. The formation of cracks is compared to the degradation in critical current and is related to the production process. The effect of longitudinal strain on the grain structure of sample B-1 is shown in figure 3.17. The silver matrix is partly removed to increase the resolution of the image.
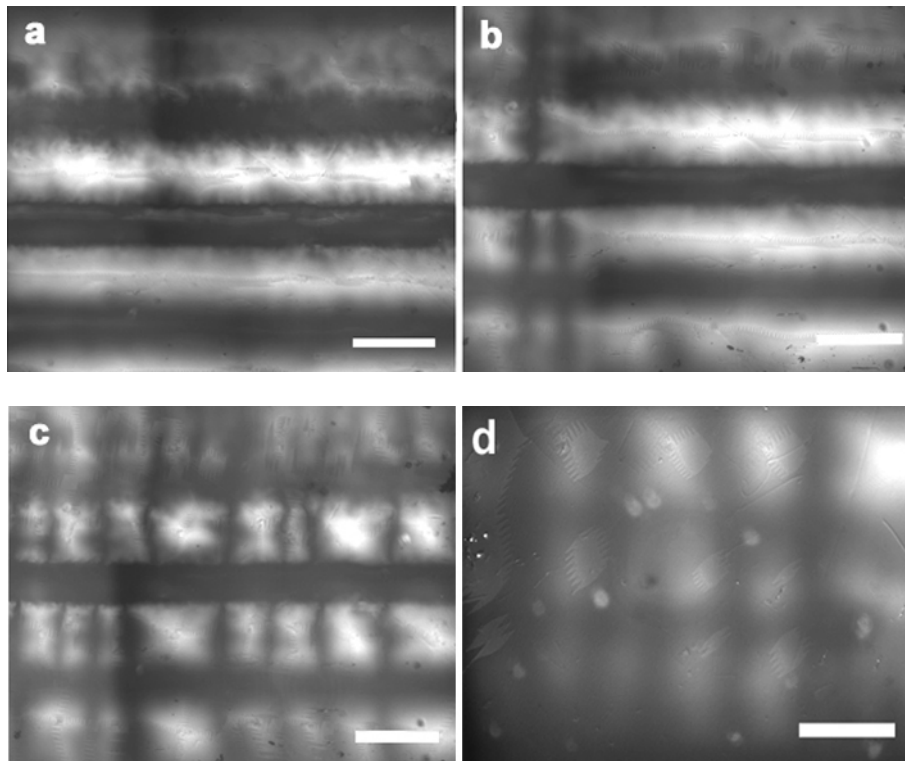
Figure 3.17. MO-images of Bi-2223 tape B-1 after flux is trapped at 120 mT. In the unstrained and etched tape (a), shielding currents are running along the entire filaments, trapping flux in the superconducting filaments. When strain is applied (b), cracks that interrupt the current appear in the filaments and flux is released. (c) Additional cracks develop in the filaments after more strain is applied. (d) MO-image of tape B-1 where the sheath material is not removed, after the applied strain exceeds 1%. The scale bar in the images is 500 μm.

Figure 3.17a shows the MO-image before strain is applied. The tape is cooled down to 30 K and magnetic flux is trapped in the superconducting filaments by applying a magnetic field of 120 mT, perpendicular to the tape surface. The magnetic flux in the superconducting filaments, indicated by the bright areas, is clearly visible in the unstrained tape. Dark areas correspond to the absence of flux. The filaments run horizontally in the image and are completely penetrated by magnetic field. Three complete filaments are visible, while half of a fourth filament can be seen at the bottom of

the image. Filaments from layers deeper in the tape are not visible. Structures in the flux are seen, which indicates that the filaments are not perfectly homogeneous, even in the case where no strain is applied to the sample. The fine structures may correspond to the presence of either micro-cracks, boundaries between colonies of well-connected grains, or variations in filament width or thickness. The fine structures are not observed in filaments that are located deeper in the tape, which is due to a decrease in resolution of the technique when the distance between indicator film and filament is increased.

Cracks develop when tensile strain is applied to a Bi-2223 tape and are visualized with MOI. Areas where no flux is present are observed after the sample is strained, as is seen in figure 3.17b. It is assumed here that this corresponds to a crack in the filament. Shielding currents that ran over the entire length of the filaments are stopped at cracks and flux is released at these locations. Cracks appear as dark lines in the image. The trapping of magnetic flux in filaments by shielding currents is presented schematically in figure 3.18.
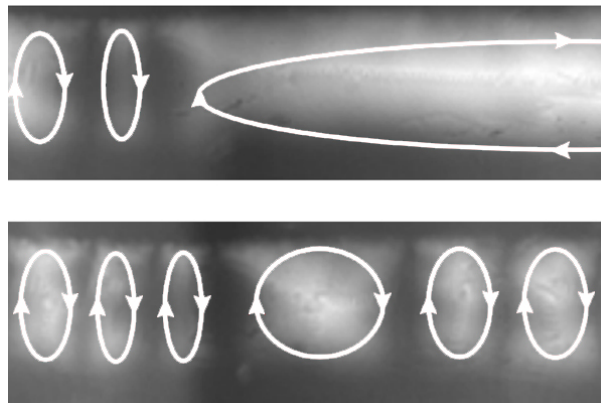
Figure 3.18. MO-image of a single filament in Bi-2223 tape B-1 shown in figures 3.17b and c. The shielding currents that run in the filaments are blocked by the cracks in the grain structure, as is indicated in the figure.

More cracks appear after the strain is increased. New cracks are developing in filaments that already show cracks at low strain (figure 3.17c). The filaments in the tape show multiple fractures and the amount of cracks in each filament increases with increasing strain. Also it is clearly observed that cracks initiated in one filament propagate to neighboring filaments and finally appear as tape-wide cracks.

In order to ensure that the etching of the silver matrix has no effect on the crack pattern, an intact sample is strained as well. Figure 3.17d shows the resulting MO-image after approximately 1% of strain is applied to the sample, which is more than twice the critical strain. The microstructural details that were visible in the MO-image of the etched

sample are absent, but the crack pattern is clearly seen and identical to the one of the etched sample. The effect of the silver matrix (distance between indicator film and filaments) on the image resolution becomes clear from this comparison. The strain at which cracks appear in the sample is measured with a strain gage, which is explained in more detail in chapter 2. The first three cracks appear at strains of 0.65 %, 0.73 % and 0.77 % respectively, as is also listed in table 3.2.

	1st crack [%]	2nd crack [%]	3rd crack [%]	ε_c [%]
B-1	0.65	0.73	0.77	0.4
B-2	0.61	0.91	-	0.4
B-3	0.41	0.48	0.70	0.3

Table 3.2. Strain at which the first cracks in Bi-based tapes are observed with MOI.

Although the cracks appear at arbitrary positions at low strain, some periodicity in crack positions appears at higher strain. This is confirmed when the number of cracks and the average distance between cracks are regarded. Figure 3.19a shows the number of cracks that appear in one filament of sample B-1 over 3 mm of its length. The average distance between cracks is calculated by dividing the length of the filament by the number of cracks that is observed and is shown in figure 3.19b.
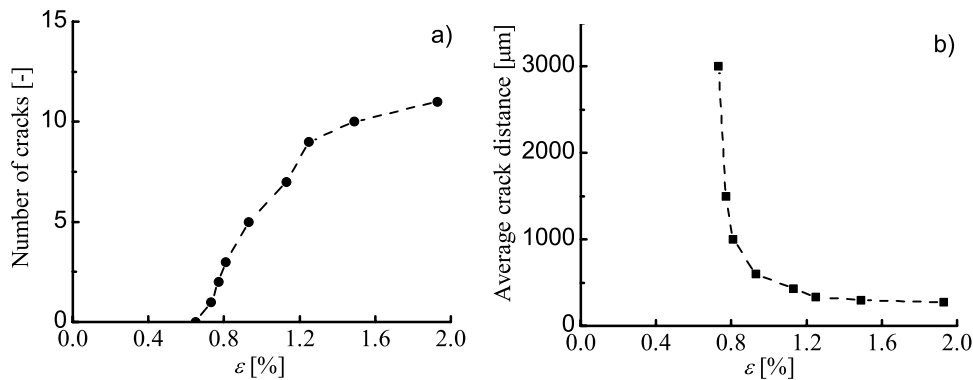
Figure 3.19. a) Number of cracks that appear in one of the top filaments in sample B-1 as function of strain. b) Average distance between cracks, calculated by dividing the filament length by the number of observed cracks. The dashed line is a guide to the eye.

The rate at which cracks appear decreases when the strain is increased. The average crack distance converges to a value of approximately 250 µm. The width of the filaments in sample B-2 is approximately 200 µm, resulting in square-shaped filament

fragments. The filament width of sample B-1 is approximately 450 μm, but the average distance between cracks is still 250 μm and corresponds well to the size of the fragments found in ultra-sonic fracturing experiments [39]. It is therefore concluded that the mechanically weak links in the filaments of Bi-2223 tapes are responsible for the location at which cracks appear and not the grain structure of the matrix.

Although no large variations in flux trapping or shielding in Bi-2223 tape B-1 are seen before strain is applied, this is not the case for Bi-2223 tape B-2. Variations in the intensity of flux shielding are observed, even before strain is applied (figure 3.20). The silver matrix is removed by etching and a magnetic field of 25 mT is applied perpendicular to the tape surface when the image is taken.

Figure 3.20a shows the MO-image after approximately 1% of strain is applied. A large number of cracks are present in the filaments. Electrically well-connected superconducting regions are shielding the external magnetic field and are dark in the image. The areas where the applied magnetic field penetrates between the filaments and through cracks appear bright in the image. Part of a filament of sample B-2 in figure 3.20a is shown in detail in figure 3.20b, before strain is applied. Areas with a low critical current density are visible in this image. It is shown in figure 3.20c, where the same area is enlarged after strain is applied, that those areas form filament-wide cracks when strain is applied. The levels of applied strain at which the first two cracks appear are measured with a strain gage on an intact sample and are 0.61 % and 0.91 % respectively (table 3.2). Figure 3.21 shows an ESEM image of one of the top filaments of sample B-2, after strain is applied. A clear crack is observed in the image. Also the grain structure is seen clearly.
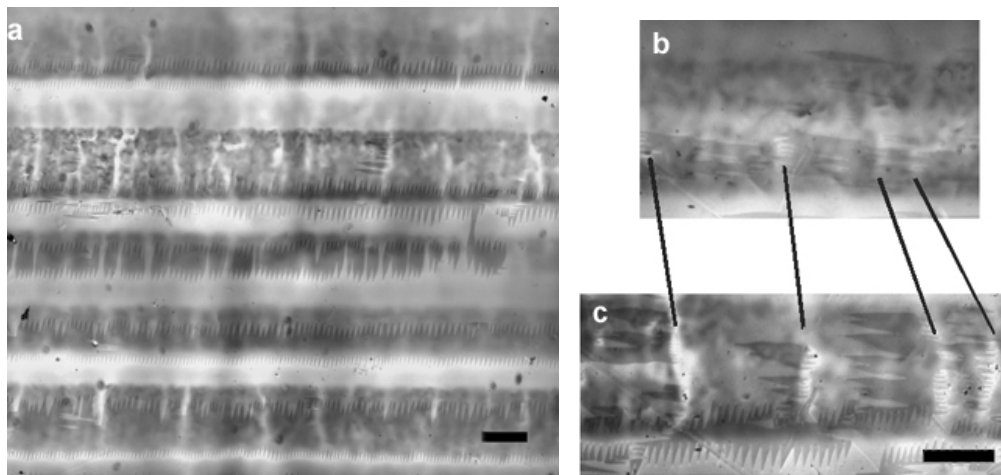
Figure 3.20. (a) MO-image of Bi-2223 tape B-2 after strain is applied. A magnetic field of 25 mT is applied when the image is taken. The MO-image of a specific area in a single filament of sample B-2 is shown in detail, (b) before and (c) after strain is applied. The scale bar in both images is 125 μm.
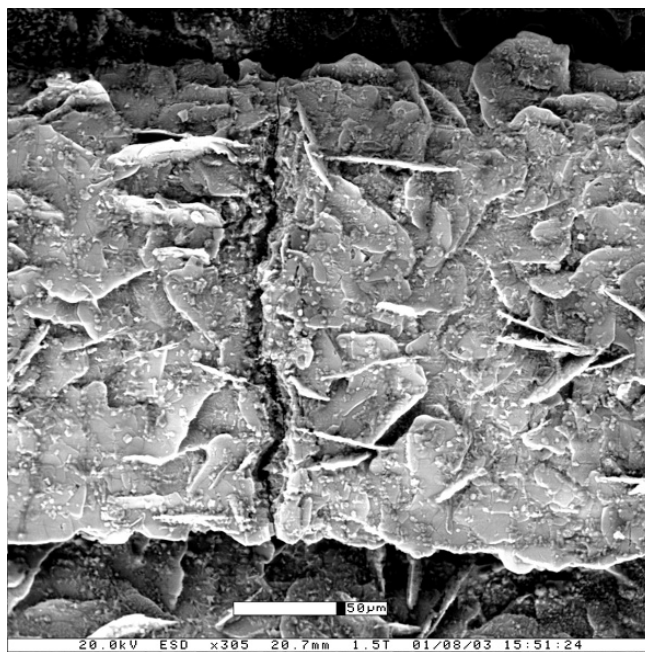
Figure 3.21. ESEM-image of the top of one filament of sample B-2, after it is strained within the MOI-setup. The silver matrix is removed by etching in order to reveal the grain structure.

The locations where flux is partly penetrating the filaments before strain is applied correspond to microcracks that are formed in the intermediate rolling steps during the production process. They are partly healed by subsequent heat treatments and form mechanically weak spots. MOI studies on Bi-2223 tapes confirm that the grain structure is influenced by the deformation steps in the production process [53]. In Bi-2223 tapes, the phase formation involves localized melting of grains, which depends on local conditions [54]. Intermediate rolling steps are needed to increase the density of the filaments. When tapes are rolled in between heat treatments, a large number of microcracks are introduced that run transverse to the rolling direction. When the deformation is applied by pressing, the microcracks mainly run in the longitudinal direction of the tape [55].

In order to compare the crack formation in Bi-2223 tapes observed with MOI at 30 K and the degradation in I_c at 77 K, the difference in precompression must be taken into account. Because the sample in the MOI setup is not mounted on a substrate, the precompression is entirely determined by the temperature and the sample itself. The precompression is directly measured with the strain gage that is mounted on the sample [56]. The precompression of the filaments in the sample when the brass bending spring is applied is largely determined by the bending spring itself and the temperature at which the

sample is soldered to the spring. The precompression is calculated using the difference in thermal expansion coefficient between brass and the ceramic Bi-core. The resulting difference in pre-compression of two Bi-2223 tapes (samples B-1 and B-2) is shown by a shift in the I_c-ε curves (figure 3.22). The shift for sample B-1 is 0.10 % and 0.17 % for sample B-2. The cracks in the grain structure of both Bi-2223 tapes that are visualized with MOI occur at a strain level exceeding the critical strain. This is confirmed when the crack formation is compared to the degradation in I_c.
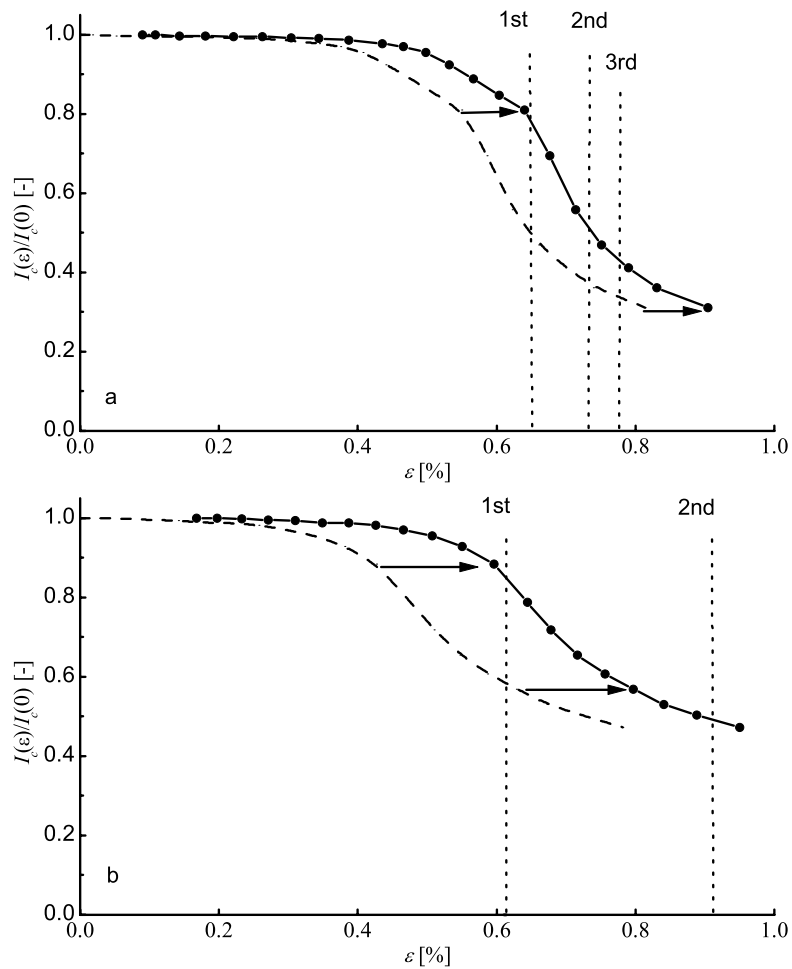
Figure 3.22. Normalized critical current vs. strain of Bi-2223 tapes. a) Degradation in I_c of sample B-1 at 77 K, compared to the results from the MOI experiment at 30 K. The dashed line is the normalized critical current before the difference in pre-compression between both experiments is taken into account. The observed cracks are at applied strain of 0.65 % (1st), 0.73 % (2nd) and 0.77 % (3rd). b) Sample B-2; cracks appear at 0.61 % (1st) and 0.91 % (2nd).

When the formation of cracks observed with MOI is compared to the degradation of the critical current as function of applied strain, some differences are evident. The first cracks are observed at higher strain levels than the critical strain that is determined by the bending spring, even after the difference in pre-compression is taken into account. This is clearly seen in figure 3.22, where the strain at which the first cracks appear is shown by the dashed lines. When the strain is increased, the critical current of the tapes degrades by approximately 10-20 % before a substantial change in flux in the filaments is observed with MOI. The initial decrease may be caused by microcracks, with a size too small to be observed by MOI. The thickness and roughness of the filaments is responsible for a relatively large distance between the indicator film and the location in the grain structure where possible microcracks appear.

A small degradation in critical current as function of strain is observed before the critical strain is reached, but no apparent differences between the critical current at low- and high field are reported. The damage in the grain structure at low strain is not concentrated at weak links in the current path. The concentration at weak links only occurs at high levels of strain. It is therefore concluded that the locations at which damage to the grain structure is observed with MOI correspond to the weak links in the current path and are related to microcracks induced by the intermediate rolling steps in the production process.

3.3.3. Crack formation in Bi-2212 tapes

An important conclusion presented in the previous section is that intermediate rolling steps in Bi-2223 tapes form mechanically and electrically weak connections in the grain structure. The intermediate rolling steps are absent in the production of the Bi-2212 tapes investigated here. Contrary to Bi-2223, the formation of Bi-2212 tapes involves a semi-congruent melting of the filaments and a subsequent re-crystallization, which results in a different grain structure [57,58]. In order to find the similarities and differences between the grain structure of Bi-2223 and Bi-2212 tapes, the formation of cracks in Bi-2212 tapes is investigated with MOI.

The best comparison between the crack formation in Bi-2212 and Bi-2223 tapes is made when multifilament tapes are selected of which the filaments are of comparable width. The configuration of the 0.5 mm wide filaments in the Bi-2212 tape that is selected in this study (sample B-3) is comparable to that of sample B-1. The properties of the sample are listed in table 3.1. The silver matrix is removed by etching to increase the resolution of the MO-images. Defects in the grain structure are observed even before strain is applied to the tape, as is seen clearly in the MO-image of figure 3.23.
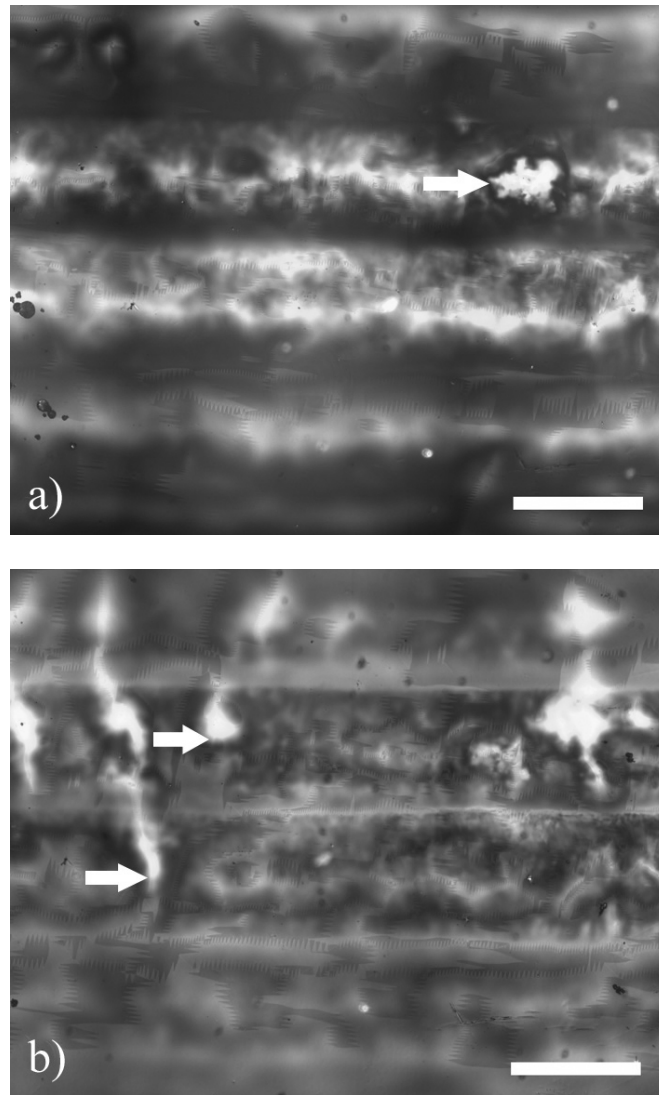
Figure 3.23. MO-image of Bi-2212 tape B-3. a) Flux is trapped at 120 mT before strain is applied. The arrow points to a pin hole where flux is concentrated. b) MO-image in the presence of a magnetic field of 25 mT, after the tape is strained. The arrows point to cracks that only partly propagate into the filaments. The scale bar is 500 µm.

Magnetic flux is trapped at 120 mT at 30 K before the image is taken. Four filaments that run horizontally in the MO-image are visible. The areas between the filaments are dark, due to the absence of flux. The arrow points to an area where flux is concentrated. This is a so-called pin hole where the high carbon content of the precursor powder resulted in a bubble during the melting process [59]. Flux trapped in the filaments

returns through such a pin hole. The ESEM image of a pin hole is shown in figure 3.24, where a clear difference between the grain structure of the pin hole and its surroundings is seen. Cracks in the Bi-2212 filaments appear when strain is applied to the tape. The MO-image of the strained tape is shown in figure 3.23b, while a magnetic field of 25 mT is applied perpendicular to the tape surface when the image is taken. Cracks appear bright in the image, due to penetrating magnetic flux. Some cracks run through part of the filaments, without breaking them completely (arrows in figure 3.23b).
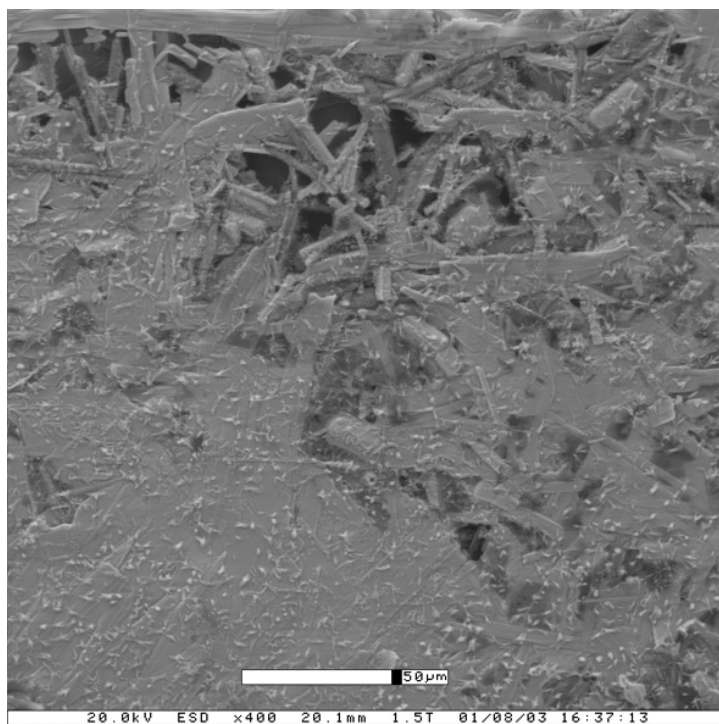
Figure 3.24. ESEM-image of the top of one filament of Bi-2212 tape B-3 showing a pin hole. The silver matrix is removed by etching in order to reveal the grain structure.

Although the configuration and dimensions of the filaments are comparable, differences are observed in the crack structure of Bi-2212 tape B-3, compared to that in Bi-2223 tapes. Most of the cracks that develop in the Bi-2212 tape under tensile strain propagate slowly through the filaments when the applied strain is increased. The arrows in figure 3.23b show cracks that only run through part of the filament. This indicates that the mechanically weak links in the filaments of Bi-2212 tapes do not run across the entire width of the filament, as is the case with Bi-2223 tapes, but are confined to particular areas in the filaments. Weak spots are most likely formed by locations where the grain structure is less dense.

In order to reveal at what level of strain the cracks appears, compared to the degradation in critical current, the applied strain is measured with a strain gage that is glued on the sample (section 2.3.4). The values of applied strain at which the first three cracks appear are 0.41 %, 0.75 % and 0.77 % respectively, as is listed in table 3.2. When the degradation in I_c as function of strain that is measured on the brass bending spring at 4.2 K is compared to the formation of cracks, it is observed that the first crack in the grain structure appears when the critical current degraded by approximately 30 % (see figure 3.25). The damage to the grain structure that causes the initial decrease is not observed in the MO-image due to the relatively low resolution of MOI. A shift of -0.04 % in the I_c-ε curve of figure 3.25 is due to the difference in precompression of the filaments between both experimental techniques.
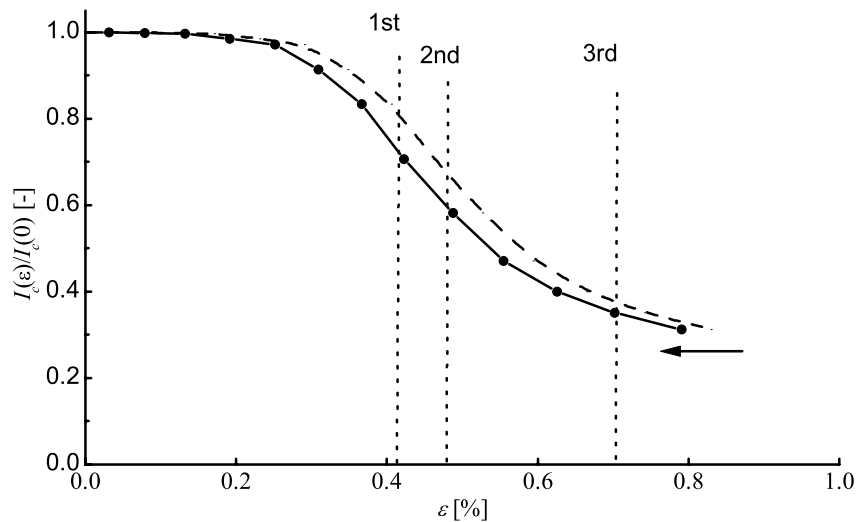
Figure 3.25. Normalized critical current vs. strain of Bi-2212 tape B-3 at 4.2 K. Cracks appear at applied strain of 0.41 % (1st), 0.48 % (2nd) and 0.70 % (3rd). The arrow shows the direction in which the curve shifts when correcting for the difference in pre-compression.

3.3.4. Crack formation in YBCO coated conductors

The grain structure of YBCO coated conductors and Bi-based tapes are in many ways different. The superconducting YBCO layer is orders in magnitude thinner than the metal substrate. It is therefore expected that damage to the grain structure due to tensile strain is mostly influenced by the substrate and not by the superconducting layer. To clarify the similarities and differences in grain structure between YBCO coated conductors and Bi-based tapes, magneto-optical imaging is applied to study the crack formation as function of longitudinal strain.

Not much experimental data on the dependence of the critical current on tensile strain in YBCO is available [60]. Here, the degradation in I_c as function of applied tensile strain of a YBCO coated conductor that is produced with PLD (Y-1) is compared to that of a Bi-2223 tape (B-2) [61]. A similar degradation in critical current at 77 K is measured as is the case with Bi-based tapes (figure 3.26). The critical current of the YBCO coated conductor decreases irreversibly by 13 % per % strain at low strain and by 94 % per % strain when the critical strain is exceeded. The critical strain is 0.45 %, which is comparable to what is measured for in Bi-based tapes. The strain dependence of the critical current of Bi-2223 tape B-2 is included in the figure.
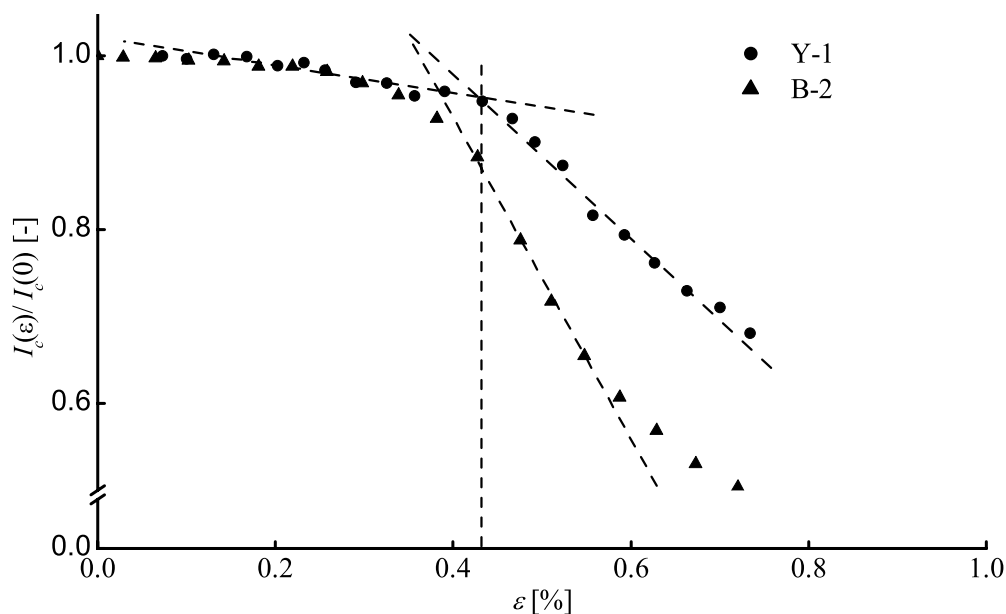
Figure 3.26. Normalized critical current versus applied strain of samples Y-1 and B-2, measured at 77 K on the brass bending spring. The vertical dashed lines indicate the change in slope of the I_c-ε curve of sample Y-1 when the applied strain exceeds the critical strain.

The main difference compared to Bi-based tapes is the more gradual degradation in critical current of YBCO coated conductors above the critical strain. The critical current of sample Y-1 is decreased by approximately 30 % of its original value at an applied strain of 1.5 times the critical strain, while that of sampled B-2 degraded by 50 %. The difference is explained by visualizing the crack formation in YBCO coated conductors with MOI. The trapped flux in the colony structure of YBCO coated conductor Y-1 is shown in figure 3.27a, before strain is applied.
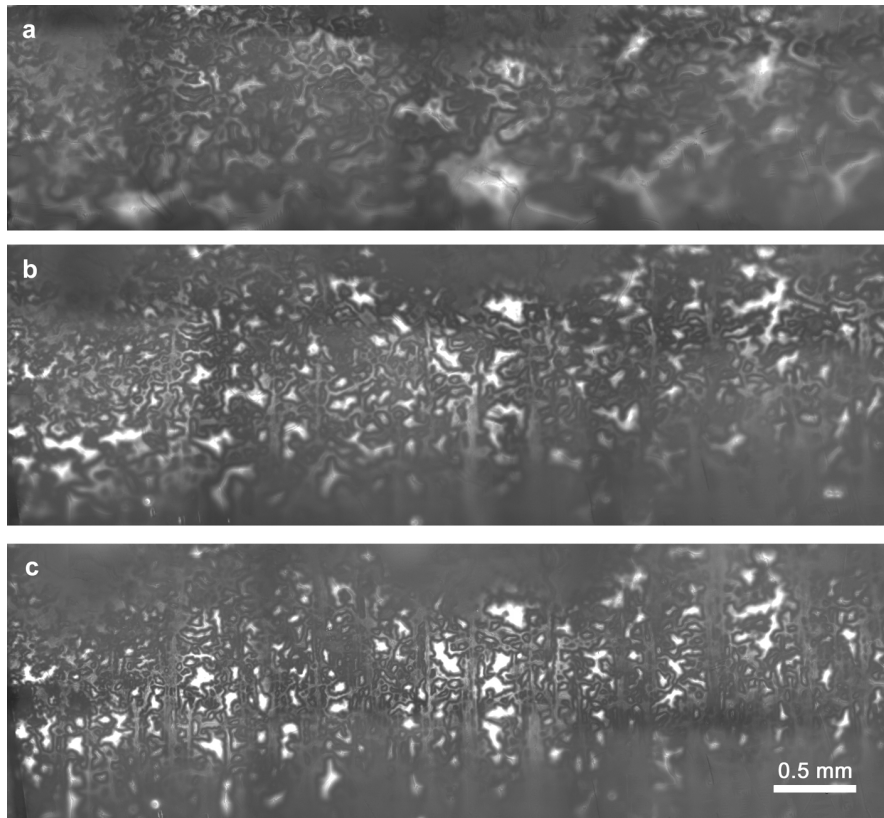
Figure 3.27. MO-image at 30 K of sample Y-1 after flux is trapped at 120 mT. a) The superconducting colonies are clearly visible before strain is applied and b) Cracks appear after the applied strain exceeds the critical strain. c) More cracks develop after even more strain is applied.

Magnetic flux is trapped in the superconducting colonies of well-connected grains by applying a magnetic field of 120 mT at 30 K and removing it before the image is taken. A similar image as in figure 3.4b is obtained where colonies of well-connected grains appear bright due to the trapped flux, while the grain boundaries appear dark. Cracks in the grain structure of the conductor appear after tensile strain exceeds the critical strain (figures 3.27b and 3.27c). The cracks are directed perpendicular to the longitudinal direction of the sample, similar to the cracks in Bi-based tapes. The colony structure of the YBCO layer in the tape does not influence the crack locations. A large number of cracks cutting through superconducting colonies appear, which indicate that in this material the crack formation is determined by the nickel substrate that consists of nickel grains with an average size of 50-100 μm [62].

The crack formation and propagation in YBCO coated conductors is seen even more clearly when a magnetic field of 25 mT is applied at the moment the MO-image is

taken. Colonies remain shielded from the external magnetic field, while the field penetrates the high-angle colony boundaries and cracks in the YBCO layer (figure 3.28). Part of the sample shown in figure 3.27c is enlarged, where groups of cracks are developing in the YBCO layer. The distance between the groups ranges from approximately 50 µm to 250 µm. The minimum distance between cracks within a group is around 10 µm. Cracks do not run sample-wide, as indicated by the arrows in the figure.
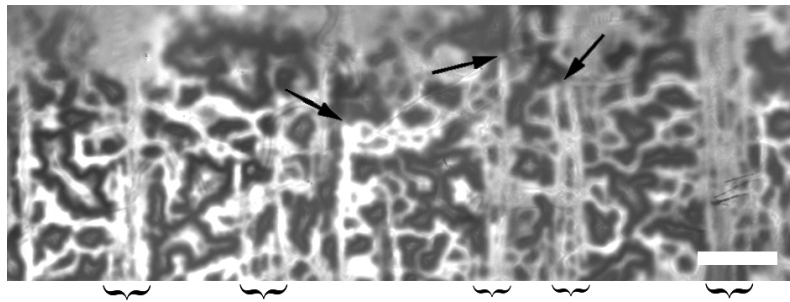
Figure 3.28. MO-image of a strained YBCO coated conductor (sample Y-1). An external magnetic field of 25 mT is applied perpendicular to the tape surface. Flux penetrates through high-angle boundaries and cracks. The brackets indicate groups of cracks. The arrows point to colonies where cracks are stopped at. The scale bar is 150 µm.
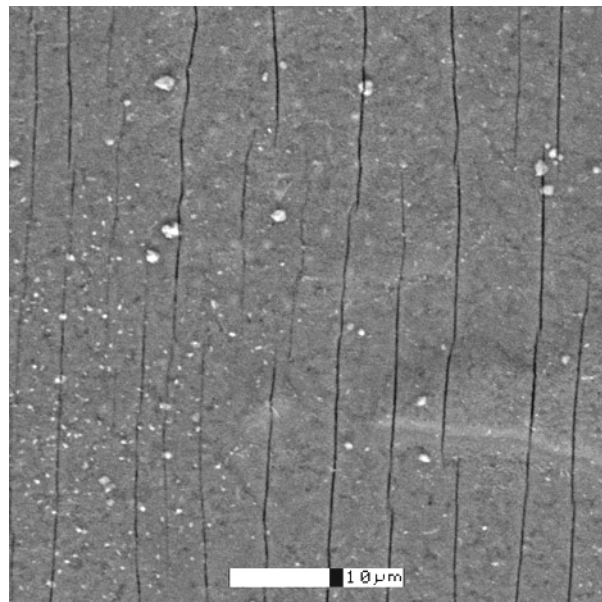
Figure 3.29. ESEM-image of YBCO coated conductor Y-1, after the sample is strained in the MOI-setup. The silver cap layer is removed by etching. Cracks that run transverse to the direction of the applied strain are clearly visible. Most of the cracks do not run over the entire width of the sample.

The ESEM-image of a typical group of cracks in the YBCO layer after deformation is presented after the silver cap layer of the conductor is removed by chemical etching (figure 3.29). Cracks run transverse to the longitudinal direction of the conductor. The average distance between cracks is only a couple of micrometers, which is much smaller than the distance between cracks observed with MOI. This is explained by the limited resolution of the MO-technique. Only larger cracks not shown in the ESEM-image can be observed with MOI. The formation of microcracks in Bi-2223 tapes before the critical strain is reached can not be visualized with MOI for the same reason.

Another indication that the crack formation in YBCO coated conductors is entirely determined by the substrate is obtained when strain is applied to a bridge-shaped sample. The configuration of such a bridge is illustrated in figure 3.30, together with the MO-image of the flux trapped in the colonies at 30 K (sample Y-1). Flux is trapped at 120 mT before strain is applied along the direction of the bridge. The image is taken after strain is applied. The most striking result is that the cracks in the YBCO layer are not directed transverse to the direction in which strain is applied, but follow the curvature of the bridge.
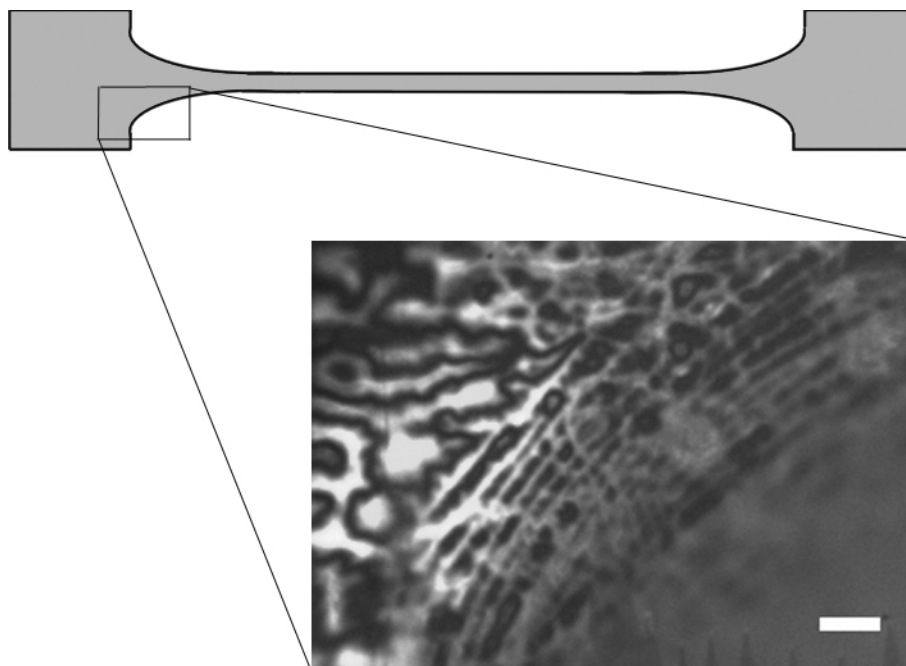
Figure 3.30. MO-image of sample Y-1 that is cut into a narrow bridge. The sample is strained at 30 K and the crack pattern is visualized by trapping flux in the superconducting colonies. The scale bar is 50 μm.

3.3.5. Conclusions on crack formation

The main difference between the formation of cracks in YBCO coated conductors, Bi-2212 tapes and Bi-2223 tapes is that cracks in Bi-2223 tapes always run across the entire width of the sample. Cracks in the coated conductors investigated here often terminate in the interior of the sample, therefore, only partly interrupt the path of a transport current. This explains the slower degradation in critical current as function of applied strain in YBCO coated conductors, at strain levels exceeding the critical strain. The difference in crack pattern is explained by differences in production process and conductor structure.

The fact that cracks are not affected by the YBCO layer gives rise to the assumption that the degradation in critical current is independent of magnetic field. The weak links in the current path of the YBCO layer are not affected in a larger extend than the strongly-linked backbone, as is the case with Bi-2223 tapes. Similar strain dependence is expected in Bi-2212 tapes because the mechanical weak links are not formed by colony boundaries but by less dense areas in the filaments. Both expectations can be verified by measuring the magnetic field and strain dependence of the critical current of the conductors.

3.4. Conclusions

Three main conclusions can be drawn from the results presented in this chapter. The first main conclusion is that clusters of grain boundaries and large defects are responsible for blocking the current in YBCO coated conductors on a macroscopic level. This is concluded from a comparison of the spatial distribution in critical current density, measured with the magnetic knife, and the local flux penetration that is visualized with magneto-optical imaging. Several observations are made:

- Spatial variations of 100 % in critical current density on a length scale of approximately 100 μm are observed in YBCO coated conductors that are produced with pulsed-laser deposition.
- Local minima in the critical current density correspond to large clusters of grain boundaries observed with magneto-optical imaging.
- Current in YBCO coated conductors does not run in one-dimensional current paths. Grain boundaries and defects that are directed along the direction of the transport current limit the critical current density. Current meanders around the defects and large grain boundaries on a length scale of approximately 50-100 μm, which results in two-dimensional current paths.

- Spatial variations in critical current density of only 20-30 % together with a more graduate flux penetration in the grain structure are observed in YBCO coated conductors that are produced with metal-organic-deposition. A better grain connectivity and a thicker YBCO layer provide superconducting currents with additional current paths to get around defects.

The second main conclusion is that weak links in the current path of Bi-2223 tapes are formed by mechanically weak spots in the grain structure, which form cracks when the tensile strain exceeds the critical strain. The locations of the weak links are identified indirectly by combining magneto-optical imaging and the application of tensile strain. A comparison between crack formation in Bi-2223 and Bi-2212 tapes is made and the differences are attributed to differences in the production process:

- The locations where cracks in Bi-2223 and Bi-2212 tapes develop are determined by the mechanically weak links in the filaments and not by the matrix.
- The main difference between the two Bi-based tapes is that the weak links in Bi-2223 tapes are formed by microcracks that are due to intermediate rolling steps. The cracks are only partly healed by the subsequent heat treatment.
- Partly-healed cracks in Bi-2223 tapes are visible before strain is applied.
- The first cracks in the filaments of Bi-based tapes are observed with MOI after the critical strain is reached.
- The weak spots in Bi-2212 tapes studied in this thesis are caused by variations in the grain structure that are due to the local reaction conditions and not by intermediate rolling steps, which are absent in the production process.
- A slower propagation of cracks under tensile strain in the filaments of Bi-2212 tapes is observed which is correlated to localized mechanical weak spots.
- It is expected that tensile strain affects weak links in the current path of Bi-2212 tapes in a similar way as the strongly-linked grains. The assumption has to be verified by studying the dependence of the critical current on magnetic field and tensile strain.

The third main conclusion is that the formation and propagation of cracks in YBCO coated conductors is entirely determined by the substrate and not by the YBCO layer. Cracks cut through colonies of well-connected grains, which forms the main difference in crack formation compared to Bi-based tapes:

- A smaller degradation in critical current in YBCO coated conductors compared to Bi-based tapes is measured, after the critical strain is exceeded.
- The more gradual degradation in critical current is explained by the fact that cracks in the YBCO layer do not run across the entire width of the conductor and

leave part of its cross-section untouched, providing a transport current with additional pathways to meander around cracks.

- It is expected from the observed crack pattern in YBCO coated conductors that tensile strain affects the weak links in the current path to the same extend as the strongly-linked backbone. This has to be confirmed by studying the dependence of the critical current on magnetic field and tensile strain.

The critical current should be measured within the MOI-setup to make a more accurate comparison between crack formation and degradation in critical current as function of tensile strain possible.

4. Separation of current limiting mechanisms in Bi-2223

The nature of the dissipation mechanisms in Bi-2223 tapes is clarified by analyzing the magnetic field and temperature dependence of the critical current density in detail. First, an overview of several existing models that describe current flow in these polycrystalline tapes is presented. The magnetic field and temperature dependence of the critical current density for different field angles is investigated experimentally, using transport- and dc-magnetization methods. The results show that two separate mechanisms limit the local current in Bi-2223 tapes and that the parallel path model, with current running in two paths, is applicable. The contributions of both current paths to the overall critical current density are separated by measuring the magnetization of aligned Bi-2223 powder. The current limiting mechanism in high magnetic field is confirmed to be intra-granular flux motion. The magnetic response can be satisfactory described using classical flux creep theory with a logarithmic dependence of the pinning potential on current. The specific field dependence of the critical current density of the weakly-linked network in Bi-2223 tapes leads to the conclusion that dissipation is due to inter-granular flux motion at low-angle grain boundaries. High-angle grain boundaries that form Josephson weak links do not significantly contribute to the overall current.

4.1. Current flow in Bi-2223 tapes

Poor grain connectivity in YBCO coated conductors not only results in a suppression of the critical current on a micrometer scale (flux penetration chapter 3), but also results in a reduced critical current density on a length scale of several millimeters (magnetic knife experiment). The question whether a link exists between the mechanisms that limit the critical current density and the grain structure in Bi-2223 tapes is addressed by presenting a brief overview of existing models. According to the brick-wall model, current flow is limited by poor grain connectivity in the *ab*-plane of the tape, while the railway switch model argues that current is carried in the *ab*-direction across low-angle grain boundaries and is limited by the large anisotropy of the grains. Finally the parallel path model describes current flow as running in chains of well-connected grains in parallel with a network of weakly-linked grains, without making assumptions regarding the location of the current paths.

The critical current density of Bi-2223 tapes decreases rapidly with increasing magnetic field, especially for magnetic fields applied perpendicular to the wide side of the tape [63]. The remaining critical current density decreases only slightly with increasing field, until a large magnetic field is applied where it decreases to zero. This so-called "double step" behavior of the critical current density as function of perpendicular magnetic field is shown at various temperatures for a Bi-2223 tape (sample B-4) in figure 4.1. The most important properties of the samples referenced to in this chapter are listed in table 4.1.
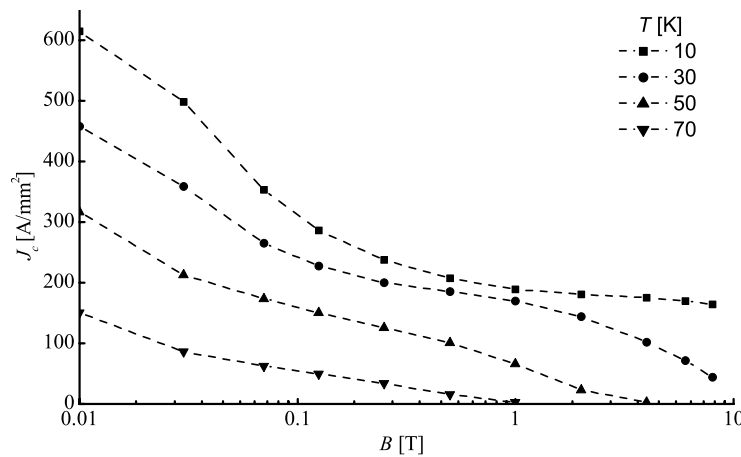
Figure 4.1. Critical current density of sample B-4 as function of magnetic field at various temperatures. The magnetic field is applied perpendicular to the wide side of the tape. The dashed lines are a guide to the eye.

	Matrix	Cross-section (mm^2)	I_c in self-field [A]
B-4	Ag	0.31	36 (77 K)
B-5	Ag	0.31	65 (77 K)
B-6	AgMg	0.18	30 (77 K)
B-7	Ag	0.39	135 (77 K)

Table 4.1. Relevant properties of the Bi-2223 tapes referred to in chapter 4.

Different approaches to describe the mechanisms that limit the critical current density of Bi-2223 tapes have been reported. The brick-wall model proposed by Bulaevskii considers colonies of well-connected grains which are arranged as bricks in a wall [64,65]. Current is limited in crossing from one brick to the next at the boundaries in the *ab*-direction. To bypass the boundaries between the grains, current is flowing in the *c*-direction within the colonies, and runs from one colony to the next over *c*-axis boundaries (figure 4.2). Current has to cross weakly-linked [001] twist boundaries where colonies partly overlap (OABTWIST, section 3.1) [66]. The twist boundaries do not degrade the critical current density in a larger extend than the weakly-linked CuO_2-planes within the grains that form the boundary [67,68,69]. Although weakly-linked CuO_2-planes are observed in Bi-2212 crystals by Kleiner [70,71], it is not clear whether this is also applies to Bi-2223 tapes.
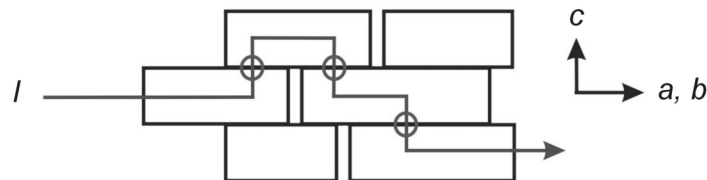
Figure 4.2. Current flow in Bi-2223 layers, according to the brick-wall model. Current cannot run freely across grain boundaries in the *ab*-direction but passes from one grain to the next in the *c*-direction. The circles indicate the OABTWIST boundaries for the sketched current path.

The brick-wall model is not convincingly proven by experimental data. The maximum critical current density along the *c*-axis of Bi-2212 single crystals in which the CuO_2-planes are fully decoupled is several orders of magnitude smaller than in Bi-2212 tapes. Also the critical current density of Bi-2223 tapes at zero field shows a linear temperature dependence, which is also observed in Bi-2212 thin films [72], while the critical current density of Bi-2212 crystals in the *c*-direction shows a much stronger temperature dependence. The discrepancies between experiment and the brick-wall model called for another approach to describe the current flow in Bi-based tapes. The railway switch model, proposed by Hensel, is based on the grain structure as observed in Bi-2223

filaments [21,73]. The colonies are well connected in the *ab*-direction across low-angle boundaries. The boundaries are strongly-linked and are not a significant barrier for the current. The critical current density is limited by the large anisotropy of the grains, and not by weak links. The most common boundaries found in Bi-2223 tapes are OABTWIST, edge-on *c*-axis tilt (ECTILT) and small-angle *c*-axis tilt (SCTILT) boundaries, as was shown in figure 3.2 in chapter 3. The current paths according to the railway switch model are shown in figure 4.3.
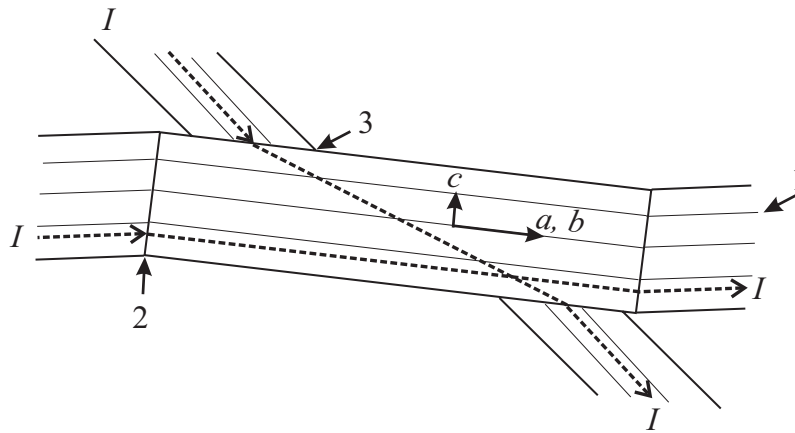
Figure 4.3. Current flow in Bi-2223 layers according to the railway switch model. Current flows from one colony of well-aligned grains to the next, crossing OABTWIST (1), ECTILT (2) and SCTILT (3) boundaries. The current is mainly obstructed by the large anisotropy of the grains.

Based on the double step behavior of the critical current density as function of magnetic field, Dhallé proposed a model where current in a Bi-2223 tape at low magnetic fields is carried by a network of weak links, in combination with a backbone of strongly-linked grains [74]. A supercurrent is no longer possible in the weakly-linked structure at higher magnetic fields, and is only carried by the backbone. This approach is used to develop a more detailed parallel path model in this study and partly published elsewhere [75,76,77]. The critical current density in the two parallel paths in the tape is limited by separate mechanisms, in order to explain the observed double step behavior in $J_c(B)$, shown in figure 4.1.

The parallel path model does not predict whether the weakly-linked network is formed by Josephson-type weak links, or by weak inter-granular flux pinning at low-angle grain boundaries. The critical current density of the weakly-linked current path decreases more rapidly as function of magnetic field than in the strongly-linked current path. Current in the strongly-linked backbone is not obstructed at low-angle boundaries, and the dissipating mechanism of this current path is therefore intra-granular flux pinning. The overall critical current density is defined by the sum of the weakly-linked network (J_{cw}) and the strongly-linked backbone (J_{cs}):

$$J_c(B,T) = J_{cw}(B,T) + J_{cs}(B,T). \qquad\qquad (4.1)$$

The parallel path model is applied in this chapter to describe the behavior of the critical current density of Bi-2223 tapes. Since the model does not couple the two current paths directly to the grain structure, the results of several experiments are analyzed to locate where the current limiting mechanisms in both current paths occurs.

4.2. Parallel path model in Bi-2223 tapes

To investigate whether the current paths described by the parallel path model can be coupled to the grain structure of Bi-2223 tapes, a separation of both current paths is made by analyzing the high-field behavior of the critical current density (section 4.2.1). The angular dependence of the critical current density of Bi-2223 tapes can not be described convincingly over a large temperature and magnetic field range. In section 4.2.2 it is investigated whether this dependence can be described accurately by taking the contributions of both current paths into account separately. The question whether a physical separation of the two current paths can be made is addressed in section 4.2.3 by preparing a single-grained sample in which the network of weakly-linked grains is no longer present. The critical current density of an intact tape is compared with that of the powder extracted from this tape in section 4.2.3.

4.2.1. Critical current according to the parallel path model

The high-field behavior of the critical current density in Bi-2223 tapes is investigated to separate the contributions of both current paths from the overall critical current density. At sufficiently high fields, the weakly-linked network does no longer contribute to the overall current. The measured critical current density is completely carried by the strongly-linked backbone in this field region. The behavior of the critical current density of this current path is described with an expression based on intra-granular flux pinning. The remaining critical current density at low field that is not taken into account by this expression is attributed to the weakly-linked network.

A large number of experiments have shown that the critical current density in Bi-2223 tapes in the high-field region follows an exponential decay as function of magnetic field [76]. This current density is attributed to the strongly-linked backbone and its behavior is determined by intra-granular flux pinning;

$$J_{cs}(B,T) = J_{cs}(0,T)\exp\left(-\frac{B}{B_{peak}(T)}\right). \tag{4.2}$$

The temperature dependent scaling field $B_{peak}(T)$ is an indication for the pinning force in the strongly-linked current path. Its value is obtained directly from experimental results, by deriving the macroscopic pinning force (F_p). The macroscopic pinning force is used by Kramer [78] to obtain the pinning properties of conventional type-II superconductors, and defined as:

$$F_p = \left| J_c \times B \right|. \tag{4.3}$$

The macroscopic pinning force shown in figure 4.4 for sample B-5 shows a maximum as function of magnetic field at B_{peak} (determined by a second order polynomial fit around the maximum).
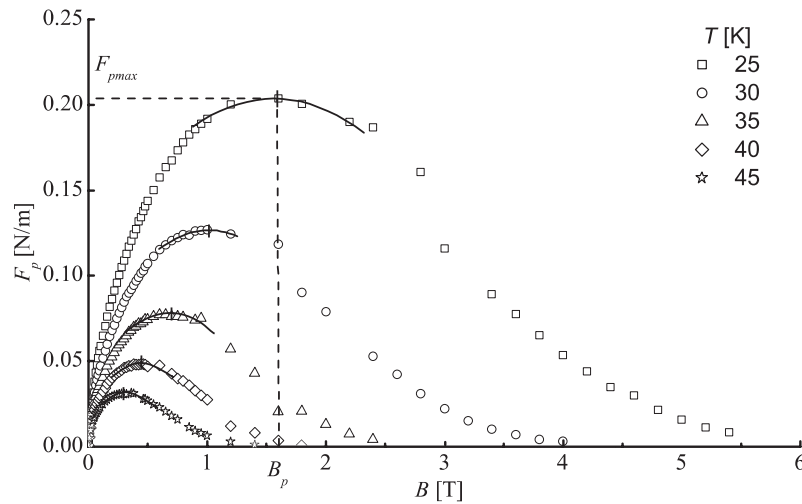
Figure 4.4. Macroscopic pinning force of sample B-5 as function of magnetic field for various temperatures. The magnetic field is applied perpendicular to the wide side of the tape. The solid lines are a second order polynomial fit around the maximum of the pinning force.

The macroscopic pinning force of the sample is calculated from the critical current density that is obtained from a dc-magnetization measurement (section 2.1.3). In the original Kramer analysis, flux motion occurs at fields below the peak field (B_{peak}) by flux line depinning and above the peak field by synchronous shear of the flux line lattice. However, here we use the position of the peak more generally, in order to select a temperature dependent scaling field and current to analyze our data. When J_c in

expression 4.3 is substituted by J_{cs} of the strongly-linked path and is normalized to the maximum pinning force F_{pmax}, which occurs at the peak field B_{peak}, the following expression for the critical current density of the strongly-linked current path is obtained [79]:

$$J_{cs}(B,T) = \frac{F_{p\max}(T)}{B_{peak}(T)} \exp\left(1 - \frac{B}{B_{peak}(T)}\right).$$ (4.4)

The critical current density of Bi-2223 tapes (sample B-5) shows an exponential field dependence at high magnetic fields over a large temperature range, which results in a straight line in a semi-logarithmic plot (figure 4.5). The critical current density is obtained with the dc-magnetization method when the magnetic field is applied perpendicular to the wide side of the tape. The exponential field dependence finds its origin in classical flux creep (expression 4.4, solid lines), as will be discussed in section 4.3.1. A contribution of the weakly-linked network is observed at low magnetic fields, where the measured critical current density exceeds the critical current density of the strongly-linked backbone.
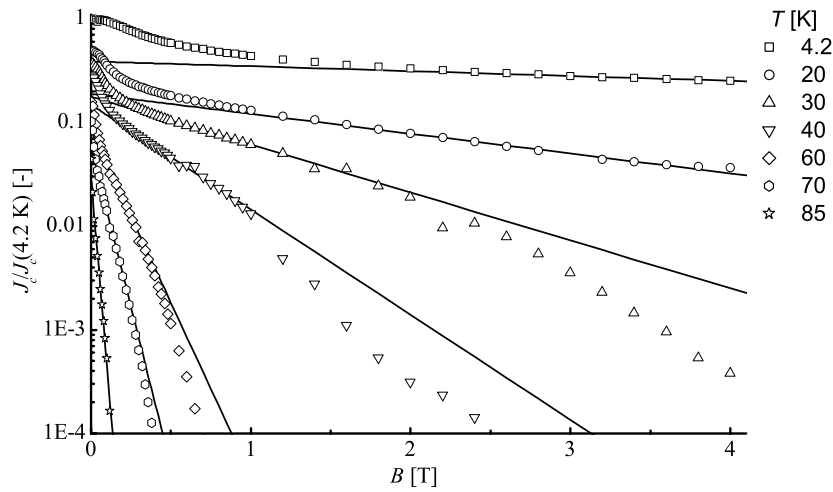
Figure 4.5. Normalized critical current density of sample B-5 as function of magnetic field at different temperatures, obtained with the dc-magnetization method. The critical current density is normalized to its self field value at 4.2 K. The magnetic field is applied perpendicular to the wide side of the tape. The lines represent the critical current density of the strongly-linked backbone (expression 4.4).

A small deviation between an exponential field dependence of J_{cs} and the overall critical current density is observed for low current at high magnetic field, which is due to an over-simplification of expression 4.4. The small deviation at high fields can be explained because the exponential field dependence (expression 4.4) is an approximation

of the critical current of the strongly-linked backbone according to classical flux creep, as will be discussed in section 4.3.1. Although the approximation influences the separation between the contributions of both current paths, it has a negligible effect on the results that are presented here.

The question to what extend the intra-granular pinning strength varies between tapes of various quality is addressed by analyzing the temperature dependence of B_{peak} for the samples listed in table 4.1. The temperature dependence of the peak field (figure 4.6) of the samples under investigation is obtained with the transport current method, which makes a direct comparison between the samples possible.
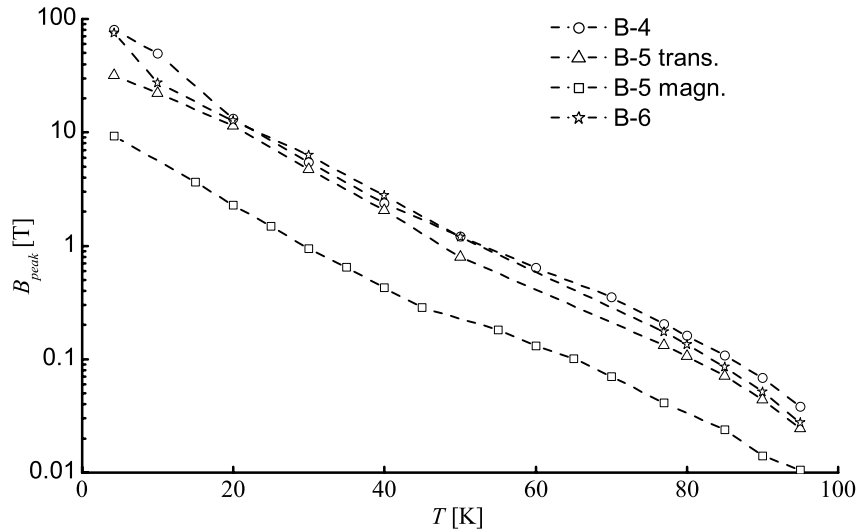
Figure 4.6. Magnetic field at which the maximum in macroscopic pinning force is reached (B_{peak}) for samples B-4, B-5 and B-6, as function of temperature. The magnetic field is applied perpendicular to the wide side of the tape. The critical current density of sample B-5 is obtained from transport- (B-5 trans.) and dc-magnetization methods (B-5 magn.). The dashed lines are a guide to the eye.

The values for B_{peak} of sample B-5 are obtained by both transport current and dc-magnetization methods in order to study the influence of the experimental technique on the results. Although sample B-5 has the highest critical current (table 4.1), its peak field is not the highest of the three samples. This again points out that B_{peak} only depends on the intra-granular pinning strength and not on the overall value of the critical current. Apparently the main difference between the tapes is the overall critical current density, which is related to the cross-section of both current paths.

A large difference between B_{peak} of sample B-5 is also observed when J_c is compared between the two experimental methods: transport- and dc-magnetization methods. The maximum in pinning force occurs at a magnetic field that is approximately 5 times higher when J_c is measured with a transport current. This difference can be

understood by for instance the difference in electric field at which both types of experiments are conducted, as is discussed in section 2.1.3.

4.2.2. Critical current density as function of field angle

In order to localize the current limiting mechanisms of both current paths in Bi-2223 tapes, the dependence on temperature and magnetic field angle of the critical current density is studied separately. Until now, modeling the angular dependence of the overall critical current over the entire temperature range was not successful. A possible explanation is that the current paths in Bi-2223 tapes have a different grain alignment, or that the current limiting mechanisms of one of the paths change due to a change in anisotropy in the grains. The differences in scaling of the contributions of both current paths are related to the grain structure of Bi-2223 tapes to determine the mechanisms that limit the critical current density.

The fact that the decrease in overall critical current density as function of applied magnetic field in thin films and single crystals is mainly determined by the field component parallel to the c-axis of the grains is a result of the layered structure of high-temperature superconductors. The large anisotropy in combination with a small coherence length in the c-direction results in a weak coupling between the CuO_2-planes over the temperature range where the spacing between the CuO_2-planes is larger than the coherence length in the c-direction [66,68,70,71,80,81]. The penetration depth for magnetic field applied parallel to the ab-plane (i.e. with shielding currents running in the c-direction) is comparable to the spacing between the CuO_2-planes in a large temperature range. Magnetic flux can penetrate between the CuO_2-planes without interfering with a transport current running along the ab-planes, therefore leaving the critical current density independent of magnetic field.

Since Bi-2223 tapes consist of a large number of plate-like grains which are aligned following a certain Gaussian-like distribution [65], a magnetic field applied parallel to the tape plane still results in a small component parallel to the c-axis of the grains [82]. This component is responsible for the degradation in J_c as function of magnetic field when applied parallel to the tape plane [7,21,73,83,84]. The critical current density of sample B-5 is measured using the dc-magnetization method for magnetic fields applied parallel and perpendicular to the tape surface. The critical current density is normalized to its value at 4.2 K and is shown as function of magnetic field in figure 4.7. A much stronger field dependence of J_c is observed when the magnetic field is applied perpendicular to the wide side of the tape. The magnetic field component parallel to the c-axis of the grains is almost equal to the applied field in this case. A much smaller component parallel to the c-axis exists for magnetic fields applied parallel to the wide side of the tape.
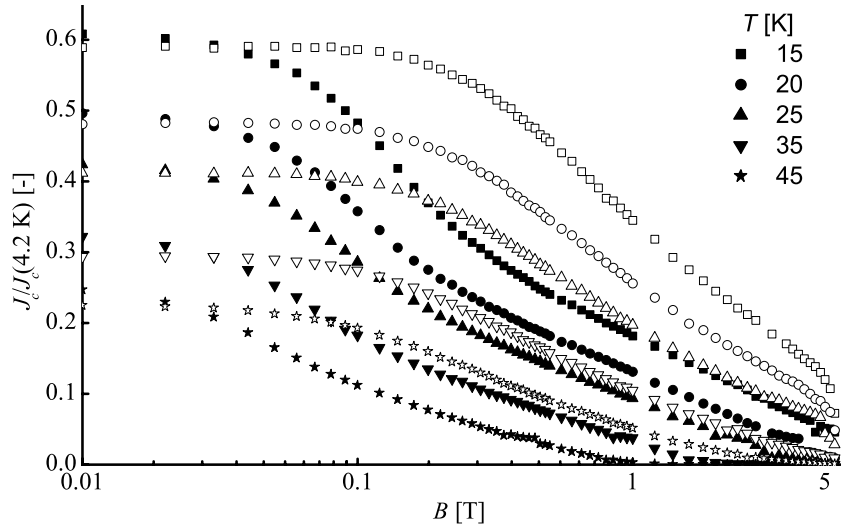
Figure 4.7. Normalized critical current density of sample B-5 as function of magnetic field applied parallel (open symbols) and perpendicular (closed symbols) to the wide side of the tape, at different temperatures. The critical current density is normalized to its value at 4.2 K.

The effective field component parallel to the *c*-axis of the grains in the tape can be used to describe $J_c(B)$ over the entire field range only within a limited temperature range [85,86]. The behavior of the critical current density of a Bi-2223 tape (sample B-5) in high magnetic fields can be scaled to the magnetic field component parallel to the *c*-axis of the grains (figure 4.8). The applied magnetic field is divided by the scaling factor b_{scs} in case the field is applied parallel to the wide side of the tape. The scaling field defines which fraction of the applied field is parallel to the *c*-axis of the grains. The scaling factor of the strongly-linked network (b_{scs}) is obtained directly from the macroscopic pinning force of the sample. It is equal to the peak field at which the maximum pinning force is reached for magnetic fields applied parallel to the wide side of the tape, divided by the peak field when the magnetic field is applied perpendicular to the wide side of the tape.

The critical current density at high magnetic field coincides for both field directions over a large temperature range. The behavior of the critical current density of the strongly-linked backbone is therefore completely determined by the magnetic field component parallel to the *c*-axis of the grains. The scaling field of the strongly-linked backbone does not apply to the weakly-linked network. A large deviation between the critical current density for both field directions is observed at low field. The deviation becomes smaller when the temperature increases. The scaling factor of the weakly-linked network is determined next.
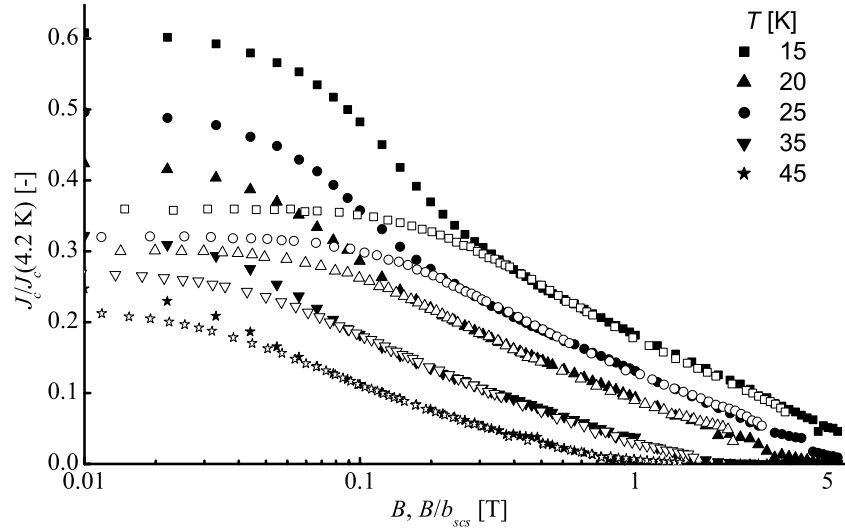
Figure 4.8. Normalized critical current density at different temperatures of sample B-5 as function of magnetic field applied parallel (open symbols) and perpendicular (closed symbols) to the wide side of the tape. The critical current density is normalized to its value at 4.2 K. The effective field component parallel to the c-axis of the grains is used to scale the critical current density for both field directions.

To analyze the dependence of the critical current density over the entire temperature range, both current paths are taken into account separately. First, the contributions of both current paths are separated by calculating the contribution of the strongly-linked backbone using the macroscopic pinning force (section 4.2.1). The weak-links critical current density is obtained by subtracting the strong-links critical current density from the overall critical current density. Additionally a second scaling factor (b_{scw}) is introduced that relates the dependence of the critical current density of the weakly-linked current path on magnetic field to the grain misalignment. The scaling factor b_{scw} for the weakly-linked network is related to the dependence of the critical current density on magnetic field in a similar way.

The critical current density of the weakly-linked network is obtained by subtracting the critical current density of the strongly-linked current path (expression 4.4) from the overall critical current density (figure 4.9). A clear difference in field dependence of the critical current density of the weakly-linked current path compared to that of the strongly-linked backbone is observed in sample B-5 for both field directions. The weakly-linked current density degrades at a higher applied field when the magnetic field is applied parallel to the tape surface compared to when the field is applied perpendicular to the tape surface.

The critical current density of the weakly-linked current path can be scaled for both field directions by dividing the value of the magnetic field, applied parallel to the wide side of the tape, by the scaling factor b_{scw}. The critical current density of the weakly-

linked current path then coincides for both field directions over a large magnetic field range (figure 4.10). An incomplete separation of the critical current of both current paths results in a deviation of the scaling at low temperatures, but has no significant influence on the scaling field b_{scw}.
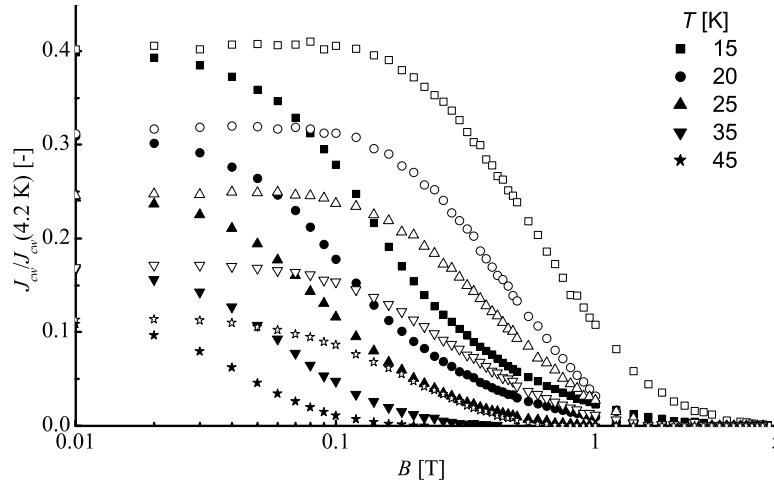
Figure 4.9. Critical current density at different temperatures of the weakly-linked network of sample B-5 as function of magnetic field applied parallel (open symbols) and perpendicular (closed symbols) to the wide side of the tape. The critical current density is normalized to its value at 4.2 K.
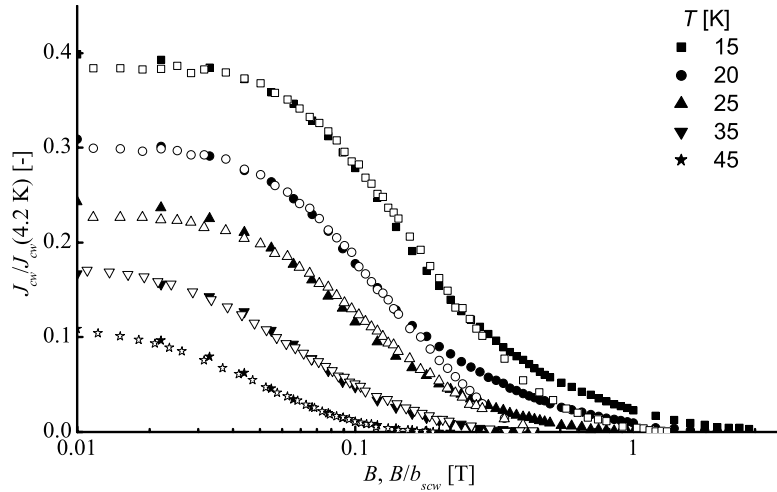
Figure 4.10. Weak-links critical current density at different temperatures of sample B-5, obtained using dc-magnetization for magnetic fields applied parallel (open symbols) and perpendicular (closed symbols) to the tape surface. The effective field component is obtained from the scaling factor b_{scs} in case the magnetic field is applied parallel to the wide side of the tape.

The question whether current flow in Bi-2223 tapes changes, or whether the mechanisms responsible for the dissipation change as function of temperature is addressed by analyzing the temperature dependence of both scaling factors (b_{scs} and b_{scw}). Since the grain connectivity of the current paths does not change as function of temperature, both scaling factors are expected to be independent of temperature.

The angular dependence of the critical current density of the current paths is analyzed in sample B-4 (transport method) and B-5 (magnetization method). A temperature dependent behavior of b_{scs} is observed in samples B-4 and B-5 below approximately 50 K (figure 4.11) while above this temperature it becomes temperature independent in case of the dc-magnetization method. The temperature variation in b_{scs} can not be explained by the grain misalignment. The critical current density of the strongly-linked backbone becomes almost independent of field angle (b_{scs}=1.1). Although this behavior at 4.2 K is not reported previously, it is a strong indication that at this temperature the magnetic field can not penetrate in between the CuO_2-planes in the grains that form strongly-linked current path. The penetration depth in the c-direction is small compared to the spacing between the CuO_2-planes, while they become comparable at around 50 K.
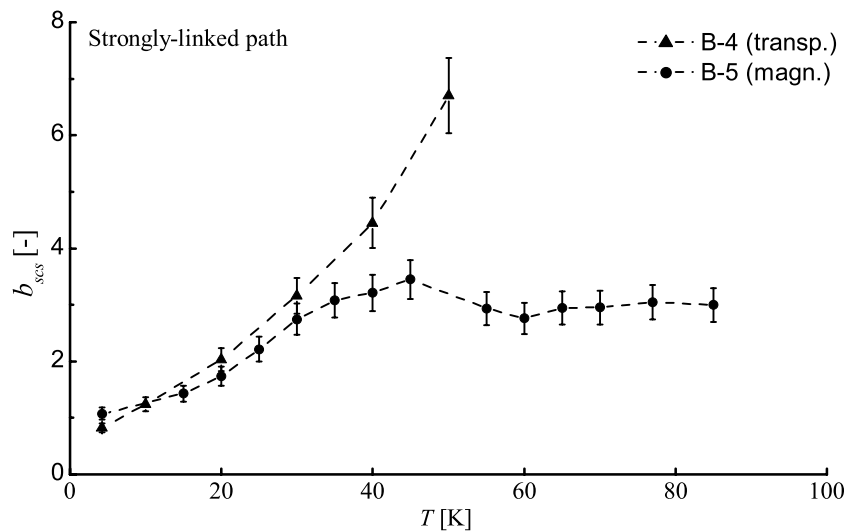
Figure 4.11. Scaling factor b_{scs} for the strongly-linked current path as function of temperature for samples B-4 (transport method) and B-5 (dc-magnetization method). The dashed lines are a guide to the eye.

The scaling factor b_{scw} is temperature independent (figure 4.12), which means that the mechanism responsible for the behavior of the weakly-linked current path and the current path itself does not change. A small difference in the magnetic field angle

dependence of both current paths is observed above 50 K. This results in a value for b_{scs} of approximately 3 ± 0.3 and for b_{scw} of approximately 3.8 ± 0.3 when the critical current density is obtained from dc-magnetization.
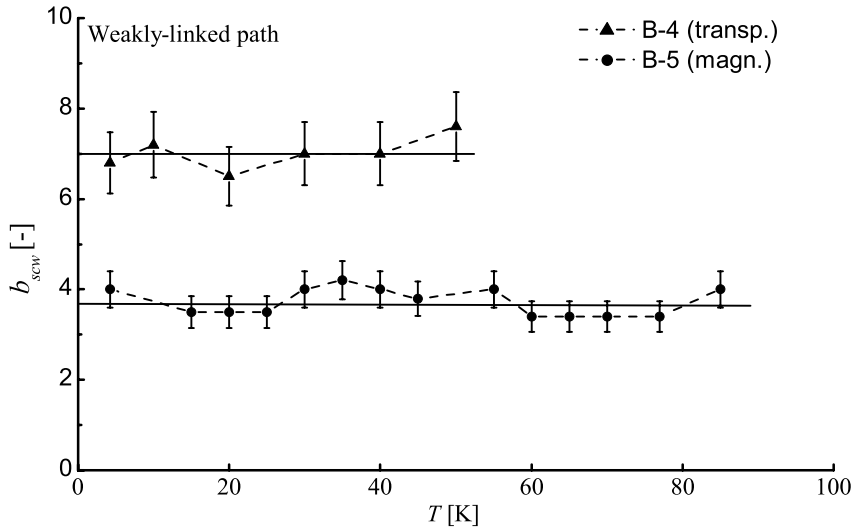
Figure 4.12. Scaling factor b_{scw} of the weakly-linked network as function of temperature for samples B-4 (transport method) and B-5 (dc-magnetization method). The dashed lines are a guide to the eye, while the solid line is a constant function of temperature.

Current transport in Bi-2223 tapes can be understood as running in two parallel paths, which is concluded from the accurate description of the angular dependence of the critical current density by the parallel path model. The critical current density of both paths shows a different dependence on magnetic field angle. Not only grain alignment of both current paths, but also the mechanisms that limit the current in the two paths are different, which results in a temperature dependent scaling field of the strongly-linked backbone below 60 K.

4.2.3. Aligned Bi-2223 powder

In this section it is verified whether a physical separation can be made between both types of current paths in Bi-2223 tapes. It is also investigated whether the assumption that dissipation in the strongly-linked backbone occurs within the grains and not at grain boundaries is correct. To reach both goals, the behavior of the critical current density of a Bi-2223 tape is compared with that of a weak-link-free powder extracted from the tape. Earlier studies showed that the low-field magnetization decreases when the

tape is ground into a powder, but no qualitative comparison between tape and powder was made [87,88,89,90]. Intra-granular flux pinning and therefore the critical current density of the strongly-linked backbone should remain unchanged after grinding as long as the c-axis alignment of the grains in the powder is comparable to that of the grains in the tape. It is verified whether the relative contributions of the weak-link and strong-link paths can be obtained from a comparison of the critical current density of both samples in the viewpoint of the parallel path model.
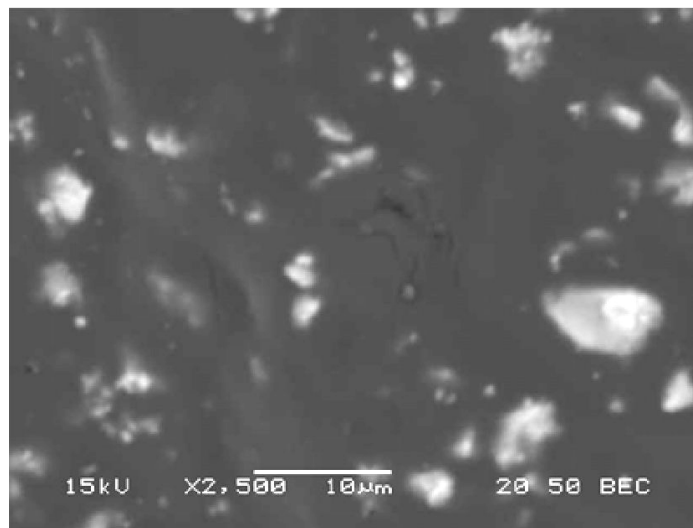
Figure 4.13. SEM-image of Bi-2223 grains that are extracted from sample B-5. The powder is filtered in order to obtain grains with a maximum size of 10 µm.

A single grained powder is extracted from a Bi-2223 tape (sample B-5) by sieving particles larger than 10 µm. Grain alignment is introduced by mixing the powder with diluted epoxy and pressing the resulting solution on a glass plate. After the epoxy is cured, a thin sample is obtained containing c-axis aligned Bi-2223 grains (figure 4.13).

The critical current density of the aligned powder is measured using the dc-magnetization method. The critical current density is measured as function of magnetic field at different temperatures, when the magnetic field is applied parallel to the c-axis of the grains (figure 4.14). There is no weakly-linked current path since the sample only contains single grains. The measured critical current density is the intra-granular critical current density of the powder. The critical current density of the aligned powder is described accurately above 55 K (expression 4.4). A deviation is observed at low magnetic field for temperatures below 65 K. Also a maximum in critical current density is observed in this temperature range. The deviation is not caused by remaining grain boundaries, but attributed to an over-simplification of the exponential field dependence, as is already mentioned in section 4.1.
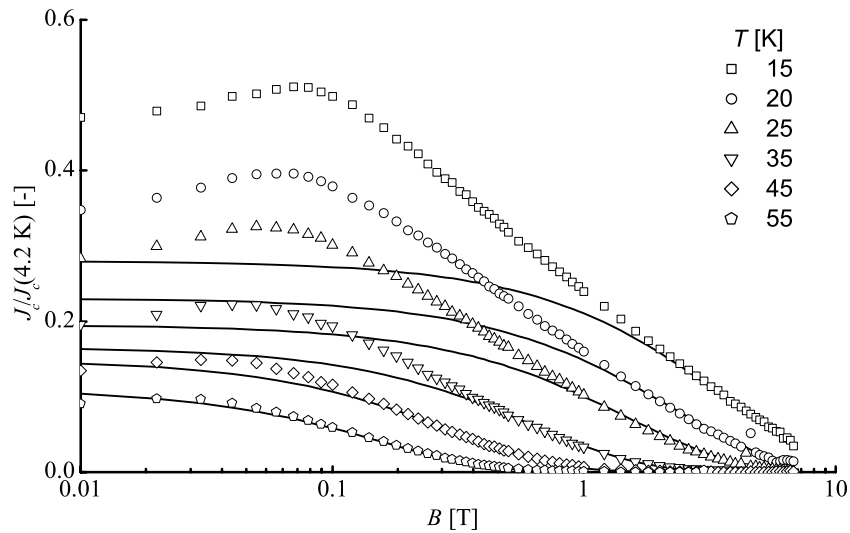
Figure 4.14. Normalized critical current density as function of magnetic field of the powder extracted from sample B-5 for different temperatures, obtained with the dc-magnetization method. The magnetic field is applied parallel to the *c*-axis of the grains. The solid lines represent the intra-granular critical current density (expression 4.4).
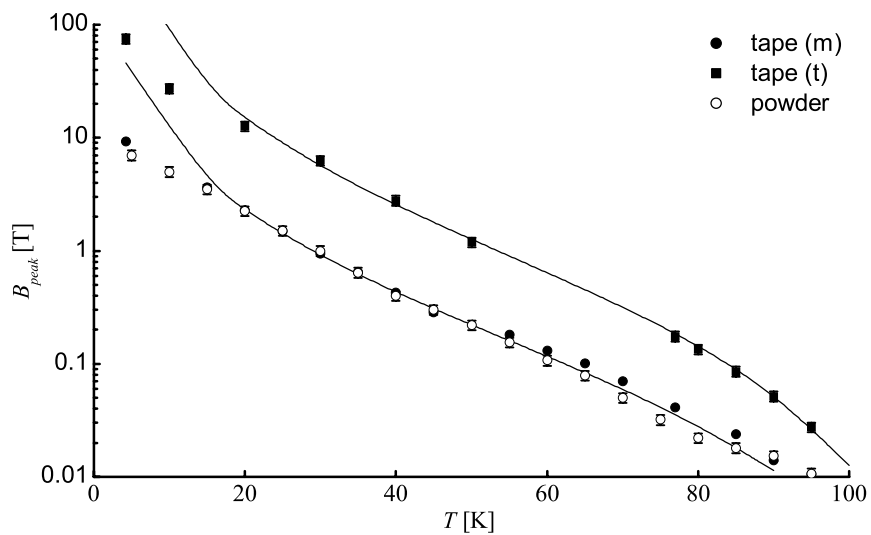
Figure 4.15. Temperature dependence of B_{peak} of intact sample B-5, measured with an uncertainty of 10 % using a transport current (t) and dc-magnetization (m), and determined from the dc-magnetization of the powder extracted from sample B-5. The lines represent a power-law fit according to expression 4.9.

A comparison between the critical current densities in the strongly-linked backbone in Bi-2223 tapes and the aligned powder is made by means of the macroscopic pinning force. To verify whether intra-granular flux depinning is indeed the current limiting mechanism in the strongly-linked backbone of the tape, the temperature dependence of the peak fields (B_{peak}) of tape and powder are compared (figure 4.15).

As expected, the intra-granular pinning properties are not changed by grinding the tape into a powder. The (magnetically measured) values of B_{peak} are identical for both samples and have the same temperature dependence as the B_{peak} that is obtained from transport measurements. A comparison between the critical current densities of tape and powder shows that both critical current densities are identical above a minimum magnetic field (figure 4.16). The difference in sample size between powder and tape is taken into account by normalizing the critical current density to its value at 4.2 K, at a magnetic field of 0.5 T where the contribution of the weakly-linked current path to the critical current density of the tape is zero. A good agreement between the critical current density of tape and powder is observed at intermediate and high magnetic field. The critical current density of the powder at low magnetic field is indeed lower than that of the tape, due to the absence of a weakly-linked network.
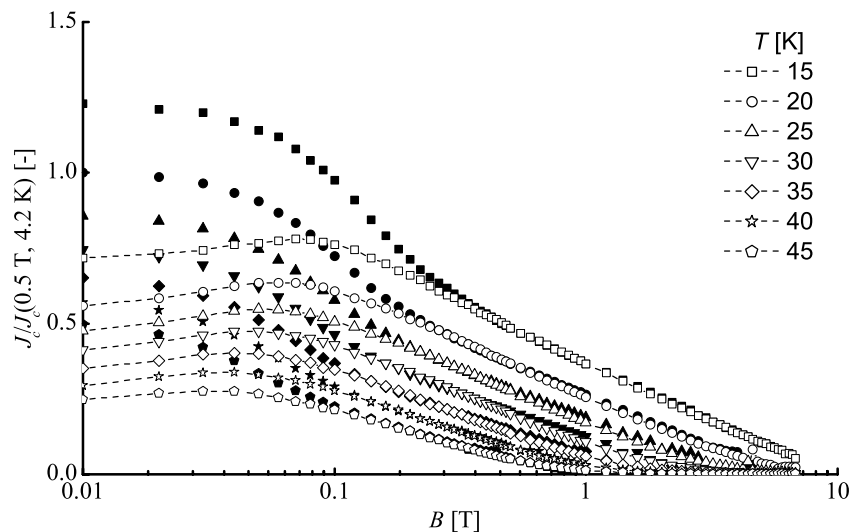
Figure 4.16. Critical current density as function of magnetic field at various temperatures for sample B-5 (closed symbols) and the powder extracted from the tape (open symbols). The critical current density is normalized to its value at 4.2 K and 0.5 T. The dashed lines are a guide to the eye.

Based on the comparable values of the peak field and the similar magnetic field dependence of the critical current density of both Bi-2223 tape and aligned powder, it is concluded that dissipation of the strongly-linked backbone in Bi-2223 tapes is indeed caused by flux depinning inside the grains.

The coupling between both current paths in the tape can be verified by analyzing the temperature dependence of the contribution of both current paths. The contribution of the weakly-linked current path in Bi-2223 tapes can be separated from to the overall critical current density, by subtracting the scaled critical current density of the powder. The maximum of the contribution of the weakly-linked network to the overall critical current density is plotted as percentage of the overall current density (figure 4.17).
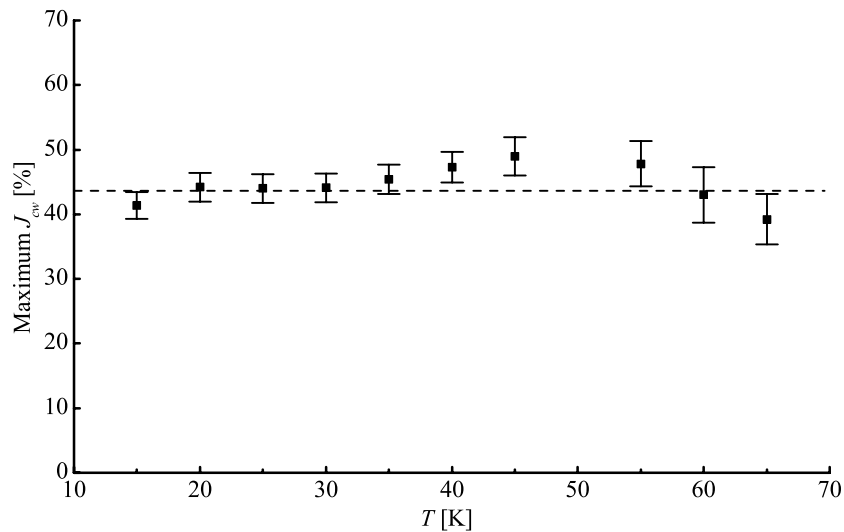
Figure 4.17. Maximum critical current density of the weakly-linked network of tape B-5 as function of temperature, expressed as percentage of the overall critical current density. The dashed line is the average of 44 %.

A constant contribution of the weakly-linked network to the overall critical current density of the tape is observed when tape and powder magnetization are compared. The temperature independence of the weak-links contribution indicates that the temperature dependence of the critical current density of the weakly-linked network is the same as that of the strongly-linked backbone (within the measurement error). From these data it is concluded that although different mechanisms limit the current in both current paths in Bi-2223 tapes, they are strongly coupled.

4.2.4. Conclusions on current flow in Bi-2223

The critical current as function of temperature, magnetic field and field angle is described accurately over the entire temperature and magnetic field range when both current paths are taken into account separately. Both contributions can be isolated from

the overall critical current by applying the parallel path model. The behavior of the critical current density of the weakly-linked network and the strongly-linked backbone is described by calculating the component of the magnetic field parallel to the c-axis of the grains in both current paths. Based on this observation it is concluded that the parallel path model introduced here convincingly applies to current transfer in Bi-2223 tapes.

A separation between the contributions of both current paths in Bi-2223 tapes is made by comparing the critical current density of a tape with that of aligned powder extracted from the tape. The behavior of the critical current density at high field of both samples is identical. It is therefore concluded that intra-granular flux motion limits the current in the strongly-linked backbone.

The temperature dependence of the critical current density is comparable for both current paths in Bi-2223 tapes. This suggests that although the dissipation in the weakly-linked network occurs at grain boundaries, while in the strongly-linked backbone it occurs in the grains, both mechanisms are somehow related.

4.3. Identifying the dissipation mechanisms in Bi-2223

In the previous section, it is demonstrated how the contributions of both current paths in Bi-2223 tapes can be obtained by comparing the critical current density of the tape with that of aligned powder extracted from the tape. In this section, the mechanisms responsible for the behavior of the critical current density of both current paths are studied more closely. It is investigated in subsections 4.3.1 and 4.3.2 in how far classical flux creep theory is able to describe intra-granular flux motion observed in Bi-2223 tapes and aligned powder. Whether dissipation in the weakly-linked network occurs at low- or at high-angle grain boundaries is investigated as well. Two theories are briefly outlined in subsections 4.3.3, one describing dissipation at high-angle grain boundaries in a network of Josephson weak links, the other as inter-granular flux motion at low-angle grain boundaries. Whether the theories apply to the weakly-linked network in Bi-2223 tapes is investigated in subsection 4.3.4 by analyzing the magnetic field dependence of the critical current density of the weakly-linked current path in Bi-2223 tapes.

4.3.1. Classical flux creep theory in HTS

The exponential field dependence of the critical current density in Bi-2223 tapes at high fields as described in section 4.2.1 is a simplified form of the dependence described according to classical flux creep theory [91]. The original expression for the critical current density of the strongly-linked current path is introduced, since rather large deviations between the measured critical current density and the simplified model occur.

It is assumed that this theory, which finds its origin in low-temperature superconductors, also applies to intra-granular flux motion in Bi-2223 tapes.

Flux lines in classical type-II superconductors are pinned by defects and will be unpinned when the Lorenz force acting on the flux lines overcomes the pinning force. According to Anderson [92], the electric field generated across a superconductor is given by:

$$E(B,T,J) = E_0(B,T) \exp\left(\frac{-U(B,T,J)}{kT}\right) \text{ and}$$

$$E_0(B,T) = \nu(T) LB, \tag{4.5}$$

where $U(B,T,J)$ is the pinning potential, which has to be overcome in order to unpin the flux lines, ν the attempt frequency and L the hopping distance. The expression is based on a homogeneous superconductor in which the material does not show a variation in microstructure and pinning. Anderson and Kim used a linear $U(J)$-dependence; $U=U_0(1-J/J_{c0})$ for the pinning potential, where J_{c0} is the current density at which the barrier vanishes. Beasley [93] was the first to use a non-linear barrier for a current density close to J_{c0}.

The form for $U(B,T,J)$ in Bi-2223 tapes can be extracted from magnetic relaxation experiments [94]. Zeldov [95,96] used a logarithmic dependence of the pinning potential on current (expression 4.6), which was later confirmed by flux creep experiments done by Maley [97]. They were able to measure the dependence for a large range of current densities by measuring flux creep as function of time at different temperatures. The logarithmic behavior of the pinning potential is given by:

$$U(B,T,J) = U_0(B,T) \ln\left(\frac{J_{cs}(0,T)}{J}\right). \tag{4.6}$$

The pinning potential vanishes when the current density becomes equal to $J_{cs}(0,T)$, which is the critical current density of the strongly-linked backbone at zero magnetic field. The magnetic field and temperature dependence of U_0 has the following form [98]:

$$U_0(B,T) = kT \left(\frac{B_{irr}(T)}{B}\right)^{n_s}, \tag{4.7}$$

and $\rho \propto \exp\left(\dfrac{-U_0}{kT}\right).$ \hfill (4.8)

The Arrhenius law described by expression 4.8 was first used by Palstra to describe the flux flow resistivity in Bi-2212 [99]. The temperature dependence of the irreversibility field $B_{irr}(T)$ is calculated by Yamasaki [100], by assuming that the irreversibility field is reached when the term U_0/kT in expression 4.8 takes a specific value, corresponding to the electric field criterion E_c. The temperature dependence of the irreversibility field is thus obtained from the pinning potential and flux flow resistivity:

$$B_{irr}(T) = B_{irr0}\left(\frac{T_c}{T} - 1\right)^{\frac{1}{n}},$$ \hfill (4.9)

where T_c is the critical temperature of the material. This expression is similar to the one obtained by Schilling [101], who stated that the irreversibility field shows an exponential temperature dependence below 0.6 times the critical temperature of the superconductor. The crossover between the two regions reflects the three- and quasi-two-dimensional character of the vortex lattice in a layered superconductor. Inserting expressions 4.6 and 4.7 into expression 4.5, while setting $E=E_c$ at $J=J_{cs}$, gives the magnetic field and temperature dependence of the critical current density for the strongly-linked current path:

$$J_{cs}(B,T) = J_{cs}(0,T) \exp\left(-\left(\frac{B}{B_{scs}(T)}\right)^{n_s} \ln\left(\frac{E_0(B,T)}{E_c}\right)\right).$$ \hfill (4.10)

The relation between electric field and current density in the strongly-linked current path is given by:

$$E(J,B,T) = E_0(B,T) \left(\frac{J}{J_c}\right)^{\left(\frac{B_{scs}}{B}\right)^{n_s}}.$$ \hfill (4.11)

The irreversibility field in expression 4.7 is replaced by a more general scaling parameter $B_{scs}(T)$, since expression 4.10 is also applied to describe the critical current density of the weakly-linked network in Bi-2223 tapes in section 4.3.4. The irreversibility field is defined as the magnetic field where the irreversible magnetization vanishes and therefore does not apply to the weakly-linked network in tapes.

The collective creep theory by Feigel'man [102] takes the interaction between neighboring flux lines into account by using an inverse power law dependence of the activation energy on current. Different pinning regimes that depend on the vortex interaction are represented by different values for the power in the $U(J)$-dependence. The value of the power is ranging from 1/7 for the motion of individual flux lines at low magnetic field and low temperature, to 3/2 for small flux bundles at intermediate magnetic field and 7/9 for large flux bundles in high magnetic field [103].

Although the pinning potential used to derive expression 4.10 differs from that of the collective pinning theory, the interaction between the flux lines is included in the parameter $E_0(B,T)$ of expression 4.5. The distance between the flux lines decreases with increasing magnetic field. The interaction also depends on the temperature-dependent diameter of the flux lines.

4.3.2. Intra-granular flux pinning in Bi-2223 tapes and powder

It is suggested in section 4.2 that dissipation in the strongly-linked backbone of Bi-2223 tapes occurs due to intra-granular flux motion. In order to verify whether the dissipation in the strongly-linked backbone can be described according to classical flux creep, the magnetic field dependence of the critical current density of aligned Bi-2223 powder is modeled over a wide magnetic field and temperature range. When dissipation in the strongly-linked backbone can be described with classical flux creep, this theory should also describe the current-voltage characteristic around the superconducting transition of a Bi-2223 tape. Whether this is the case is verified in the magnetic field range where the weakly-linked network no longer contributes to the overall critical current density.

Intra-granular flux motion in aligned Bi-2223 powder can be described accurately by classical flux creep, which follows from the good agreement between theory (expression 4.10) and the observed magnetic field dependence of the critical current density (figure 4.18). The values that the parameters of expression 4.10 take are listed in table 5.3. A constant value of 0.01 m/s is taken for the attempt frequency v times hopping distance L of the depinned flux lines. It is evident that classical flux creep is able to describe the dissipation in the strongly-linked backbone over a much wider magnetic field range than its simplified form (expression 4.4). A good agreement between model and measured critical current density is reached above 0.2 T at 20 K (figure 4.18), while the simplified expression only describes the measurement well for magnetic fields above 1 T (figure 4.5).

A deviation between model and experiment is observed at low magnetic fields and is caused by two factors. First, the sample demagnetization decreases the critical current density at low magnetic field within the entire temperature range. Secondly, the observed maximum in critical current density at low temperatures could be the result of

the dimensional crossover when the CuO_2-layers become coupled that is also observed in the dependence of the critical current density on magnetic field angle (section 4.2.2). Classical flux creep theory does not take such a crossover into account. The deviation becomes small for temperatures above 50 K.
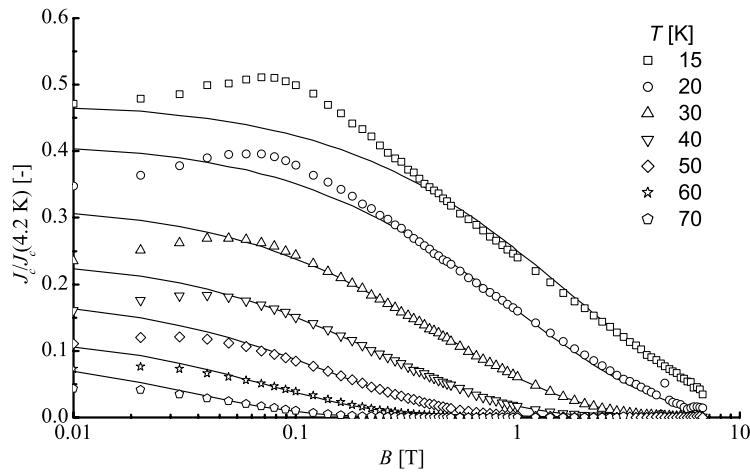
Figure 4.18. Critical current density obtained from dc-magnetization as function of magnetic field of the aligned powder extracted from sample B-5. The critical current is normalized to its value at 4.2 K. The magnetic field is applied parallel to the c-axis of the grains. The lines represent the critical current density according to classical flux creep theory (expression 4.10).
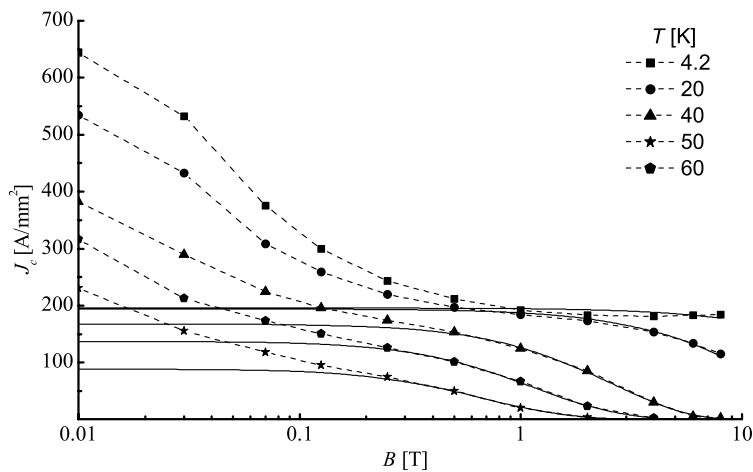
Figure 4.19. Critical current density, obtained using the transport current method, as function of applied magnetic field of sample B-4. The magnetic field is applied perpendicular to the wide side of the tape. The solid lines represent the critical current density of the strongly-linked backbone according to classical flux creep theory (expression 4.10). The dashed lines are a guide to the eye.

The critical current density of the strongly-linked backbone of Bi-2223 tapes can also be described by classical flux creep theory when the critical current is measured with the transport method (figure 4.19). The theory (expression 4.10) applies in the magnetic field region where the weakly-linked network is no longer contributing to the overall critical current (parameters listed in table 5.3), which is above 1 T at 4.2 K. The weakly-linked network carries a significant part of the transport current at low field.

The hypothesis that classical flux creep is responsible for the dissipation in the strongly-linked backbone is supported by the voltage characteristics around the superconducting transition of the tape (figure 4.20). The electric field across the superconductor is described well by the power-law dependence (expression 4.11) around the electric field criterion of 10^{-4} V/m in the field range where the weakly-linked network does no longer contribute to the overall critical current density. The dashed horizontal line in the figure is the voltage criterion of 10^{-4} V/m, at which the critical current density is defined. A minor deviation is observed at higher electric fields. This confirms that the behavior of the critical current density of the strongly-linked backbone is due to flux motion in the sense of classical flux creep.
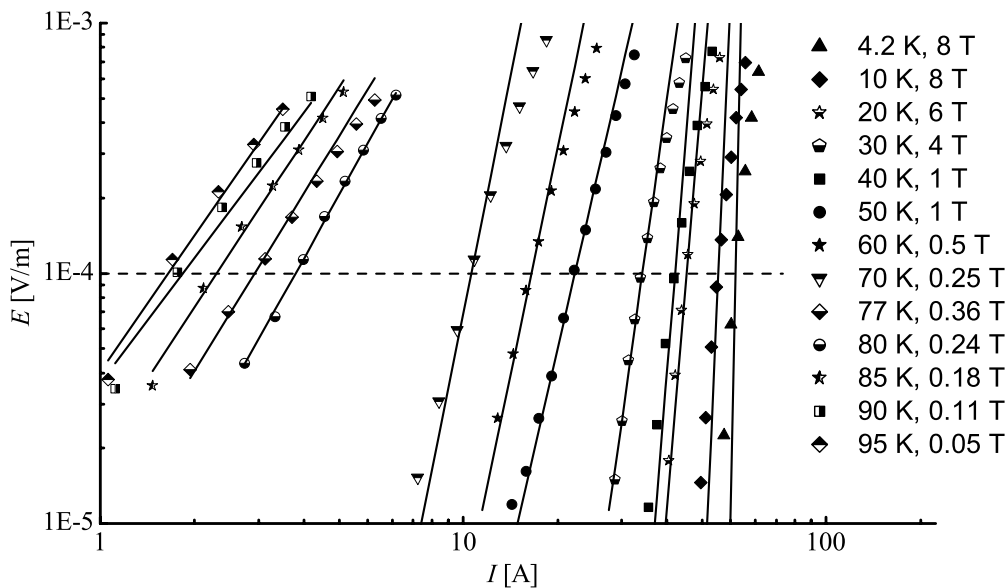
Figure 4.20. $E(I)$-characteristics at high field of sample B-4 at different temperatures. The solid lines represent the $E(I)$-characteristics according to classical flux creep (expression 4.11). The dashed line is the voltage criterion at which the critical current is defined.

4.3.3. Dissipation in the weakly-linked network

A review of experiments and results is presented, which have led to the general assumption that the weak-link contribution to the overall critical current density in Bi-2223 tapes is related to Josephson-type behavior in the inhomogeneous matrix of high-angle grain boundaries. However, recent developments have led some authors to advance an alternative picture, based on the interaction between inter-granular flux lines and the intra-granular flux line lattice.

Grain boundaries that are formed in the microstructure of various high-temperature superconductors can suppress a supercurrent. Studies on YBCO crystals show that, strain fields that are due to a lattice mismatch form at the boundary where two grains meet [104,105]. The strain fields reduce the critical current density at the grain boundary. They increase in size when the grain boundary angle is increased, which results in an exponential dependence of the critical current density as function of boundary angle [106,107]. The strain fields overlap above a certain grain boundary angle and the grain boundary becomes weakly-linked in the sense of Josephson behavior [33,41].

A similar behavior as observed at boundaries in YBCO is seen in Bi-2212 bi-crystals [44]. Josephson behavior is seen at [001] tilt boundaries above a minimum angle [43], together with a lower critical temperature at the grain boundary [108]. Although a large variety of grain boundaries is observed in Bi-2223 tapes, the difficulty of producing high-quality Bi-2223 crystals and films for detailed studies so far has caused a lack of knowledge on grain boundary properties in this system. In Bi-2223 tapes, a variety of low-angle and high-angle colony boundaries is observed (SCTILT, ECTILT and OABTWIST as shown in figure 3.2). As mentioned before, the lattice mismatch between colonies of well-aligned grains gives rise to strain fields, but also induce the formation of secondary phases and amorphous layers. Bi-2212 lamellae at SCTILT boundaries in Bi-2223 tapes and other secondary phases in Bi-2212 tapes are reported [109,110,111]. The cross-section of high-angle SCTILT boundaries in Bi-2223 tapes is largely formed by the Bi-2212 phase, and only a small fraction of the boundary is formed by the Bi-2223 phase [112]. The formation of Bi-2212 layers at OABTWIST boundaries in Bi-2223 tapes is observed and has a large effect on current running along the c-axis of the grains [113,114]. Recently it is shown that [001] tilt boundaries cause a Josephson behavior when the boundary angle exceeds 8 degrees [115,116,117], but also secondary phases give rise to weak coupling between the colonies [118].

The scenario where grains and high-angle grain boundaries form a network of Josephson weak links in Bi-2223 tapes is widely accepted and was introduced to describe the hysteresis in critical current density as function of applied field [119,120,121]. The shielding field that is generated within the grains of a Bi-2223 tape causes an increase of the local field at the grain boundaries with increasing applied field. The opposite occurs

when the external magnetic field is decreased, and the local field at the grain boundaries is lower than the applied field. This scenario results in different values for the critical current density of the tape in increasing and decreasing magnetic fields.

In order to describe the $J_c(B)$ dependence of such a network of Josephson weak links at high-angle boundaries, the properties of a single Josephson junction are briefly outlined. The magnetic field dependence of the critical current density of a Josephson weak link is given by:

$$J_c(B) = J_c(0) \left| \frac{\sin\left(\dfrac{\pi B(2\lambda_l + d)w}{\phi_0}\right)}{\left(\dfrac{\pi B(2\lambda_l + d)w}{\phi_0}\right)} \right|.$$

(4.12)

Here λ_l is the London penetration depth, d the barrier thickness, w the width of the weak link and ϕ_0 the elementary flux quantum. The magnetic field dependence is represented by a Fraunhofer-like pattern (see figure 4.21), where the minima occur whenever the flux in the weak link equals an integer amount of flux quanta.
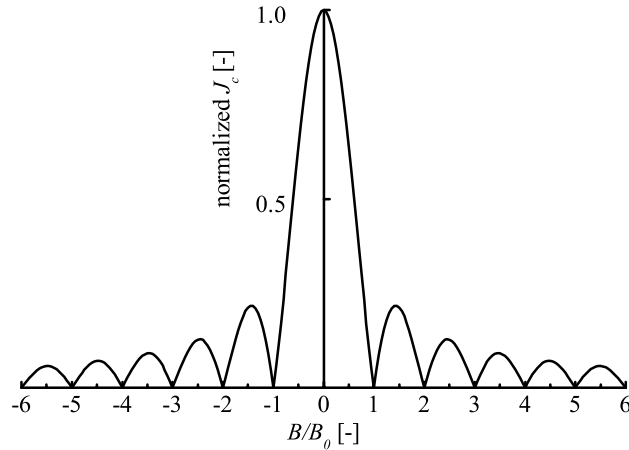
Figure 4.21. Normalized critical current density as function magnetic field scaled to ϕ_0 of a Josephson weak link. The critical current density is normalized to its value at zero field.

A Fraunhofer-like pattern was first used by Kwak to describe the magnetic field dependence of the critical current density of weakly-linked grains in YBCO [6]. Since a high amount of weak links with different dimensional properties is present in the samples, a distribution function of Fraunhofer patterns was used by Peterson [122]. A Fraunhofer

pattern only applies when the magnetic field is oriented parallel to one side of the rectangular junction. This is not the case when the grains are randomly oriented in the sample, in which case the use of an Airy diffraction pattern derived for elliptical junctions is more appropriate to describe the field dependence of the critical current density [123].

Several approaches were made to describe the critical current density of Bi-2223 tapes as a network of weakly-linked grains [124,125,126]. Other approaches included modeling of the current in the c-direction in grains with decoupled CuO_2-planes [65,127] and a network of pinned Josephson vortices at grain boundaries [128]. Müller [129,130] used a different approach to calculate the magnetic field dependence of the critical current density of the weakly-linked network in Bi-2223 tapes. Instead of using a Fraunhofer pattern, a model based on inter-granular pinning was developed. Josephson vortices are pinned at the corners in a two-dimensional array of rectangular grains [131]. The expression for $J_{cw}(B,T)$ used by Müller describes a similar field dependence as an overall Fraunhofer pattern with a distribution of junction parameters:

$$J_{cw}(B,T) = \frac{J_{cw}(0,T)}{1 + \left(\dfrac{|B|}{B_0(T)}\right)^{\beta}} \quad , \tag{4.13}$$

where B_0 is the characteristic field of the weak links. The parameter β reflects the geometry of the weak links [123]. When the weak links are circular, β has a value of 3/2, and the magnetic field dependence is the same as in the case of an Airy diffraction pattern. In case of rectangular junctions, one obtains $\beta=1$ when the field which penetrates the weak links is within a few degrees of being parallel to one of the junction edges. For different field orientations, $\beta=2$. The temperature dependence of the parameters in expression 4.13 is related to the character of the weak links in the tape [132,133].

The critical current of low-angle grain boundaries shows a different behavior as function of magnetic field than of high-angle grain boundaries. Although a decrease in J_c is observed in grain boundaries that are formed at angles smaller than 10-15 degrees, no Josephson effect is present. The strain fields at low-angle boundaries are not extended over the entire length of the boundary. Superconducting bridges remain between the strain fields, where current can cross from one grain to the next [134]. Abrikosov vortices with highly anisotropic Josephson cores (*AJ*-vortices) are pinned at defects within the boundary. The inter-granular pinning at boundary defects is not the only mechanism that keeps the inter-granular vortices in place [135,136,137]. A strong interaction between the inter-granular *AJ*-vortices and the intra-granular Abrikosov vortices exists. The depinning of *AJ*-vortices at low-angle boundaries forms the main dissipation mechanism at fields that are high enough to penetrate the grains and depends largely on intra-granular pinning. This is confirmed in YBCO by several experimental studies [138,139,140,141,142]. In case the dissipation of the weakly-linked network occurs at low-angle grain boundaries,

the magnetic field and temperature dependence of the weak-links critical current density should be closely related to that of the strongly-linked backbone. This is exactly what is observed comparing the temperature dependence of the critical current density in tapes and in isolated powder, as discussed in section 4.2.3.

Although it is widely accepted that Josephson weak links in Bi-2223 tapes are responsible for the behavior of the critical current at low magnetic field, several questions remain unanswered. Since Josephson junctions are strongly field sensitive, the large current densities of the weakly-linked network that are measured at relatively high magnetic field can not be explained [143,144,145]. Low-angle grain boundaries will contribute largely to the overall critical current density of Bi-2223 tapes. Because the critical current density of the low-angle boundaries is orders of magnitude higher than that of high-angle grain boundaries, especially in field, the contribution of low-angle grain boundaries to the overall critical current density will probably dominate over the contribution of high-angle boundaries.

4.3.4. Inter-granular flux pinning

The question is addressed whether the dissipation in the weakly-linked network in Bi-2223 tapes occurs at high-angle grain boundaries that form a network of Josephson weak links or due to inter-granular flux motion at low-angle grain boundaries. The theories that are introduced in the previous subsection are applied to describe the magnetic field dependence of the critical current density of the weakly-linked network.

A power-law dependence (expression 4.13) of the critical current density on magnetic field is the result of dissipation at Josephson weak links that are located at high-angle grain boundaries. To verify whether this behavior occurs in the weakly-linked network of Bi-2223 tapes, the critical current density at low field that is applied perpendicular to the wide side of the tape is described according to this model (figure 4.22).

The critical current density of the weakly-linked network is separated from the overall critical current density of the tape by subtracting the critical current density of the aligned powder from the tape. The result shows that the critical current density of the weakly-linked network can not be described by a power-law, even when the value of parameter β is taken equal to 2. Parameter β in expression 4.13 should be increased to an even higher value to minimize the deviation. However, as discussed in the previous section, such a high value of β can not be correlated to a physical mechanism.

Although a deviation occurs when the critical current density of the weakly-linked network is described according to a network of Josephson weak links, the deviation does not occur when the critical current is described according to classical flux creep (expression 4.10). The model that describes intra-granular flux motion also applies to

inter-granular flux motion at low-angle grain boundaries. A strong coupling between inter-granular flux lines at low-angle grain boundaries and intra-granular flux lines explains the comparable behavior [135]. These findings are also confirmed by the quite similar temperature dependence of the critical current density of both current paths in the tape (section 4.2.3).
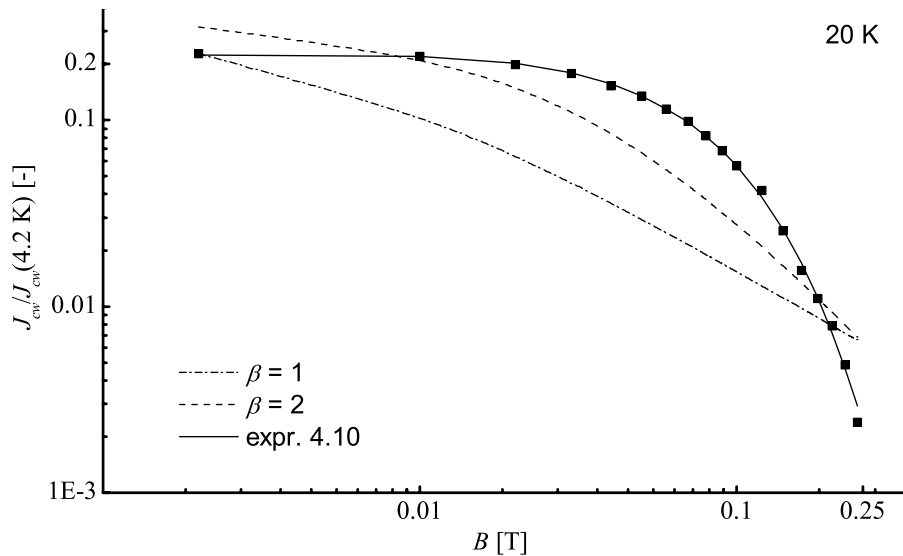
Figure 4.22. Normalized critical current density of the weakly-linked network of sample B-5 at 20 K, obtained with the dc-magnetization method. The critical current density is obtained by subtracting the critical current density of the aligned powder from that of the tape where the powder was extracted from. The critical current density is described according to a network of Josephson weak links (expression 4.13) with $\beta=1$ and $\beta=2$, and according to classical flux creep theory (expression 4.10).

The good agreement between the behavior of the weakly-linked network and classical flux creep theory is also expressed when this theory is applied to describe the critical current density of the weakly-linked network over a large magnetic field and temperature range (figure 4.23). A very good agreement between model and measured critical current density is observed, even at low magnetic field. The parameters of expression 4.10 are listed in table 5.3. The same value for the product of attempt frequency and hopping distance (vL) of 0.01 m/s as for the strongly-linked backbone applies. Based on the conclusion that both mechanisms which limit the critical current density in Bi-2223 tapes are based on flux pinning, the overall critical current density that is obtained with the transport method can also be described with classical flux creep (figure 4.24). The critical current of sample B-4 is measured as function of magnetic field for different temperatures. The magnetic field is applied perpendicular to the wide side of the tape.
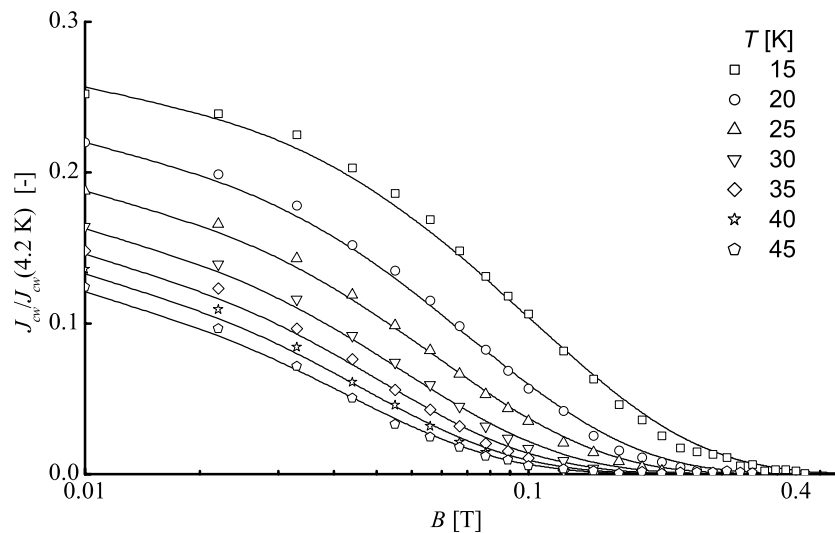
Figure 4.23. Critical current density of the weakly-linked network in sample B-5 as function of magnetic field at different temperatures. The critical current density is normalized to its value at 4.2 K and is obtained by subtracting the critical current density of the aligned powder from that of the tape. The magnetic field is applied perpendicular to the wide side of the tape. The solid lines represent the critical current density according to classical flux creep theory (expression 4.10).
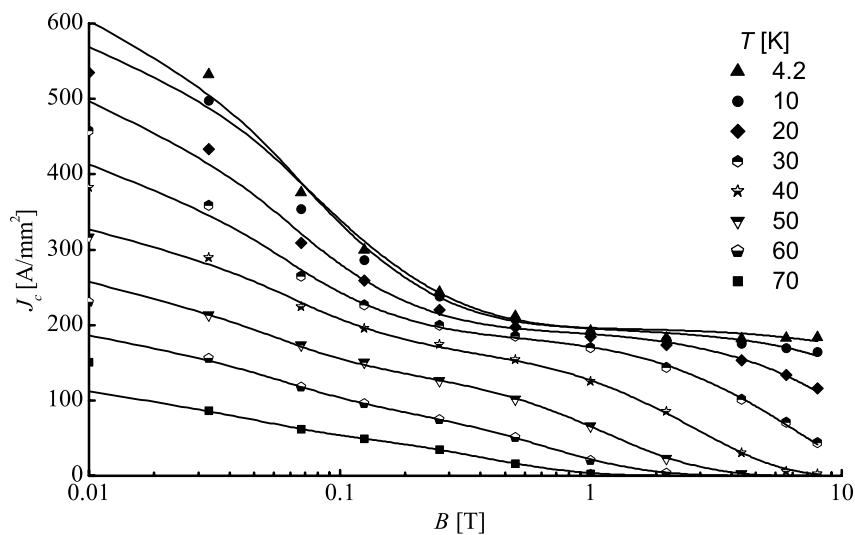
Figure 4.24. Critical current density of sample B-4 versus magnetic field at low temperatures, measured with the transport method. The magnetic field is applied perpendicular to the wide side of the tape. The solid lines represent the critical current density according to classical flux creep (expression 4.10).

The overall critical current density is represented by solid lines (parameters in table 5.3) when the behavior of both current paths is described according to classical flux creep. The model describes the $J_c(B,T)$ over the entire double step regime very well, except for low magnetic fields at low temperatures where the self-field of the tape is comparable to the applied magnetic field.

4.4. Conclusions

The first main conclusion that can be drawn based on the results presented in this chapter is that current in Bi-2223 tapes can be described as running in two paths in parallel. The critical current density of both paths is limited by separate mechanisms. This main conclusion is based on a number of observations:

- The angular dependence of the critical current density can only be scaled as function of the magnetic field component parallel to the c-axis of the grains when the contribution of both current paths are taken into account separately.
- Different scaling factors apply for the strongly-linked backbone and the weakly-linked network.
- The weakly-linked network and the mechanism that limits the critical current density of this current path do not change as function of temperature, which is expressed by a temperature-independent scaling factor.
- The temperature dependent scaling field of the strongly-linked current path shows that the mechanism that limits the critical current density of the strongly-linked backbone changes below 50 K. This can be explained by a change in coupling between the CuO_2-planes of the grains.
- Both current paths can be separated physically by grinding the tape into a powder.
- The grain alignment of the powder is sufficiently high to make a direct comparison between the critical current density of powder and tape possible.
- The weakly-linked network is formed by grain boundaries. The decrease in critical current density of the powder at low field is less compared to that of the tape.
- The dissipation of the strongly-linked backbone occurs within the grains. No change in the behavior of the critical current density at high magnetic field is observed when the tape is ground into a powder.

The second main conclusion is that the mechanisms that limit the critical current density in Bi-2223 tapes can be clarified after the contributions of both current paths have been isolated from the overall critical current density:

- Intra-granular flux motion according to classical flux creep limits the critical current density of the strongly-linked backbone. The magnetic field and temperature dependence of the critical current density can be described accurately by this theory, as is the voltage-current characteristic around the superconducting transition of the tape.
- The critical current density of the weakly-linked network is not limited by Josephson behavior at high-angle grain boundaries.
- The weakly-linked network is formed by low-angle grain boundaries where dissipation can be attributed to inter-granular flux motion.
- A coupling between inter- and intra-granular flux pinning in Bi-2223 tapes is expected. This is supported by the fact that the behavior of the critical current density of the weakly-linked network can be described accurately according to classical flux creep and a similar temperature dependence of the critical current density of both current paths is observed.

The magnetic field angle dependence of the critical current density of the strongly-linked backbone in Bi-2223 tapes has a large effect on the design of high-field applications at 4.2-40 K, such as high-field insert magnets. The assumption that the critical current density at high field only depends on the effective magnetic field component parallel to the c-axis of the grains does not apply in the sample investigated in this study. The change in coupling between the CuO_2-planes of the grains in the strongly-linked backbone should be investigated more extensively. Detailed measurements of the dependence of the critical current density on magnetic field and field angle should be performed in high magetic field.

5. Flux pinning in polycrystalline high-temperature superconductors

The hypothesis that inter-granular flux pinning at low-angle grain boundaries in Bi-2223 tapes is coupled to intra-granular flux pinning is investigated in more detail. The coupling is verified by comparing the effect of a reversible change in intra-granular pinning on the behavior of the critical current density of the weakly-link network and the strongly-linked backbone. The question whether an improvement of the production process only results in a larger effective cross-section of the current paths in Bi-2223 tapes is addressed by measuring the magnetic field dependence of the critical current density of tapes made by various producers. The study reveals whether it also affects pinning at low-angle grain boundaries and intra-granular flux pinning.

Based on the results obtained in Bi-2223 tapes and the mechanisms that are responsible for the dissipation, the question whether the mechanisms apply to technical superconductors in general is addressed. Current flow in a variety of high-temperature superconductors is studied, such as Bi-2212 tapes and YBCO coated conductors. In analogue to Bi-2223 tapes, these samples show a similar dependence of the critical current density on magnetic field. A distinct low-field contribution to the overall critical current density points to the existence of a weakly-linked network in the current path. This is supported by the existence of multiple current paths in YBCO coated conductors, observed with magneto-optical imaging in chapter 3. The parallel path model is applied to verify whether the mechanisms that limit the critical current density in this wide variety of samples are comparable to those in Bi-2223 tapes, suggesting a more general picture of current flow in granular high-temperature superconductors.

5.1. Coupling between pinning mechanisms in Bi-2223 tapes

Based on the results obtained in the previous chapter, a coupling between inter- and intra-granular flux pinning is expected in Bi-2223 tapes. It is verified whether a coupling as is described for YBCO exists, where flux pinning at low-angle grain boundaries depends on the interaction between Abrikosov-Josephson (*AJ*-) vortices at the grain boundary with Abrikosov (*A*-) vortices within the grains. The model predicts a large influence on the magnetic field dependence of the critical current density of the weakly-linked network as soon as flux pinning in the strongly-linked backbone is changed. It is verified whether an effective and reversible method to change intra-granular flux pinning exists, that enables a gradient in pinning strength within the grains to study the coupling between pinning mechanisms.

5.1.1. Influencing flux pinning

To select a technique most suitable for the variation of intra-granular flux pinning in Bi-2223 tapes, an overview of factors that change intra-granular flux pinning in high-temperature superconductors is presented. Included are defects in the crystalline structure that are introduced by a variation of radiation techniques and doping or substitution of elements in the lattice. Techniques that can have a smaller effect on pinning but have the advantage of being reversible are introduced as well.

Strong intrinsic pinning between the CuO_2-layers in layered high-temperature superconductors is observed for magnetic fields applied perpendicular to the *c*-axis of the grains. For magnetic fields applied parallel to the *c*-axis, pinning normally occurs at defects in the crystalline structure, for instance at screw dislocations [146] and twinning planes in YBCO [147]. Several approaches to increase the pinning of flux lines in single crystals and tapes are reported in literature. Pinning is for instance affected by introducing columnar defects resulting from heavy ion irradiation [148,149,150,151]. Parallel linear tracks that act as strong pinning sites for flux lines are formed in the crystalline structure. Also splayed columnar defects can be introduced by proton irradiation, where the tracks are oriented randomly through the sample [152,153]. The advantage of splayed defects over columnar defects is that the disorder in the pinned flux lattice is enhanced, which leads to a higher critical current density.

A weaker form of pinning occurs at point-like defects, which are introduced by oxygen vacancies [154] or electron irradiation [155,156]. The effect of point-like defects is much smaller than of columnar tracks [157,158,159,160,161,162], due to the vortex structure in layered high-temperature superconductors. Magnetic and Josephson interactions between vortex segments in adjacent CuO_2-layers are not sufficiently strong

to compete with thermal- and pinning disorder. Flux lines occur uncorrelated from one layer to the next throughout a large part of the temperature- and field domain [163,164,165]. The pancake vortices in individual layers are able to move without undergoing an interaction with vortices in the neighboring layers. Pancake vortices therefore have to be pinned individually.

Oxygen doping not only affects the number of point-like defects but also changes the anisotropy of the material [166]. Intra-granular flux pinning is affected strongly by lowering the anisotropy [167,168], which increases the coupling between the CuO_2-planes [169]. The method is also favored because oxygen doping is reversible. When oxygen is removed or added at temperatures below the decomposition temperature of the Bi-2223 phase, the microstructure and composition of the tape will not be affected. The other option, creating defects using irradiation, has a larger effect on pinning but is irreversible and therefore less suitable.

Another advantage of changing the oxygen concentration to vary the pinning in Bi-2223 tapes is the option of forming a concentration gradient in the grains of the tape. Oxygen diffuses along the *a*-axis of the crystal, starting at the grain boundary [170]. When oxygen is first removed, a concentration gradient develops within the grains. The oxygen concentration is reduced near the grain boundaries, while the oxygen concentration near the center of the grains is reduced at a lower rate. A gradient in oxygen content also occurs when oxygen is brought back into the sample. The concentration near the grain boundaries will be higher than in the interior of the grains. The formation of a gradient is a valuable tool to investigate if the weak link current density (J_{cw}) is influenced by the pinning of vortices near the grain boundaries. If this is the case, inter-granular flux pinning within the weakly-linked network will be restored before intra-granular flux pinning in the strongly-linked backbone after oxygen diffused back into the tape.

For this study, oxygen doping is selected to influence intra-granular flux pinning in Bi-2223 tapes. Intra-granular flux pinning is altered in an effective and reversible way. It also has the advantage of creating a gradient in pinning strength within the grains.

5.1.2. Oxygen deficiency in Bi-2223 tapes

An oxygen concentration gradient in the grains is applied to investigate whether an interaction between *AJ*-vortices at low-angle grain boundaries and intra-granular *A*-vortices exists in Bi-2223 tapes. In the experiment, the highest concentration of oxygen (and strongest intra-granular pinning) is present close to the grain boundaries. It is expected that such a concentration gradient has a larger effect on the weakly-linked network than it has on the strongly-linked backbone when inter- and intra-granular flux pinning are coupled. Whether this is the case is verified by analyzing the change in maximum pinning force in both current paths.

Four fully oxygenated Bi-2223 tapes from the same batch are selected (B-9, table 5.1). Oxygen is removed from the samples by annealing in pure argon atmosphere at 700°C for various time periods (B-9a to B-9d; table 5.2). The change in oxygen can be monitored by measuring the critical temperature (T_c). An annealing temperature of 700°C is chosen because it is the highest temperature at which no microstructural changes are introduced in the tape [171], and because the oxygen diffusion rate increases with increasing temperature. In order to create an oxygen concentration gradient and to verify whether the process is reversible, oxygen is first removed from the tape (B-9a) followed by a diffusion of oxygen back into the tape (B-9a+A) when the same sample is annealed at 700°C in air.

	Superconductor	Sample form	Matrix/ Substrate	Superconducting Cross-section (mm^2)	I_c in self-field [A]
B-4	Bi-2223	Tape	Ag	0.31	36 (77 K)
B-5	Bi-2223	Tape	Ag	0.31	65 (77 K)
B-6	Bi-2223	Tape	AgMg	0.18	30 (77 K)
B-7	Bi-2223	Tape	Ag	0.39	135 (77 K)
B-8	Bi-2212	Tape	AgMg	-	300 (4.2 K)
B-9	Bi-2223	Tape	Ag	-	65 (77 K)
Y-3	YBCO	CC	Ni	0.004	10 (77 K)
Y-4	YBCO	CC	NiW	0.012	70 (77 K)

Table 5.1. Selected properties of the superconducting samples studied in chapter 5.

First, the effect of a reduced oxygen concentration on intra-granular pinning is demonstrated. The decrease in oxygen is confirmed by measuring the critical temperature of the samples after annealing. The critical temperature is obtained by measuring the magnetic moment with the dc-magnetization method between 4.2 K and 120 K in an external magnetic field of 1 mT, after the samples are cooled in zero field to 4.2 K. The critical temperature of the sample is defined using three criteria. According to these criteria, T_c is the temperature at which the magnetic moment is 1 %, 50 % and 90 % of its value at 4.2 K (figure 5.1 and table 5.2).

The critical temperature of Bi-2223 tapes can only be changed in a small temperature window of approximately 10 degrees, which is already reached within 38 hours of annealing. This is in contrast with Bi-2212, where T_c reaches a maximum of around 90 K in the optimally doped state and decreases to below 40 K when it becomes underdoped [172]. The maximum T_c of Bi-2223 has been reported when samples are annealed under optimized conditions [173,174,175]. The magnetization measurements

show that a reduction in oxygen concentration results in a decrease of the critical temperature and a widening of the superconducting-to-normal transition.
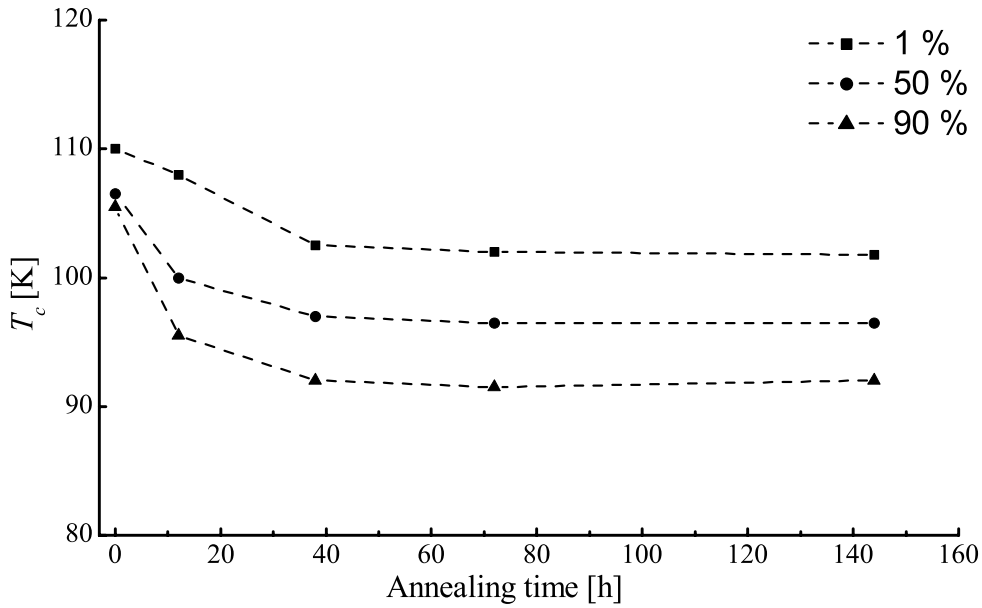
Figure 5.1. Measured critical temperature of Bi-2223 tapes B-9a to B-9d versus annealing time. T_c is defined as the temperature where the magnetic moment after zero-field-cooling is 1 %, 50 % and 90 % of the magnetic moment at 4.2 K. The lines are a guide to the eye.

	Annealing atmosphere	Annealing time [h]	T_c [K] 1 % of 4.2 K	T_c [K] 50 % of 4.2 K	T_c [K] 90 % of 4.2 K
B-9	-	-	110	107	106
B-9a	Ar	12	108	100	96
B-9a+A	Ar/Air	12/12	110	106	102
B-9b	Ar	38	103	97	92
B-9c	Ar	72	102	97	92
B-9d	Ar	144	102	97	92

Table 5.2. Critical temperature of the Bi-2223 tapes that are annealed under various conditions at 700°C.

The change in flux pinning in Bi-2223 tapes due to the varied oxygen concentration results in a change of the irreversibility field (B_{irr}) at which the critical current density decreases to zero. The irreversibility field is reduced when the annealing

time is increased, as shown by the magnetic field dependence of the critical current density (figure 5.2). Here, the critical current density is plotted as function of magnetic field at 50 K for the samples listed in table 5.2, when the magnetic field is applied perpendicular to the wide side of the tape. The critical current density of the samples is extracted from a dc-magnetization measurement and is normalized to that of the untreated sample (B-9) at 4.2 K in zero field. Also the overall critical current density decreases with decreasing oxygen concentration. No change in pinning and critical temperature is observed when the annealing time exceeds 38 hours, which means that the oxygen concentration in the tape remains unchanged.
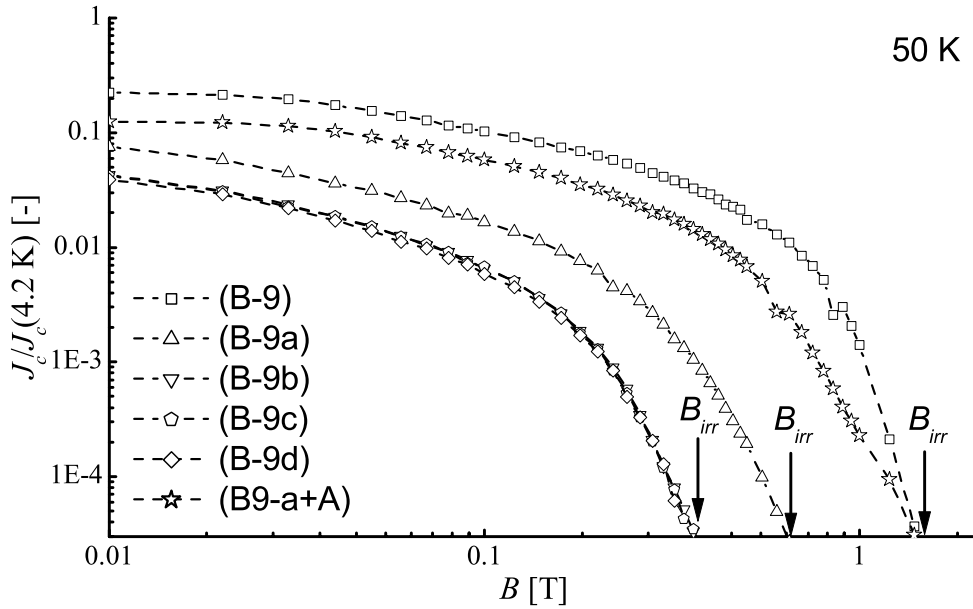
Figure 5.2. Critical current density, normalized to that of sample B-9 at 4.2 K and zero field, as function of magnetic field of Bi-2223 tapes B-9 to B-9d at 50 K. The dashed lines are a guide to the eye.

The change in intra-granular pinning due to the variation in oxygen concentration is clearly visible when the temperature dependence of the irreversibility field is considered (figure 5.3). The temperature dependence itself does not change significantly; only the absolute value of B_{irr} decreases. Therefore it is concluded that the pinning mechanism does not change in nature when oxygen is removed.

The coupling between intra-granular flux pinning and pinning at low-angle grain boundaries in the weakly-linked network is investigated by comparing the effect of oxygen concentration on the magnetic field dependence of the critical current density of both current paths. The reduction of intra-granular flux pinning due to a decrease in oxygen concentration results in a change in macroscopic pinning force (section 4.2.1).

Both macroscopic pinning force F_{pmax} and peak field B_{peak} decrease when oxygen is removed, while their temperature dependence remains unchanged (figures 5.4a and 5.4b). The macroscopic pinning force that is presented here corresponds to that of the strongly-linked backbone of the tape.
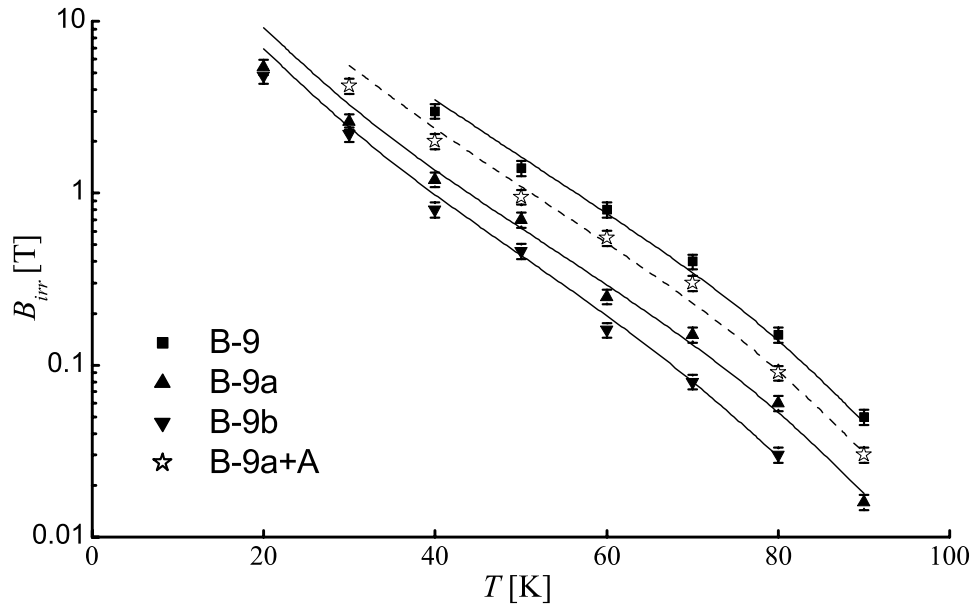
Figure 5.3. Temperature dependence of the irreversibility field of Bi-2223 tapes B-9 to B-9b. The irreversibility field is defined as the magnetic field at which the irreversible magnetic moment becomes smaller than 1×10^{-2} A/m and is obtained within an uncertainty of 10 %. The lines represent a power-law fit to the data (expression 4.9).

The reversibility of the effects of oxygen doping on T_c and intra-granular pinning is demonstrated first. Both critical temperature and the magnetic field dependence of the critical current density are obtained before (sample B-9) and after (sample B-9a) oxygen is removed at 700°C during 12 hours in argon. Oxygen diffuses back into the same tape when it is annealed at 700°C for 12 hours in air, after which $J_c(B)$ and T_c are measured again (sample B-9a+A). Intra-granular flux pinning and the critical temperature almost return to their original state after oxygen diffuses back into the sample (figures 5.1, 5.2 and 5.3). The results clearly demonstrate the reversibility of the annealing process. The small difference with the original sample is attributed to the fact that a longer annealing time at a higher oxygen pressure is needed in order to return the oxygen concentration to its original level.
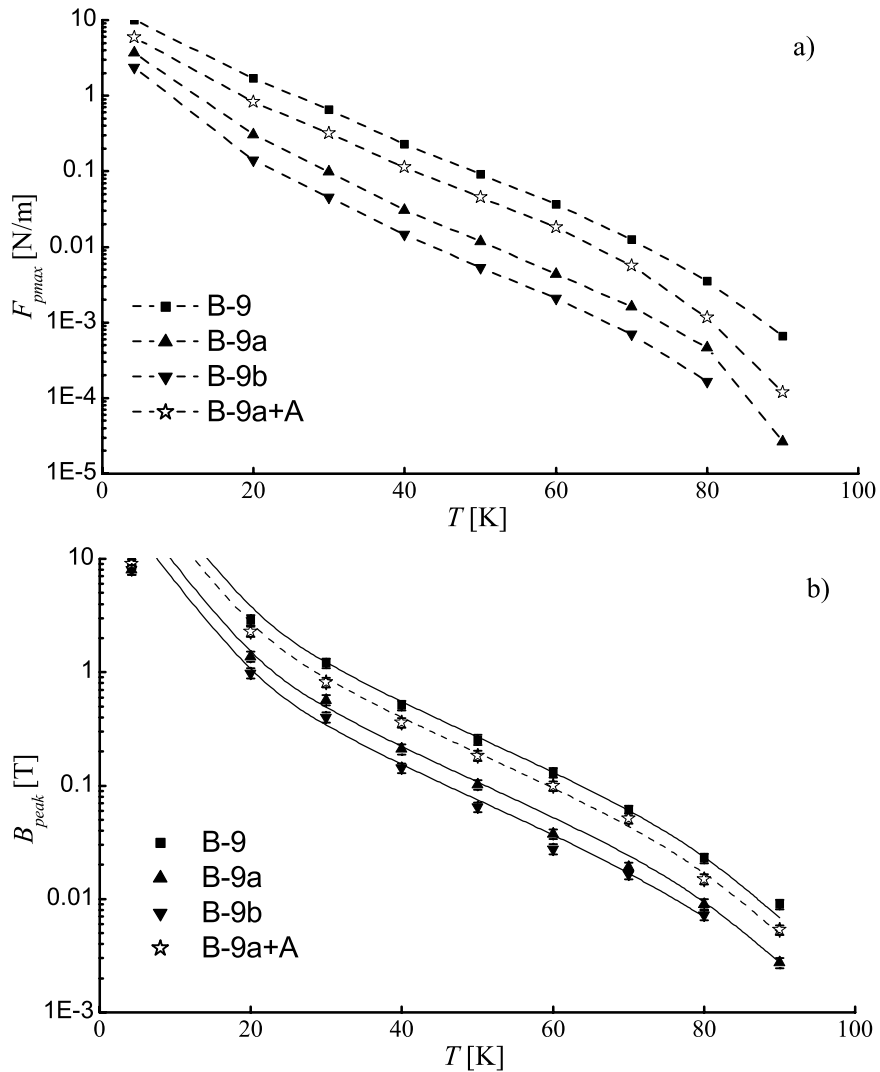
Figure 5.4. a) Temperature dependence of the maximum pinning force F_{pmax} of Bi-2223 tapes B-9 to B-9b. The dashed lines are a guide to the eye. b) Temperature dependence of the peak field B_{peak} at which the maximum pinning force is reached, obtained with an accuracy of 10 %. The lines describe the temperature dependence according to expression 4.9.

The coupling between intra-granular flux pinning and flux pinning at low-angle grain boundaries is investigated by analyzing the current in the weakly-linked network. The macroscopic pinning force of the weakly-linked network is calculated after the strong-links critical current density (expression 4.4) is subtracted from the overall critical current density of the tape. A decrease in pinning strength at low-angle grain boundaries

is observed when oxygen is removed from the tape (figure 5.5). The peak field at 70 K decreases to approximately 38 % of its original value when the tape is annealed in argon for 144 hours. This proves that inter-granular flux pinning in the weakly-linked current path is indeed coupled to intra-granular flux pinning.
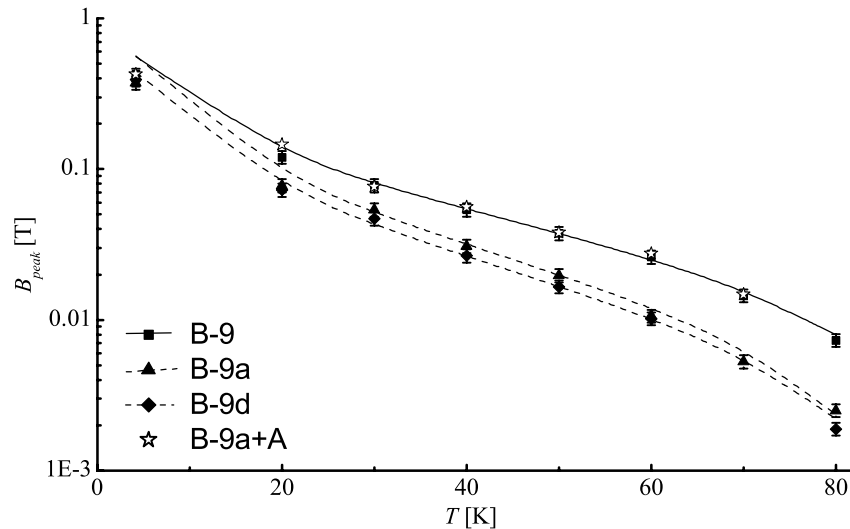
Figure 5.5. Temperature dependence of the peak field (B_{peak}) of the weakly-linked current path in Bi-2223 tapes B-9, B-9a, B-9d and B-9a+A. The values are obtained with an accuracy of 10 %. The lines describe the temperature dependence according to expression 4.9.

The coupling between inter-granular flux pinning and pinning near the grain boundaries becomes even clearer when flux pinning in the weakly-linked network is compared to that of the strongly-linked backbone, after oxygen diffused back into the tape (sample B-9a+A). Flux pinning within the weakly-linked current path is completely restored, which is observed in parameter B_{peak} that returns within 5 % of its value before oxygen is removed. This is not the case for the strongly-linked backbone, where the peak field returns to approximately 50 % of its original value. The gradient in oxygen concentration that develops in the grains causes the difference. As the grain interior takes up oxygen from the grain boundary area inward, the Abrikosov vortices close to the grain boundary recover their strongly-pinned character first and through interaction with the Abrikosov-Josephson vortices also improve the field dependence of the weakly-linked network. The behavior of the measured strong-links component reflects the situation in the entire grain volume, including the not yet fully oxygenated interior. It can be concluded that the interaction between AJ-vortices at the grain boundaries with A-vortices near the boundaries has a large effect on the critical current density of the weakly-linked network.

5.1.3. Conclusions regarding flux pinning in Bi-2223

A decrease in the irreversibility field and macroscopic pining force of the strongly-linked current path is observed when the oxygen concentration in the grains is reduced. This shows that the reduction of oxygen concentration is an effective process to change the intra-granular flux pinning in Bi-2223 tapes. Flux pinning does not change when the annealing time exceeds 38 hours. This is attributed to the minimized oxygen concentration. Flux pinning is completely restored after oxygen diffuses back into the tape, which shows that the process is reversible.

Inter-granular flux pinning at low-angle grain boundaries and intra-granular flux pinning near the grain boundaries are coupled. This conclusion is based on the following observations: 1) intra-granular oxygen concentration not only effects flux pinning within the grains, but also at low-angle grain boundaries and 2) inter-granular flux pinning in the weakly-linked network changes within a shorter time scale than intra-granular flux pinning in the strongly-linked backbone when the tape is annealed in air. The difference in time scale at which flux pinning at grain boundaries and within grains changes is the result of a gradient in oxygen concentration.

5.2. Improved connectivity and flux pinning in Bi-2223 tapes

A better grain connectivity due to an improved production process results in an increase of the overall cross section of both current paths in Bi-2223 tapes. Whether flux pinning in both current paths is affected by the improved production process is investigated by studying the magnetic field dependence of the critical current density. Three samples (B-4, B-5 and B-7), with a critical current ranging from 36 to 135 A at 77 K (table 5.1) are studied. The samples were used in chapter 4 to introduce the parallel path model. The temperature dependence of the scaling field (B_{scs} and B_{scw}) is assumed to be identical to that of the irreversibility field and is defined as follows:

$$B_{scs}(T) = B_{scs0}\left(\frac{T_c}{T} - 1\right)^{\frac{1}{n}} \text{ and} \tag{5.1}$$

$$B_{scw}(T) = B_{scw0}\left(\frac{T_c}{T} - 1\right)^{\frac{1}{n}}. \tag{5.2}$$

The magnetic field and temperature dependence of the critical current density of the strongly-linked backbone according to classical flux creep (expression 4.10) is repeated here for clarity.

$$J_{cs}(B,T) = J_{cs}(0,T) \exp\left(-\left(\frac{B}{B_{scs}(T)}\right)^{n_s} \ln\left(\frac{E_0(B,T)}{E_c}\right)\right).$$ (5.3)
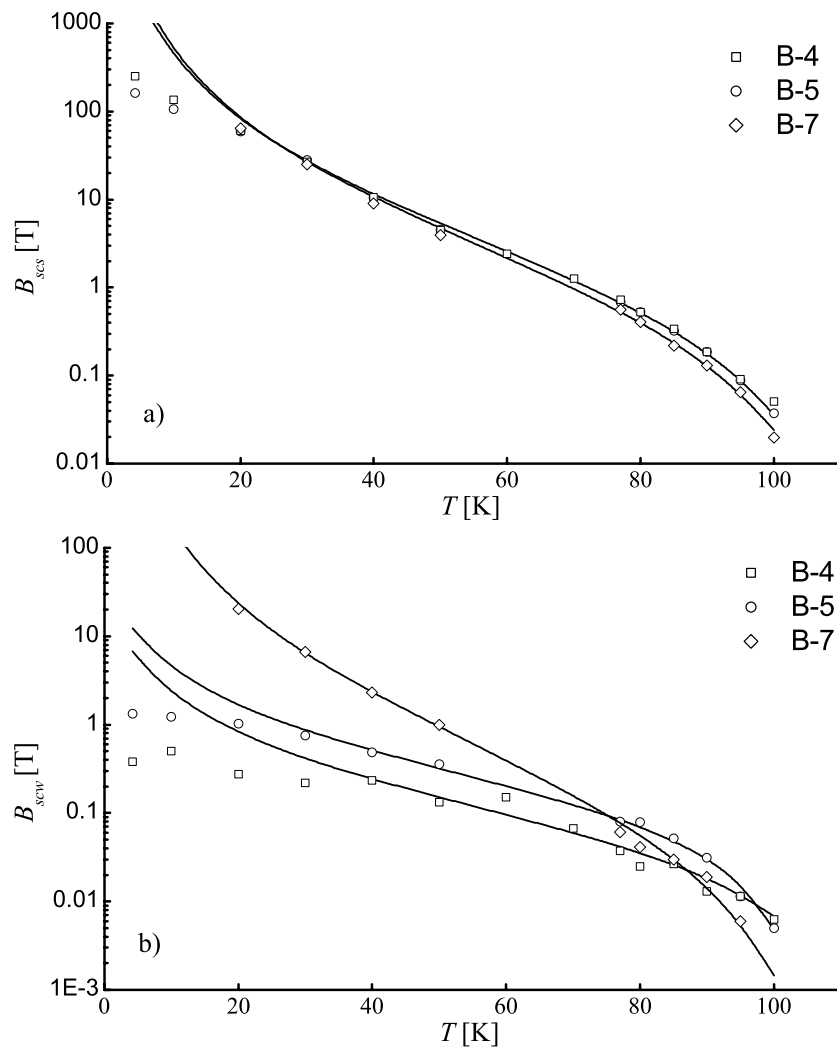
Figure 5.6. a) Temperature dependence of the strong-links scaling field B_{scs} of Bi-2223 tapes B-4, B-5 and B-7. b) Temperature dependence of B_{scw}. The solid lines represent expressions 5.1 and 5.2.

Table 5.3 lists the values of the parameters when the critical current density of various superconductors is described with expressions 5.1, 5.2 and 5.3. First, the influence of the production process on flux pinning in the strongly-linked backbone is studied by comparing the magnetic field dependence of its critical current density within the three tapes (figure 5.6a).

The temperature dependence (expression 5.1) that is used for the strong-links scaling field ($B_{scs}(T)$) is described by theory above 30 K. Intra-granular pinning strength varies between samples within 50 %. An improved cross-section of the current paths (increased overall critical current density) does not guarantee a stronger intra-granular flux pinning. This is concluded based on the fact that intra-granular pinning at high temperatures in the tape with the highest critical current density (B-7) is weaker than in both other samples.

	Expressions 5.1 and 5.2						Expression 5.3		
	$B_{scw}(T)$			$B_{scs}(T)$			$J_c(B,T)$		
	B_{scw0} [T]	T_c [K]	n [-]	B_{scs0} [T]	T_c [K]	n [-]	E_c [V/m]	n_w [-]	n_s [-]
B-4	0.12	110	0.8	3.7	110	0.5	10^{-4}	0.47	1.23
B-5 t	0.3	103	0.85	3.8	110	0.48	10^{-4}	0.47	1.23
B-5 m	0.08	108	1.00	1.35	110	0.43	10^{-5}	0.96	0.52
Powder	-	-	-	1.35	110	0.43	10^{-5}	-	0.52
B-6	0.2	110	0.6	3.2	110	0.47	10^{-4}	0.47	1.23
B-7	0.7	107	0.43	3.3	109	0.48	10^{-4}	0.47	1.23
B-8m	0.12	80	0.58	0.32	80	0.49	10^{-5}	0.43	1.4
B-9m	0.05	108	0.5	2.04	108	0.40	10^{-5}	0.96	0.52
Y-3	4.4	88	0.92	84	88	1.1	10^{-4}	0.29	1.1
Y-4	-	-	-	-	-	-	10^{-4}	0.29	1.1

Table 5.3. Values of the parameters in expressions 5.1, 5.2 and 5.3 of the superconductors that are presented in this thesis.

Inter-granular flux pinning in the weakly-linked network of Bi-2223 tapes is strongly correlated with the overall quality. The influence of the production process on the pinning in the weakly-linked network is reflected in the absolute value and the temperature dependence of its scaling field (B_{scw}) (figure 5.6b). At 20 K the scaling field of the weakly-linked network of the sample with the highest critical current (B-7) is approximately 10 times higher than the scaling field of the sample with the lowest critical current (B-4). The temperature dependence of B_{scw} becomes stronger when the overall quality of the tape increases, resulting in a lower value for n (table 5.3) in expression 5.1.

In fact, the temperature dependence of B_{scs} and B_{scw} of the sample with the highest quality (B-7) is identical.

It is reported in literature that the values of n in expressions 5.1 and 5.2 and n_s in expression 5.3 are similar [100]. This turns out to be not the case based on the results presented in this study. Both parameters are obtained independently from experiment. The value of n that reflects the temperature dependence of B_{scs} is approximately 0.5. A similar value (0.5) for n is reported in literature [98]. The value of n_s is obtained from the superconducting transition. At any given magnetic field at which the critical current density of the weakly-linked network is zero, n_s can be obtained from the $E(I)$-characteristic (expression 4.11) and is approximately equal to 1.23.

It is demonstrated that an improvement in production process that results in a larger cross-section of the current paths in Bi-2223 tapes does not result in a stronger intra-granular flux pinning. Intra-granular flux pinning depends on intrinsic properties within the grains, which are not affected by the connectivity between the grains. Inter-granular flux pinning at low-angle grain boundaries in the weakly-linked network does increase with improved grain connectivity and is next to an increased cross-section of the current path the field where most gain in conductor quality can be obtained.

5.3. Bi-2212 tapes

The behavior of the critical current density of Bi-2212 tapes is studied to verify whether similar mechanisms as in Bi-2223 tapes are responsible for the dissipation in these tapes. Bi-2212 tapes have a quite similar grain structure compared to Bi-2223 tapes. It is investigated whether a strongly-linked backbone exist by studying the high-field behavior of the critical current density and its dependence on oxygen content of the grains. Whether dissipation at low magnetic field occurs in a network of low-angle grain boundaries is studied by analyzed the critical current density with the parallel path model.

5.3.1. Intra-granular flux pinning in Bi-2212 tapes

In order to demonstrate the existence of a strongly-linked backbone in Bi-2212 tapes, it is investigated whether the critical current density at high magnetic fields is related to intra-granular flux pinning. Therefore, intra-granular pinning is changed by varying the oxygen content of the tape. Similar as reported on Bi-2223 in section 5.1.2., the resulting change in field dependence of the critical current density at high magnetic field is analyzed by means of the macroscopic pinning force.

Several results in literature show that intra-granular flux pinning in Bi-2212 is changed in a similar fashion as in Bi-2223 tapes by reducing the oxygen concentration of the tape. The main reason for this is that the anisotropy increases when the oxygen

content is decreased [167]. A second peak in the magnetization is often observed [160,168] and is caused by a transition in flux dynamics.

The effect of intra-granular flux pinning on the critical current density at high magnetic field is studied using three fully oxygenated Bi-2212 tapes from the same batch (sample B-8, table 5.1). Oxygen is removed from the samples following the same procedure as is done with Bi-2223 tapes (section 5.1.2), by annealing in pure argon atmosphere at 700°C for various time periods (samples B-8a to B-8c; table 5.4).

	Annealing atmosphere	Annealing time [h]	T_c [K] 1 % of 4.2 K	T_c [K] 50 % of 4.2 K	T_c [K] 90 % of 4.2 K
B-8	-	-	79	74	70
B-8a	Ar	36	93	83	75
B-8a+A	Ar/Air	36/48	84	78	74
B-8b	Ar	72	96	88	79
B-8c	Ar	159	86	72	62

Table 5.4. Annealing conditions and the resulting T_c of the Bi-2212 tapes that are analyzed in this subsection.
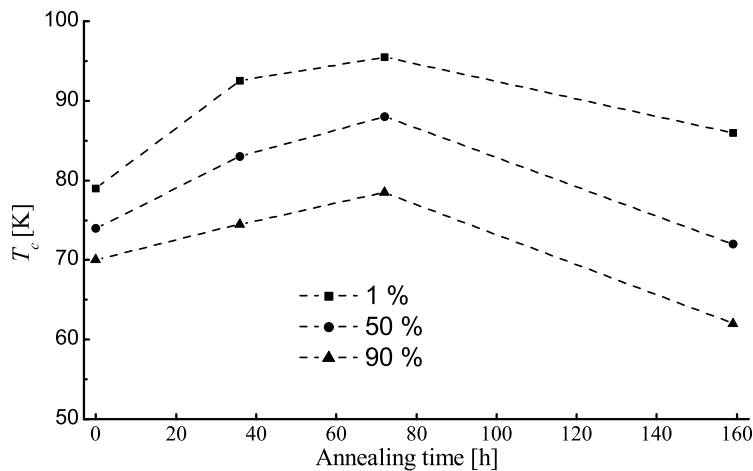
Figure 5.7. Critical temperature of Bi-2212 tapes B-8 to B-8c versus annealing time. T_c obtained using the dc-magnetization method is defined as the temperature where the magnetic moment after zero-field-cooling is 1 %, 50 % or 90 % of the magnetic moment at 4.2 K. The dashed lines are a guide to the eye.

The change in oxygen concentration is confirmed by measuring the critical temperature (T_c), which shows that the oxygen concentration has a considerable influence on the critical temperature of Bi-2212 tapes (figure 5.7). The critical temperature increases when the oxygen content decreases and goes through a maximum after

approximately 72 hours of annealing. When the tapes are annealed for a longer time period, T_c decreases as the oxygen content decreases further. Table 5.4 lists the relevant properties of Bi-2212 tapes B-8 to B-8c, which are annealed under various conditions. A similar dependence of the critical temperature on oxygen concentration is found in single crystals and thin films, where T_c first increases when oxygen is removed [170,172,174,176].
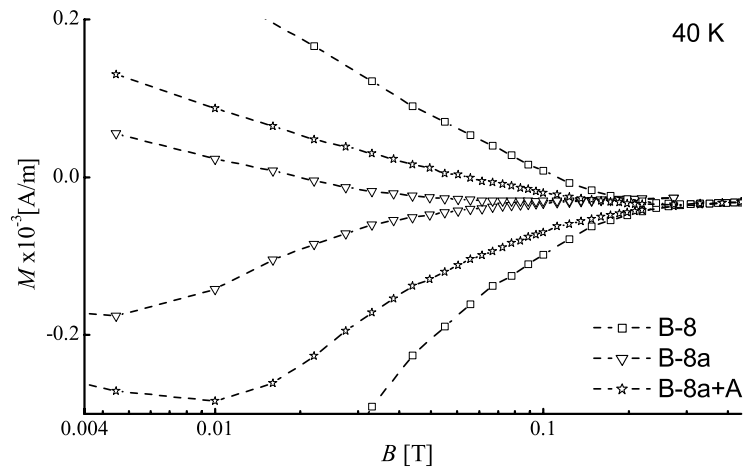
Figure 5.8. Magnetic moment as function of magnetic field of Bi-2212 tapes B-8, B-8a and B-8a+A at 40 K. The magnetic field is applied perpendicular to the wide side of the tape. The dashed lines are a guide to the eye.
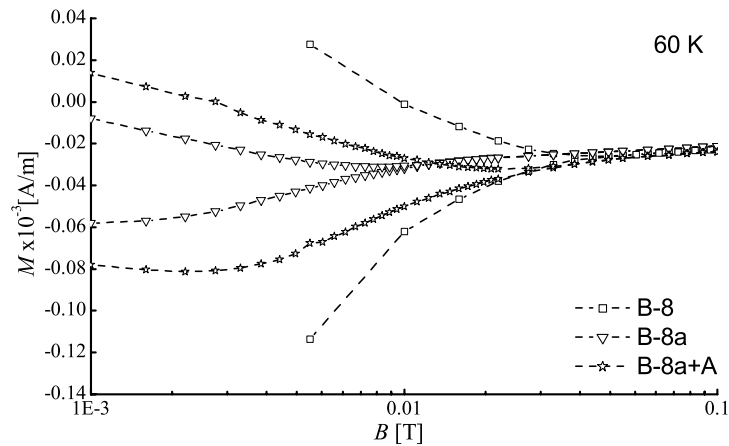
Figure 5.9. Magnetic moment as function of magnetic field of Bi-2212 tapes B-8, B-8a and B-8a+A at 60 K. The magnetic field is applied perpendicular to the wide side of the tape. The dashed lines are a guide to the eye.
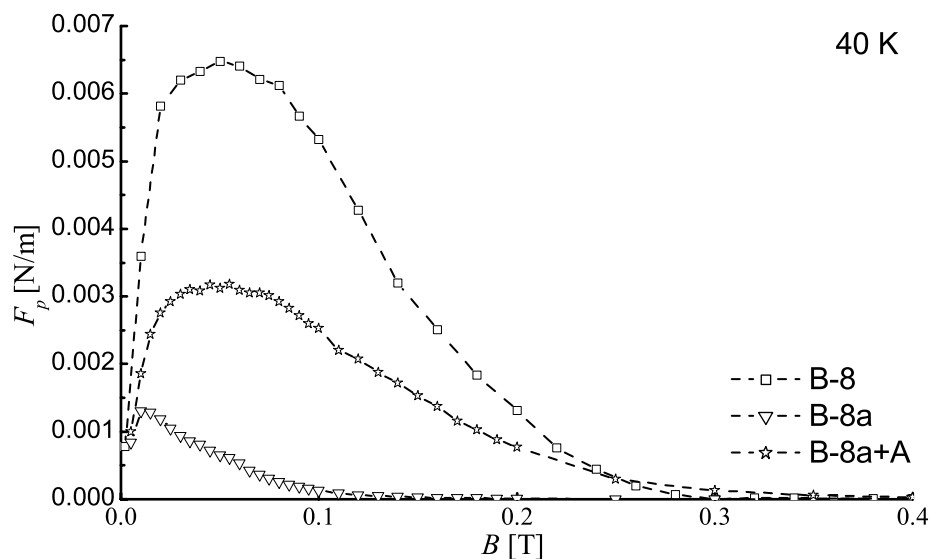
Figure 5.10. Macroscopic pinning force as function of magnetic field of Bi-2212 tapes B-8, B-8a and B-8a+A at 40 K. The magnetic field is applied perpendicular to the wide side of the tape. The dashed lines are a guide to the eye.
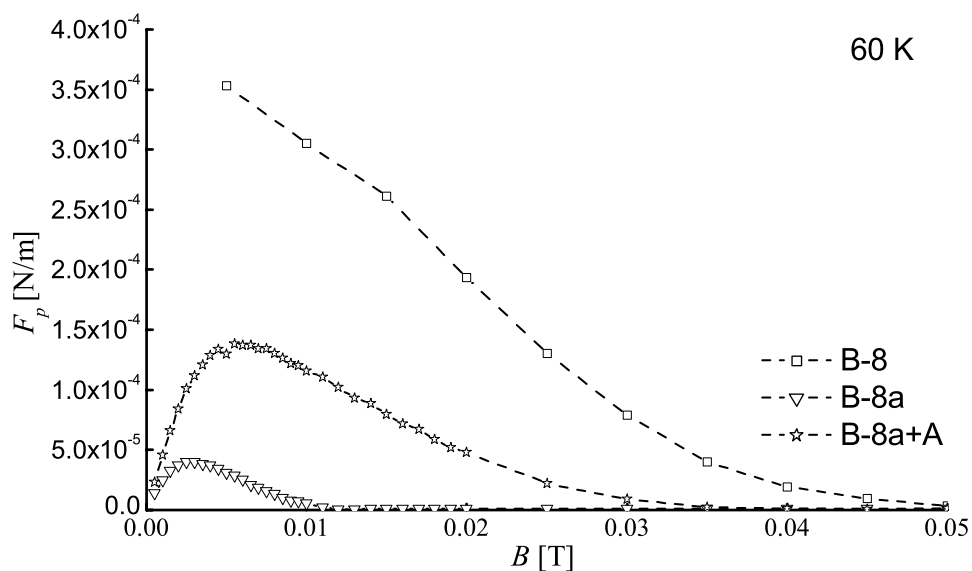
Figure 5.11. Macroscopic pinning force as function of magnetic field of Bi-2212 tapes B-8, B-8a and B-8a+A at 60 K. The magnetic field is applied perpendicular to the wide side of the tape. The dashed lines are a guide to the eye.

The influence of the oxygen concentration on intra-granular pinning strength in Bi-2212 tapes is analyzed by considering the macroscopic pinning force. The macroscopic pinning force is reduced when the amount of oxygen is decreased. This is shown in figures 5.10 and 5.11, where the macroscopic pinning force of samples B-8, B-8a and B-8a+A is shown at 40 K and 60 K. A maximum in pinning force is observed at both temperatures. The peak field and the absolute pinning strength decrease when oxygen is removed (sample B-8 and B-8a). The peak field at which the macroscopic pinning force is reached returns to its original value after sample B-8a is annealed in air (sample B-8a+A). The maximum pinning force is not recovered entirely due to possible damage to the sample, as is discussed earlier.

It is concluded that current in Bi-2212 tapes at high magnetic field is limited by intra-granular flux motion. The decrease in oxygen in Bi-2212 tapes by annealing in argon reduces intra-granular flux pinning in a similar fashion as in Bi-2212 single crystals and Bi-2223 tapes. The dependence of the critical current density on intra-granular flux pinning suggests that the current at high magnetic field in Bi-2212 tapes is carried by a backbone of strongly-linked grains.

5.3.2. Two pinning mechanisms in Bi-2212 tapes

In the previous subsection it is shown that current at high magnetic field in Bi-2212 tapes is limited by intra-granular flux motion. It is investigated next whether the critical current density at low field is limited by inter-granular flux motion at low-angle grain boundaries, as is the case with Bi-2223 tapes.

The similarities of current flow between Bi-2212 tapes and Bi-2223 tapes become evident when the critical current densities as function of magnetic field are compared (figure 5.12). The critical current densities of Bi-2212 tape B-8 and Bi-2223 tape B-5 are obtained with the dc-magnetization method at 30 K while the magnetic field is applied perpendicular to the wide side of the tape. A double step in the overall critical current density as function of magnetic field is observed, which indicates that two current paths in parallel exist in Bi-2212 tapes where the characteristic fields are sufficiently different. The parallel path model is applied to describe the behavior of the critical current density. The contributions of both current paths are described according to classical flux creep and are included in the figure.
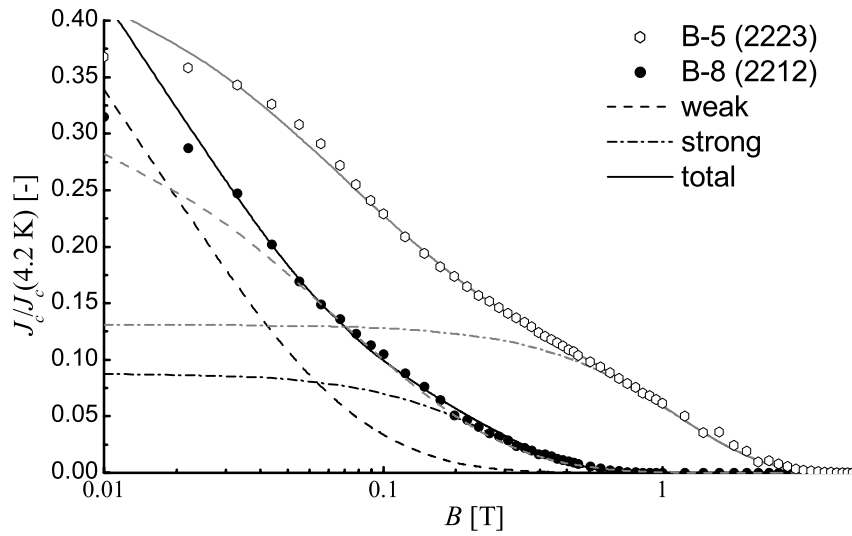
Figure 5.12. Critical current density of Bi-2223 tape B-5 and Bi-2212 tape B-8, as function of magnetic field at 30 K. The critical current density is normalized to its value at 10 K at zero field. The magnetic field is applied perpendicular to the wide side of the tape. The critical current density of both current paths of the Bi-2212 tape according to classical flux creep (expression 5.3) is included in the figure.
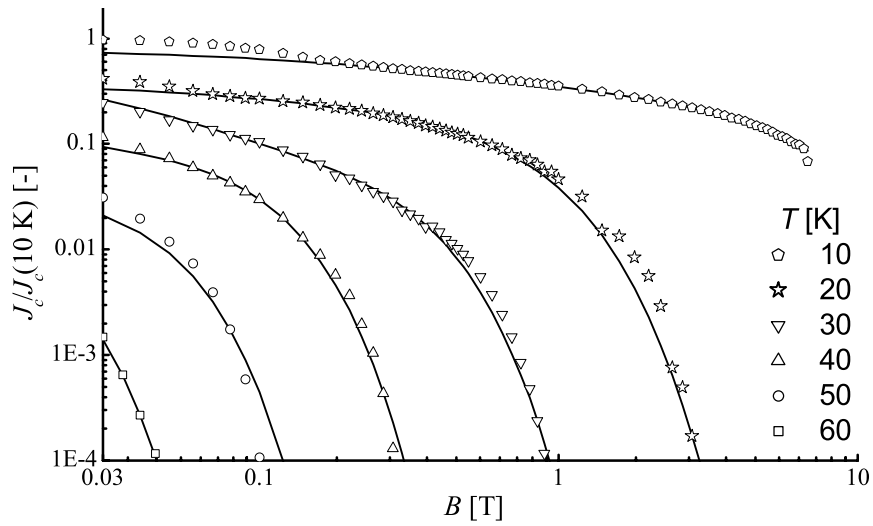
Figure 5.13. Critical current density of Bi-2212 tape B-8, normalized at 10 K and 30 mT, as function of magnetic field and temperature. The magnetic field is applied perpendicular to the wide side of the tape. The solid lines represent the overall critical current density when the critical current density of both current paths are described according to classical flux creep (expression 5.3).

The accordance between model and data shows that the model applies for both current paths, as is the case with Bi-2223 tapes. The magnetic field dependence of the critical current density is described in a similar way for different temperatures (figure 5.13). The critical current density is obtained with dc-magnetization and is normalized to its value at 10 K and 30 mT. The overall critical current density of the sample, according to the parallel path model (parameters as listed in table 5.3), is included in the figure. Similar as in Bi-2223, a good agreement between experiment and the parallel path model is observed for magnetic fields above the penetration field of the sample (50 mT at 20 K).
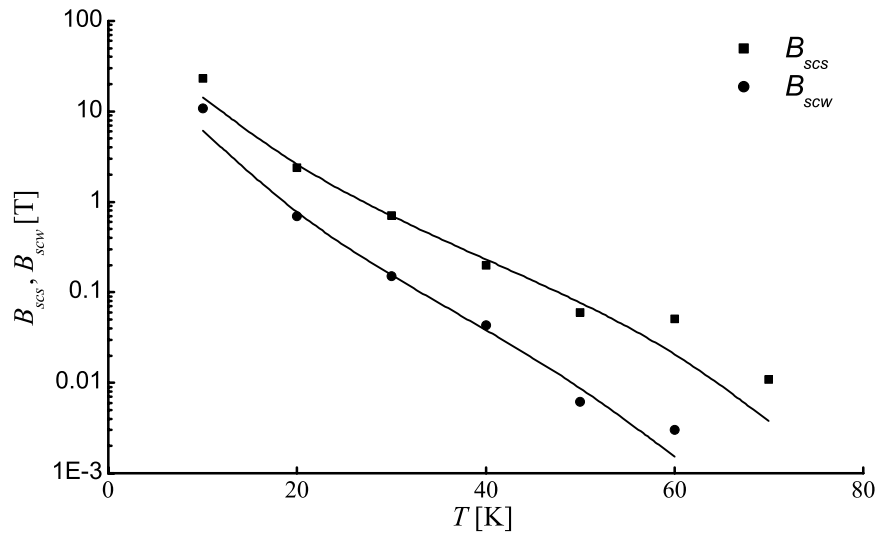
Figure 5.14. Temperature dependence of strong-links scaling field B_{scs} and weak-links scaling field B_{scw} of Bi-2212 tape B-8. The solid lines represent expressions 5.1 and 5.2.

Although similar mechanisms limit the critical current density in Bi-2212 and Bi-2223 tapes, a difference in pinning strength exists. This difference is shown in a comparison between the magnetic field dependence of the critical current density of both superconductors. The temperature dependence of the scaling fields B_{scs} and B_{scw} of both current paths in Bi-2212 tapes, are described by expressions 5.1 and 5.2 (figure 5.14). Smaller values of B_{scs0} en B_{scw0} apply to Bi-2212 tapes (table 5.3), which indicate a weaker pinning compared to Bi-2223 tapes. The temperature dependence is comparable to that of the scaling fields in Bi-2223 tapes (table 5.3). The temperature dependence of B_{scs} of the strongly-linked backbone in Bi-2212 corresponds to that found in Bi-2212 crystals [101] and films [177].

5.3.3. Conclusions on Bi-2212 tapes

The critical current density in Bi-2212 tapes is limited by intra-granular flux motion at high magnetic field. Current is carried by a backbone of strongly-linked grains as is the case in Bi-2223 tapes. Intra-granular flux pinning is reduced when the oxygen concentration of the tape is reduced. A contribution to the overall critical current density at low magnetic field points towards the presence of a weakly-linked network. Flux pinning in this network is weaker than that of the strongly-linked backbone and is described accurately by classical flux creep theory. From these results it is concluded that inter-granular flux motion at low-angle grain boundaries limits the critical current density of the weakly-linked network. Differences in intrinsic properties between Bi-2212 and Bi-2223 tapes (especially anisotropy) cause important quantitative differences in flux pinning strength.

5.4. YBCO coated conductors

YBCO coated conductors may well become the next generation of conductors for large-scale applications. Large improvements in their current carrying capabilities are still needed to make them economical attractive. The influence of its granularity on the overall critical current density is revealed in chapter 3 by combining the magneto-optical imaging and magnetic knife technique. Whether the presence of multiple current paths, which are formed due to the granularity of YBCO coated conductors, leads to a similar behavior of the critical current density as function of magnetic field as is the case in Bi-2223 tapes is investigated. Whether the smaller anisotropy of YBCO results in a stronger intra-granular flux pinning compared to Bi-2223 tapes is addressed by analyzing the behavior of the critical current density at high magnetic field. Also the role of low-angle grain boundaries and inter-granular flux motion is studied.

5.4.1. Comparing current flow in YBCO coated conductors and Bi-2223 tapes

The single layer of YBCO grains in samples prepared with pulsed-laser-deposition (PLD) enables a detailed comparison between grain connectivity and local critical current density, which is not possible with Bi-based tapes due to their more three-dimensional grain structure. The granularity of YBCO coated conductors has a large impact on a transport current, where current meanders around high-angle grain boundaries, as was shown with the magneto-optical imaging technique in chapter 3.

The meandering of the current in YBCO coated conductors gives rise to the assumption that current is running in multiple current paths similar to current flow in Bi-2223 tapes. The similarities between current flow in YBCO coated conductors and Bi-2223 tapes become evident in the magnetic field dependence of the critical current density (figure 5.15). At low magnetic field, the critical current density of a typical YBCO coated conductor (sample Y-4) at 77 K, normalized to its value at 20 mT, decreases at the same rate with increasing magnetic field as that of a Bi-2223 tape (B-7). The critical current density finally decreases to zero at high magnetic fields when the flux lines in the grains become unpinned.
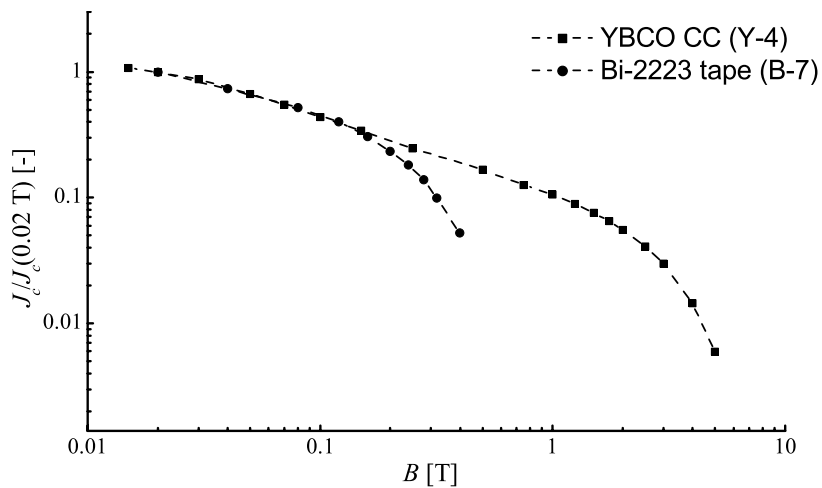
Figure 5.15. Critical current density as function of magnetic field of Bi-2223 tape B-7 and YBCO CC Y-4 at 77 K obtained with the transport method. The magnetic field is applied perpendicular to the wide side of the tape. The critical current density is normalized to its value at 20 mT. The dashed lines are a guide to the eye.

The main difference between both materials is that the critical current density of the YBCO coated conductor decreases to zero at a magnetic field almost ten times higher than the critical current density of Bi-2223 tapes. This is explained by a smaller anisotropy of 26 (ratio of effective mass for motion in the CuO_2-planes and normal to the planes) for YBCO [178] compared to 3000 for Bi-2212 [179,180], which causes a stronger intra-granular pinning of the strongly-linked backbone [69].

5.4.2. Critical current density in YBCO coated conductors

The magnetic field dependence of the critical current density of YBCO coated conductors at 77 K is similar as that of Bi-2223 tapes (figure 5.15). Based on the

similarities and the results presented in chapter 3 where the influence of the granularity on the overall critical current density was revealed, it is expected that; 1. Current in YBCO coated conductors is limited by grain boundaries and 2. Current paths of well-connected grains that carry the current at high field exist along the length of the conductor. To verify whether these assumptions are correct the parallel path model is applied to describe the behavior of the critical current density. It is expected that also here inter-granular flux motion at low-angle grain boundaries forms the dissipation mechanism at low field and that intra-granular flux motion limits the current of the strongly-linked backbone.

   The critical current of a YBCO coated conductor (sample Y-3) is measured as function of magnetic field for different temperatures using the transport method. A double step in the critical current density as function of magnetic field is observed over a large temperature range (figure 5.16). This is a strong indication for the existence of a weakly-linked network and a strongly-linked backbone in Bi-2223 tapes.
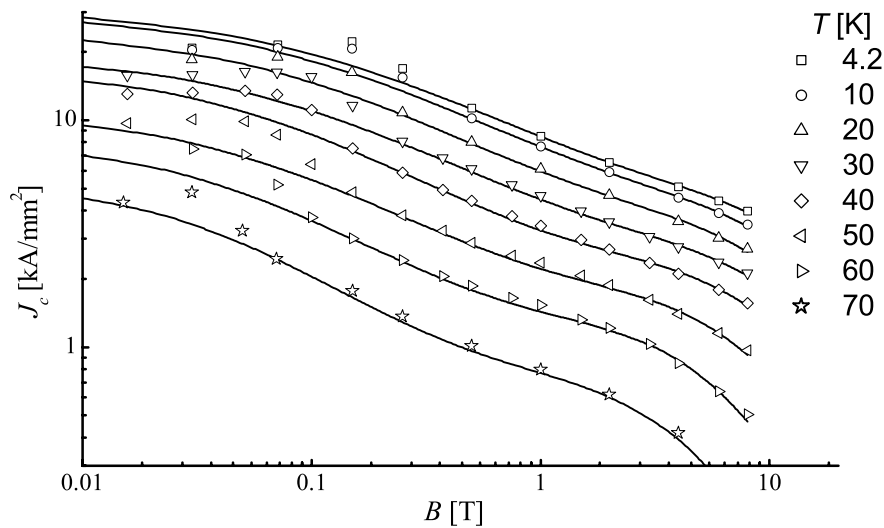
Figure 5.16. Critical current density as function of magnetic field for YBCO CC Y-3 at different temperatures. The magnetic field is applied perpendicular to the wide side of the conductor. The solid lines represent the overall critical current density when classical flux creep (expression 5.3) is applied to describe the contribution of both current paths.

   The double step in the critical current density as function op magnetic field is clearly seen for temperatures between 40 and 70 K. Below 40 K, the second step occurs at magnetic fields much higher than 8 T, which is outside the experimental window. This is also the case for temperatures above 70 K (figure 5.17), where the maximum applied field of 0.4 T is insufficient to reach the second decrease in the critical current density. The overall critical current density according to the parallel path model is included in both figures, when the contribution of both current paths is described according to classical

flux creep theory (expression 4.10). The parameters that are used in the parallel path model are listed in table 5.3. A good agreement between experiment and model is observed, except at low fields where the maximum in critical current density occurs.

Figure 5.17. Critical current density as function of magnetic field of YBCO CC Y-3 at different temperatures. The magnetic field is applied perpendicular to the wide side of the conductor. The solid lines represent the overall critical current density (expression 5.3).

A maximum in the overall critical current density is observed at low fields, ranging from 150 mT at 4.2 K to 20 mT at 77 K. This maximum for increasing field is not observed in Bi-based tapes and might be related to the grain structure of the coated conductor. In all likelihood, this maximum in the $J_c(B)$ dependence is attributed to geometrical factors. The combination of a wider sample and a large amount of grain boundaries that form channels for easy flux penetration in samples produced with PLD gives rise to this maximum. The maximum is not observed in samples that are produced with metal-organic-deposition (MOD), where a sample-wide grain connectivity is observed with MOI (sample Y-4 in section 3.2.3).

At high magnetic fields, the critical current density is expected to be limited by intra-granular flux motion. In that case, the voltage versus current characteristic of the superconducting transition is described using a power-law (expression 4.11). This assumption is investigated by measuring the current-voltage characteristic around the superconducting transition (figure 5.18).

A good agreement between experiment and model is observed below 70 K. At higher temperatures, a large part of the total critical current density is carried by the weakly-linked current path in the magnetic field range of the experiment. The assumption that the critical current density at high magnetic field is limited by intra-granular flux

motion is supported by the value of n_s in the model (expression 4.10) for the strongly-linked backbone, which corresponds to a close to linear field dependence of the activation energy U_0 of the strongly-linked backbone, as reported elsewhere [181,182].
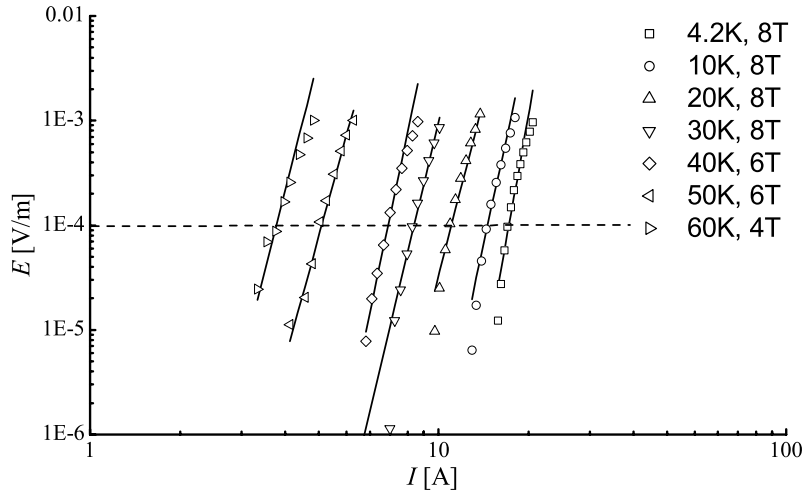
Figure 5.18. Electric field as function of current near the electric field criterion of YBCO CC Y-3. The solid lines represent a power-law dependence of the electric field on current (expression 4.11). The dashed line is the electric field criterion at which the critical current is defined.

Due to the lower anisotropy, a much stronger intra-granular flux pinning is observed in YBCO coated conductors compared to Bi-2223 tapes. This is not only the case at 77 K, as pointed out in the previous section, but from 4.2 K up to a temperature of only a few degrees under the critical temperature of YBCO (90 K). The stronger intra-granular flux pinning follows directly from the values of the strong-links scaling field (B_{scs}) (figure 5.19). A value of 28.9 T at 70 K is found for YBCO (Y-3), while a value of 1.25 applies to Bi-2223 at the same temperature (B-4). Similar values for the irreversibility field of YBCO at 77 K as found in this study are reported in literature [183,184,185,186].

The scaling field of the weakly-linked network of YBCO coated conductors is approximately ten times higher compared to Bi-2223 tapes (figure 5.19). Inter-granular flux pinning in YBCO coated conductors is largely enhanced due to the stronger intra-granular pinning strength.

The large pinning strength in the weakly-linked network is demonstrated when the magnetic field dependence at 77 K is regarded (figure 5.20). The critical current density of YBCO coated conductor Y-4 is shown, together with the contributions of both current paths (expression 5.3). The results show that at 77 K the weakly-linked network carries a significant part of the current in the coated conductor up to a field of approximately 1 T.
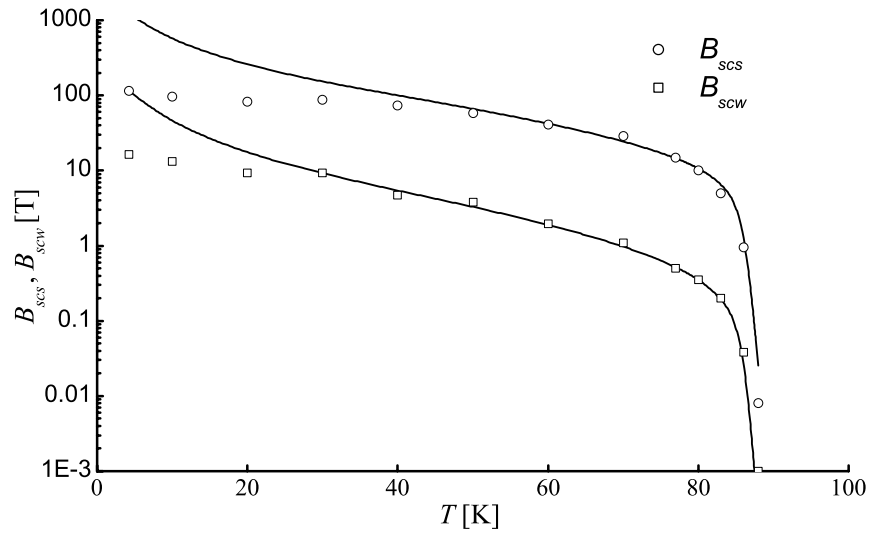
Figure 5.19. Temperature dependence of the weak-links and strong-links scaling fields B_{scw} and B_{scs} of sample Y-3. The solid lines represent the temperature dependence of the scaling fields (expressions 5.1 and 5.2).

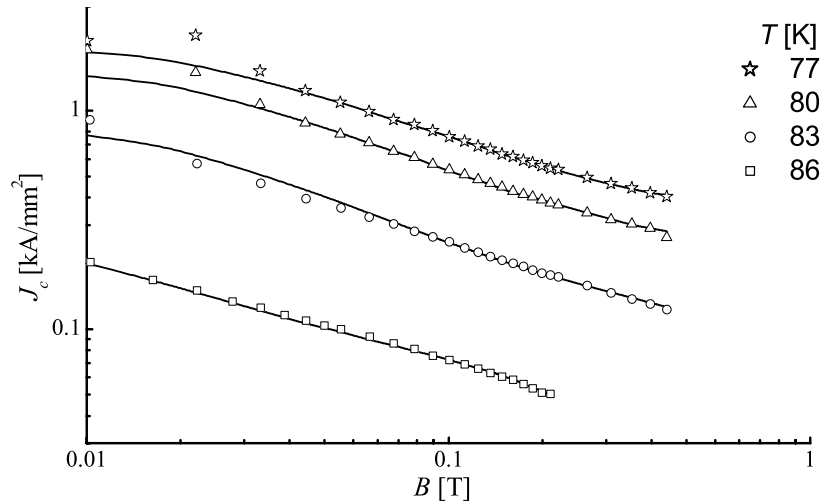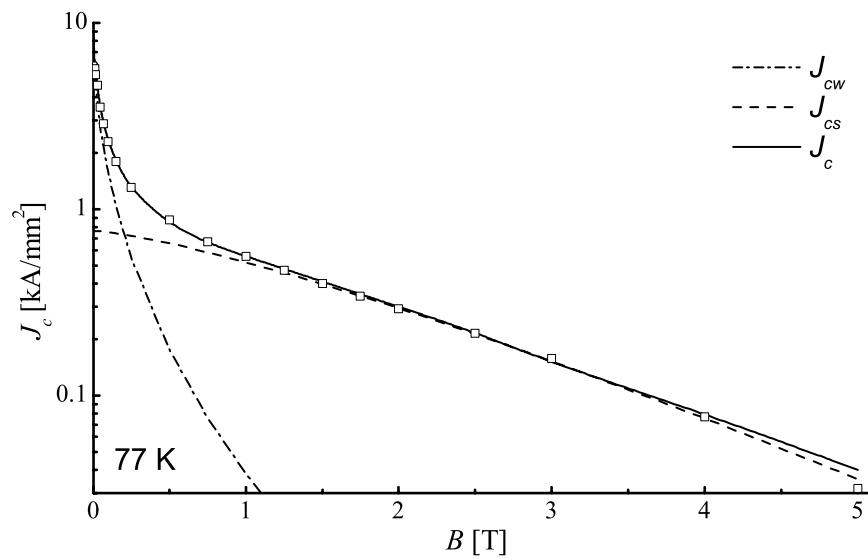Figure 5.20. Critical current density as function of magnetic field of YBCO coated conductor Y-4 at 77 K. The magnetic field is applied perpendicular to the wide side of the tape. The critical current density of both current paths is described with expression 5.3.

The coupling between inter-granular flux pinning at low-angle grain boundaries in the weakly-linked network and intra-granular flux pinning results in a similar temperature dependence of the scaling fields of both current paths (expressions 5.1 and 5.2). The similar temperature dependence of their critical current density at zero field supports this picture (figure 5.21). The critical current density at zero field as function of temperature of both current paths ($J_{0s}(T)$ and $J_{0w}(T)$) in Bi-2223 tape B-4 is included in the figure. The temperature dependence of J_{0w} is comparable to that of YBCO coated conductor Y-3, while that of J_{0s} of sample B-4 is temperature-independent below 30 K. The temperature dependence of J_{0s} in Bi-2223 tapes below 30 K may be the result of a change in coupling between the CuO_2-planes. The change in coupling does not occur in YBCO in the temperature range under investigation.

Figure 5.21. Temperature dependence of the critical current density at zero magnetic field of both current paths of YBCO CC Y-3 (closed symbols) and Bi-2223 tape B-4 (open symbols), normalized at 4.2 K. The dashed lines are a guide to the eye.

5.4.3. Conclusions on YBCO coated conductors

Multiple current paths in YBCO coated conductors lead to a similar magnetic field behavior of the critical current density compared to Bi-2223 tapes. A double step in critical current is observed, which indicates that current runs in two paths in parallel. The magnetic field dependence of the critical current density of both current paths is significantly different. The magnetic field dependence of the critical current density and the voltage-current characteristic at high field can be accurately described by classical flux creep.

The magnetic field dependence of the critical current density of the weakly-linked network is also described well with classical flux creep theory. It is therefore concluded that the weakly-linked network is formed by low-angle grain boundaries where current is limited by inter-granular flux motion. This is also concluded from the similar temperature dependence of the critical current density at zero field of the weakly-linked network and the strongly-linked backbone and the temperature dependence of the scaling fields of both current paths. A lower anisotropy (ratio of effective mass for motion in the CuO_2-planes and normal to the planes) of the grains in YBCO results in an increase in intra-granular flux pinning compared to Bi-2223 tapes. Inter-granular flux pinning is increased as well, due to the coupling between intra- and inter-granular flux pinning.

5.5. Conclusions

Two main conclusions can be drawn from the results that are presented in this chapter. The first main conclusion is that current in Bi-2223 tapes, Bi-2212 tapes and YBCO coated conductors can be described as running in two paths in parallel. The granularity of the conductors results in a weakly-linked network of low-angle grain boundaries that is formed parallel to a strongly-linked backbone of well-connected grains.

Several conclusions regarding current flow in granular high-temperature superconductors can be drawn:

- Intra-granular flux motion limits the current in the strongly-linked backbone.
- Inter-granular flux motion at low-angle grain boundaries limits the current in the weakly-linked network.
- Classical flux creep applies to pinning in both current paths.
- Pinning strength varies between different materials and is caused by a difference in intrinsic properties as for instance anisotropy. Stronger intra-granular flux pinning in YBCO coated conductors results in a characteristic field of 85 T, compared to 3.5 T for Bi-2223 tapes.

The second main conclusion is that a strong coupling exists between inter-granular flux pinning at low-angle grain boundaries in the weakly-linked network and intra-granular flux pinning. Abrikosov-Josephson vortices at low-angle grain boundaries are partly pinned by the grain boundary itself, but are also kept in place by Abrikosov-vortices near the grain boundary. This conclusion is based on the following observations:

- Intra-granular flux pinning in Bi-2223 tapes and Bi-2212 tapes can be changed effectively and reversibly by changing the oxygen concentration of the grains.

- Inter-granular flux pinning is reduced as a result of a reduced intra-granular flux pinning.
- Inter-granular flux pinning in Bi-2223 tapes is restored in a shorter time-scale compared to intra-granular flux pinning when oxygen diffuses back into the tape. This is explained according to the formation of a gradient in oxygen concentration in the grains.
- Inter-granular flux pinning increases with increasing grain connectivity. The scaling field of the weakly-linked network in Bi-2223 tapes increases and the temperature dependence of the scaling field becomes comparable to the temperature dependence of the scaling field of the strongly-linked backbone when the connectivity is improved.
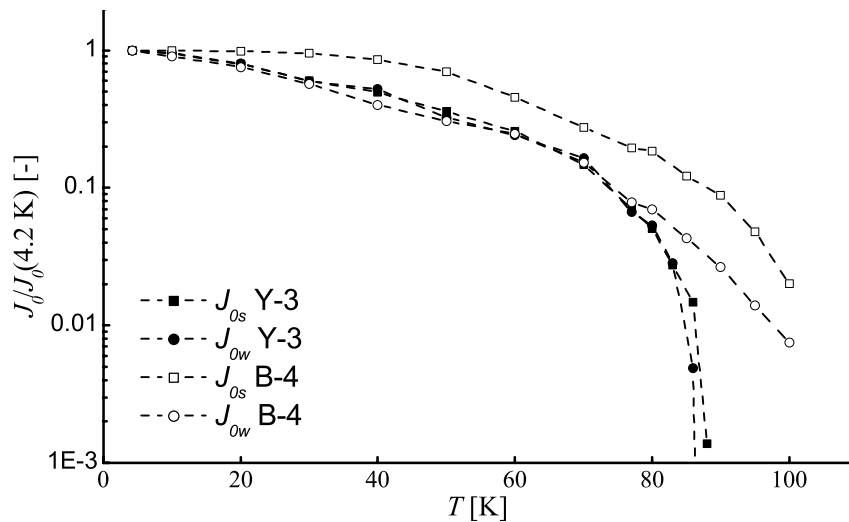- The temperature dependence of the critical current density at zero magnetic field of both current paths in YBCO coated conductors is identical. This, together with the identical temperature dependence of the scaling fields of both current paths points toward a coupling between inter-granular and intra-granular flux pinning.

Additionally a few conclusions can be drawn for conductor development and practical applications:

The main differences between Bi-2223 tapes of different quality are the overall critical current density and the magnetic field dependence of the critical current density of the weakly-linked network. Intra-granular flux pinning in the strongly-linked backbone does not vary significantly between conductors, as does the fraction of the current carried by the backbone at 77 K.

Conductor characterization needed for an optimized production process of Bi-2223 tapes can be kept to a minimum by measuring the magnetic field dependence of the critical current density at 77 K, by either transport current or magnetization methods. The overall critical current density is obtained from self-field measurement while the tape quality is obtained from the magnetic field dependence of the critical current density at low field, when the magnetic field is applied perpendicular to the wide side of the tape. The magnetic field dependence of the critical current density should be measured at an intermediate temperature (30-50 K) as well in case a complete conductor characterization is required. The temperature dependence of the scaling field varies between Bi-2223 tapes.

The magnetic field and temperature dependence of the critical current density of the YBCO coated conductor studied in this work can be largely obtained over the entire temperature range by measuring its properties at one temperature. This applies as long as the temperature dependence of the scaling fields of both current paths is identical. It is assumed that this is the case for YBCO coated conductors and high-quality Bi-2223 tapes.

Most practical applications in the temperature range of 65-77 K are operated at magnetic fields below 1 T. Current in Bi-based tapes is largely carried by the strongly-linked backbone in this magnetic field range, while the weakly-linked network in YBCO coated conductors still carries a large part of the current. This is an advantage of YBCO coated conductors over Bi-2223 tapes since the improvement in quality of YBCO coated conductors can be larger compared to Bi-based tapes. The quality of the conductor is not only improved when the cross-section of the strongly-linked backbone is increased, but the quality also benefits from the simultaneous increase of the cross-section of the weakly-linked network.

6. Conclusions

The conclusions that can be drawn from the results presented in this work are outlined in this conclusive chapter. The correlation between grain structure and critical current density of polycrystalline high-temperature superconductors is obtained from the combination of the magnetic knife technique, magneto-optical imaging and tensile strain. Poor grain-to-grain connectivity results in the formation of several current paths where current is limited by either intra-granular flux motion or by inter-granular flux motion at low-angle grain boundaries. Both mechanisms interact, which is demonstrated for the case of Bi-2223 tapes. The behavior of the critical current density of polycrystalline high-temperature superconductors can be described very accurately with classical flux creep.

Grain structure

The correlation between grain structure and macroscopic critical current density in YBCO coated conductors is studied by combining the magnetic knife and magneto-optical imaging. A good correlation between the spatial distribution of the critical current density and trapped flux in the grain structure is found.

The comparison between magneto-optical imaging and the magnetic knife shows that current in YBCO coated conductors is limited by clusters of high-angle grain boundaries and defects that are related to the production process and substrate. Defects that run in the longitudinal direction of the sample also suppress the critical current density on a length scale greater than 50 μm. Current meanders around high-angle grain boundaries and defects and has a significant component transverse to the longitudinal direction of the tape.

The magnetic knife experiment shows that the spatial variations of the overall critical current density of YBCO coated conductors produced with metal-organic-deposition are smaller than those produced with pulsed-laser-deposition. The improved grain connectivity in coated conductors produced with metal-organic deposition results in a Bean-like flux penetration, which is observed with magneto-optical imaging.

Transport measurements on deformed Bi-2223 tapes show that longitudinal strain affects weak links in the current path before if affects the strongly-connected grains. This conclusion is based on the stronger decrease in critical current at low field when strain is applied. Weak links in the current path of Bi-2223 tapes are formed by colony boundaries. This is concluded from the crack formation at colony boundaries as is observed with magneto-optical imaging. Flux penetrates colony boundaries in Bi-2223 tapes before strain is applied. Filaments break at the same locations after the applied strain exceeds the critical strain.

A difference between the colony structures of Bi-2223 and Bi-2212 tapes is observed when the crack formation is visualized with magneto-optical imaging. The filaments in Bi-2223 tapes break instantly, while cracks in Bi-2212 tapes propagate rather slowly when the applied strain is increased. Colony boundaries in Bi-2223 tapes run across the entire width of the filaments, which is due to intermediate rolling steps in the production process. The absence of intermediate rolling steps in the production process of Bi-2212 tapes and a different phase formation result in colony boundaries, which are not correlated to crack formation. Cracks are formed at weak locations such as pinholes, which do not commonly coincide with colony boundaries.

The combination of magneto-optical imaging and longitudinal strain shows that the grain structure and mechanical properties of the superconducting layer in YBCO coated conductors are largely influenced by the substrate of the conductor. The grains in the YBCO layer copy the grain structure of the metal substrate. This is concluded from the flux penetration along high-angle grain boundaries on a length scale comparable to the size of the grains in the substrate.

The location of strain-induced cracks in the YBCO layer is determined by the substrate and not by the YBCO grain structure. Not only colony boundaries, but also colonies themselves break open when strain is applied. Cracks run across part of the width of the sample. This leaves a relatively large path for transport current and results in a slower degradation of the critical current as function of applied strain compared to Bi-2223 tapes after the critical strain is exceeded.

Based on the results of this study on crack formation and propagation in Bi-based tapes and YBCO coated conductors, one can expect that the degradation of the critical current due to applied strain is independent of magnetic field in the following two materials:

- YBCO coated conductors, where cracks in the YBCO layer affect weak links and strongly-linked grains in the current path in a similar way, unlike cracks in the filaments of Bi-2223 tapes.
- Bi-2212 tapes, where the weak links in the current path are not per definition located at the weak spots in the filaments and the weak spots do not spread across the entire width of the filaments.

In order to determine the influence of longitudinal strain on the grain structure and critical current of high-temperature superconductors more accurately, the critical current of the sample should be measured within the magneto-optical imaging setup at the moment strain is applied.

Separate current paths in Bi-2223 tapes

Multiple current paths in Bi-2223 tapes are formed as a direct result of the grain structure of the conductor and form the basis for the parallel path model. The model describes current in Bi-2223 tapes as running in parallel paths where current is limited by two separate dissipation mechanisms. Dissipation at low magnetic field is due to inter-granular flux motion at low-angle grain boundaries that form a weakly-linked network. A second part of the current is carried by a backbone of strongly-linked grains at high magnetic field where intra-granular flux motion is the dissipation mechanism.

The hypothesis that current in Bi-2223 tapes can be described as flowing in two paths in parallel which have different microstructural properties is confirmed when the magnetic field dependence of the critical current density is analyzed as function of field angle. The magnetic field dependence of the critical current density for different angles can only be scaled accurately when both current paths are taken into account separately. From the dependence of the critical current density on magnetic field and field angle it is concluded that the separate current paths are each formed by different parts in the grain structure.

The dissipation mechanisms in both current paths are different in nature. The strongly-linked backbone is affected in a larger degree by the magnetic field component parallel to the c-axis of the grains, when the magnetic field is applied perpendicular to the wide side of the tape compared to the dissipation at the grain boundaries.

The magnetic field dependence of the weakly-linked current path, where the critical current density is limited by inter-granular flux motion at low-angle grain boundaries, is completely determined by the effective magnetic field component parallel to the c-axis of the grains. The effective field component is independent of temperature, which indicates that the current path and the dissipation mechanism do not change as function of temperature.

Dissipation in the strongly-linked backbone becomes more independent of field angle when the temperature is reduced from 50 K down to 4.2 K, at which temperature the critical current density becomes almost independent of field angle.

The dissipation mechanisms are analyzed independently when both current paths are physically separated. A weak-link-free powder is prepared from a Bi-2223 tape. The field and temperature dependence of the critical current density of the tape at high field and of the powder are identical. It is concluded that the critical current density of the strongly-linked backbone is limited by intra-granular flux motion and its behavior as function of magnetic field and temperature is described according to classical flux creep theory.

The dissipation mechanism of the weakly-linked network is attributed to inter-granular flux motion at low-angle grain boundaries and NOT Josephson behavior at high-angle grain boundaries. This is concluded from the critical current density of the weakly-linked network, which is much less field-sensitive than the critical current density of high-angle grain boundaries. Also its magnetic field dependence can not be described by a junction-based power-law, but is described in great detail with classical flux motion.

The mechanisms limiting the critical current density in the weakly-linked network and the strongly-linked backbone are related. Both current paths show a corresponding temperature dependence of the critical current density. This is observed when the critical current density of aligned Bi-2223 powder subtracted from the critical current density of the intact tape.

Coupling between pinning mechanisms

Although they are situated at different locations in the grain structure, the two mechanisms limiting the critical current density of the weakly-linked network and the strongly-linked backbone in Bi-2223 tapes are coupled. The variations in intra-granular and inter-granular flux pinning due to a change in oxygen concentration of the grains are compared. Both mechanisms are affected in a similar way. This is in accordance with the model where mixed Abrikosov-Josephson vortices at low-angle grain boundaries interact with Abrikosov-vortices in the neighboring grains. The model is valid for Bi-2223 tapes.

The effect of oxygen concentration on inter-granular flux pinning is caused by an interaction between inter-granular flux lines at low-angle grain boundaries with intra-granular flux lines close to the grain boundaries. The interaction causes pinning at low-angle grain boundaries to be restored before pinning in the strongly-linked backbone after oxygen diffuses back into the grains. This is due to an oxygen concentration gradient in the grains.

Both grain-to-grain connectivity and coupling between inter-granular and intra-granular flux lines determine the pinning strength at the low-angle grain boundaries in the weakly-linked network. The temperature dependence of the scaling field of the weakly-linked network becomes comparable to the temperature dependence of the scaling field of the strongly-linked backbone when the connectivity in the tape is improved.

Polycrystalline high-temperature superconductors

The importance of the grain-to-grain connectivity in polycrystalline high-temperature superconductors becomes evident from the results presented in this thesis. Multiple current paths are formed to get around high-angle grain boundaries and defects. Inter-granular flux pinning at low-angle grain boundaries and intra-granular flux pinning within the grains limit the critical current density of Bi-2223 tapes as well as Bi-2212 tapes and YBCO coated conductors. This is concluded from the good agreement between the behavior of the critical current density in these superconductors and the description with the parallel path model. In Bi-2212 tapes, the dependence of the critical current density at high magnetic field on oxygen concentration of the grains indicates that current at high magnetic field is carried by a strongly-linked backbone, similar as in Bi-2223.

Differences in intrinsic properties such as anisotropy result in a different intra-granular pinning strength between various polycrystalline high-temperature superconducting materials in this study (Bi-2223, Bi-2212 and YBCO).

Applications and conductor optimization

Two conclusions regarding applications for polycrystalline high-temperature superconductors can be drawn from the results presented in this study. First, the change in magnetic field angle dependence of the critical current density of the strongly-linked backbone in the Bi-2223 tapes investigated here below 50 K has a large impact on the design of high-field applications. The critical current decreases faster as function of magnetic field, applied at other angles than perpendicular to the wide side of the tape, then expected when the effective field component parallel to the c-axis of the grains is taken into account in the design. The change in coupling between the CuO_2-planes in Bi-2223 should be investigated in more detail by analyzing the magnetic field angle dependence of the critical current density at high fields. Whether the observed change also occurs in other Bi-2223 tapes, Bi-2212 tapes and YBCO coated conductors should be investigated as well.

The second conclusion is that YBCO coated conductors has two advantages over Bi-based tapes. The first advantage is a stronger intra-granular flux pinning in YBCO. The second advantage is related to the magnetic field range where the conductor is applied. The conductor is exposed to magnetic fields of up to 1 T in applications operated between 65K and 77 K, such as power applications. The weakly-linked network in YBCO coated conductors carries a significant fraction of the critical current in this magnetic field range, which is not the case for Bi-2223 tapes. Applications benefit from the improvement of both strongly-linked backbone and weakly-linked network with improved grain connectivity in YBCO coated conductors.

The following conclusions can be drawn regarding conductor characterization and optimization. The main difference between different quality Bi-2223 tapes next to the overall critical current density is the magnetic field dependence of the weakly-linked network in magnetic field applied perpendicular to the wide side of the tape. Both conductor properties can be obtained from a single measurement of the magnetic field dependence of the critical current density at for instance 77 K. A more detailed characterization of Bi-2223 tapes requires an additional measurement at intermediate temperature (30-50 K), because the temperature dependence of the scaling field of the weakly-linked network varies between conductors. The temperature dependence of both scaling fields above 30 K can be described accurately with a power-law. It is assumed that the temperature dependence of both scaling fields of high-quality Bi-2223 tapes and YBCO coated conductors is identical, as is the case for the highest quality Bi-2223 tape

and YBCO coated conductor studied in this work. An additional measurement at intermediate temperatures is not required for these conductors.

A higher conductor quality in Bi-based tapes and YBCO coated conductors can be obtained when the grain connectivity is increased when the grains become better aligned. As a result, more grain boundaries will contribute to the weakly-linked network and strongly-linked backbone and fewer grains will be connected at high angle. The improved grain-to-grain connectivity can be obtained by an improved production process. A second option of increasing the grain-to-grain connectivity is to increase the coupling between grains by proper doping at the grain boundaries. Doping could shift the grain boundary angle separating low- and high-angle grain boundaries to higher angles, resulting in a larger fraction of grain boundaries contributing to the current paths in polycrystalline high-temperature superconductors.

Improved grain connectivity also results in a change of the temperature dependence of the scaling field of the weakly-linked network, together with its absolute value. This is a result of an increased flux pinning at grain boundaries. Pinning of inter-granular flux lines can also be improved by increasing the coupling between flux lines at the grain boundaries and intra-granular flux lines. Further studies are required to verify whether flux pinning in the weakly-linked network can be improved by proper doping of the grains with for instance oxygen.

References

[1]   J. G. Berdnorz and K.A. Müller, *Z. Phys. B* **64**, 189-173 (1986).
[2]   K. Heine, J. Tenbrink and M. Thöner, *Appl. Phys. Lett.* **55** (23), 2441-2443 (1989).
[3]   Goyal, D.P. Norton, J.D. Budai et al., *Appl. Phys. Lett.* **69**, 1795-1797 (1996).
[4]   D.C. Larbalestier, A. Gurevich, D.M. Feldmann et al., *Nature* **414**, 368-377 (2001).
[5]   H. Hilgenkamp and J. Mannhart, *Rev. Mod. Phys.* **74**, 485-549 (2002).
[6]   J.F. Kwak, E.L. Venturini, P.J. Nigrey et al., *Phys. Rev. B* **37** (16), 9749-9751 (1988).
[7]   R. Flükiger, B. Hensel, A Jeremie et *al., Supcond. Sci. Technol.* **5**, S61-68 (1992).
[8]   F.A. List, A. Goyal, M. Paranthaman et al., *Physica C* **302**, 87-92 (1998).
[9]   B. ten Haken, A. Godeke and H.H.J. ten Kate, *J. Appl. Phys.* **85**, 3247-3253 (1999).
[10]   H.J.N. van Eck, L. Vargas, B. ten Haken et al., *Supercond. Sci. Technol.* **15** (8), 1213-1215 (2002).
[11]   B. ten Haken, "Strain effects on the critical properties of high-field superconductors", *Ph.D. Thesis*, University of Twente, The Netherlands (1994).
[12]   Y. Yeshurun and A. P. Malozemoff, *Phys. Rev. Lett.* **60** (21), 2202-2205 (1988).
[13]   H. Küpfer, S.N. Gordeev, W. Jahn et al., *Phys. Rev. B* **50** (10), 7016-7025 (1994).
[14]   B. ten Haken, H.J.N. van Eck and H.H.J. ten Kate, *Physica C* **334**, 163-167 (2000).
[15]   A.A. Polyanskii, X.Y. Cai, D.M. Feldmann et al., *Proc. of NATO Adv. Stud. Inst.*, Sozopol, Bulgaria, I. Nedkov and M. Ausloos, eds., 353-370 (1999).
[16]   A.A. Polyanskii, V.K. Vlasko-Vlasov, M.V. Indenbom et al., *Sov. Tech. Phys. Lett.* **15**, 872-873 (1989).
[17]   C.P. Bean, *Phys. Rev. Lett.* **8** (6), 250-253 (1962).
[18]   Y.Y. Xie, J.Z. Wu, A.A. Gapud et al., *Physica C* **322**, 19-24 (1999).
[19]   R.N. Bhattacharya, Z. Xing, J.Z. Wu et al., *Physica C* **377**, 327-332 (2002).
[20]   J.H. Su, P.V.P.S.S. Sastry, D.C. van der Laan, et al., *Adv. Cryogenic Eng. Mat*, **48B**, 639 (2002).
[21]   B. Hensel, G. Grasso and R. Flükiger, *Phys. Rev. B* **51** (21), 15456-15473 (1995).
[22]   Q. Li, W. Zhang, U. Schoop et al., *Physica C* **357**, 987-990 (2001).

[23]   M.W. Rupich, U. Schoop, D.T. Verebelyi et al., *IEEE Trans. Appl. Sup.* **13** (2), 2458-2461 (2002).

[24]   A.P. Malozemoff, S. Annavarapu, L. Fritzemeier et al., *Supercond. Sci. Technol.* **13**, 473-476 (2000).

[25]   D.M. Feldmann, J.L. Reeves, A.A. Polyanskii et al., *Appl. Phys. Lett.* **77** (18), 2906-2908 (2000).

[26]   B. ten Haken, H.J.N. van Eck and H.H.J. ten Kate, *Physica C* **334**, 163-167 (2000).

[27]   N. Amemiya, Y. Shinkai, Y. Iijima et al., *Supercond. Sci. Technol.* **14**, 611-617 (2001).

[28]   M.V. Indenbom, N.N. Kolesnikov, M.P. Kulakov et al., *Physica C* **166**, 486-496 (1990).

[29]   M.V. Indenbom, V.I. Nikitenko, A.A. Polyanskii et al., *Cryogenics* **30**, 747-749 (1990).

[30]   M.R. Koblischka and R.J. Wijngaarden, *Supercond. Sci. Technol.* **8**, 199-213 (1995).

[31]   D.M. Feldmann, J.L. Reeves, A.A. Polyanskii et al., *IEEE Trans. Appl. Sup.* **11** (1), 3772-3775 (2001).

[32]   J.L. Reeves, D.M. Feldmann, C-Y Yang et al., *IEEE Trans. Appl. Sup.* **11** (1), 3863-3867 (2001).

[33]   A.A. Polyanskii, A. Gurevich, A.E. Pashitski et al., *Phys. Rev. B* **53** (13), 8687-8697 (1996).

[34]   M. Turchinskaya, D.L. Kaiser, F.W. Gayle et al., *Physica C* **221**, 62-70 (1994).

[35]   Y.K. Huang, B. ten Haken and H.H.J. ten Kate, *IEEE Trans. Appl. Sup.* **9** (2), 2702-2705 (1998).

[36]   R. Passerini, M. Dhallé, L. Porcar et al., *Inst. Phys. Conf. Ser.* **67**, 607-610 (2000).

[37]   T. Kiss., *to be published*.

[38]   R. Passerini, M. Dhallé, B. Seeber et al., *Supercond. Sci. Technol.* **15**, 1507-1511 (2002).

[39]   D.C. Larbalestier, J.W.A. Anderson, S.E. Babcock et al., *Adv. Supercond.* **XI**, 805-810 (1999).

[40]   D. Dimos, P. Chaudhari, J. Mannhart et al., *Phys. Rev. Lett.* **61** (2), 219-222 (1988).

[41]   D. Dimos, P. Chaudhari and J. Mannhart, *Phys. Rev. B* **41** (7), 4038-4049 (1990).

[42]   N.F. Heinig, R.D. Redwing, I Fei Tsu et al., *Appl. Phys. Lett.* **69** (4), 577-579 (1996).

[43]   B. Mayer, L. Alff, T. Träuble et al., *Appl. Phys. Lett.* **63** (7), 996-998 (1993).

[44] T. Amrein, L. Schultz, B. Kabius et al., *Phys. Rev. B* **51** (10), 6792-6795 (1995).

[45] D.M. Feldmann, D.C. Larbalestier, D.T. Verebelyi et al., *Appl. Phys. Lett.* **79** (24), 3998-4000 (2001).

[46] H. Kitaguchi, K. Itoh, H. Kumakura et al., *IEEE Trans. Appl. Sup.* **11** (1), 3058-3061 (2001).

[47] R. Passerini, M. Dhallé, E. Giannini et al., *Physica C* **371**, 173-184 (2002).

[48] J.W. Ekin, D.K. Finnemore, Qiang Li et al., *Appl. Phys. Lett.* **61** (7), 858-560 (1992).

[49] B. ten Haken, A. Beuink, H.H.J. ten Kate, *IEEE Trans. Appl. Sup.* **7**(2), 2034-2037 (1997).

[50] *Handbook on Materials for Superconducting Machinery*, Batelle, Columbus, OH: Metals and Ceramics Information Center, (1977).

[51] M.R. Koblischka, T.H. Johansen and H. Bratsberg, *Supercond. Sci. Technol.* **10**, 693-701 (1997).

[52] M. Polak, J.A. Parrell, A.A. Polyanskii et al., *Appl. Phys. Lett.* **70** (8), 1034-1036 (1997).

[53] J. A. Parrell, A.A. Polyanskii, A.E. Pashitski et al., *Supercond. Sci. Technol.* **9**, 393-398 (1996).

[54] R. Flükiger, G. Grasso, J.C. Grivel et al., *Supercond. Sci. Technol.* **10**, A68-92 (1997).

[55] Z. Han and T. Freltoft, *Appl. Sup.* **2**, 201-215 (1994).

[56] D.C. van der Laan, H.J.N. van Eck, M.W. Davidson et al., *Physica C* **372**, 1020-1023 (2002).

[57] H. Miaa, H. Kitaguchi, H. Kumakura et al., *Cryogenics* **38**, 257-259 (1998).

[58] H. Miao, H. Kitaguchi, H. Kumakura et al., *Physica C* **301**, 116-122 (1997).

[59] E.E. Hellstrom and W. Zhang, *Physica B* **216**, 252-254 (1996).

[60] C.L.H. Thieme, S. Fleshler, D.M. Buczek et al., *IEEE Trans. Appl. Sup.* **9** (2), 1494-1497 (1999).

[61] D.C. van der Laan, H.J.N. van Eck, B. ten Haken et al., *IEEE. Trans. Appl. Sup.* **13** (2), 3534-3539 (2003).

[62] Goyal, D.F. Lee, F.A. List et al., *Physica C* **357**, 903-913 (2001).

[63] J.W. Ekin, T.M. Larson, A.M. Hermann et al., *Physica C* **160**, 489-496 (1989).

[64] L.N. Bulaevskii, J.R. Clem, L.I. Glazman et al., *Phys. Rev. B* **45** (5), 2545-2548 (1992).

[65] L.N. Bulaevskii, L.L. Daemen, M.P. Maley et al., *Phys. Rev. B* **48** (18), 13798-13816 (1993).

[66] J.L. Wang, X.Y. Cai, R.J. Kelley et al., *Physica C* **230**, 189-198 (1994).

[67] Y. Zhu, Q. Li, Y.N. Tsay et al., *Phys. Rev. B* **57** (14), 8601-8608 (1998).

[68]   P.H. Kes, J. Aarts, V.M. Vinokur et al., *Phys. Rev. Lett.* **64** (9), 1063-1066 (1990).
[69]   M. Tinkham, *Physica C* **235**, 3-8 (1994).
[70]   R. Kleiner, F. Steinmeyer, G. Kunkel et al., *Phys. Rev. Lett.* **68** (15), 2394-2397 (1992).
[71]   R. Kleiner and P. Müller, *Phys. Rev. B* **49** (2), 1327-1341 (1994).
[72]   P. Schmitt, P. Kummeth, L. Schultz et al., *Phys. Rev. Lett.* **67** (2), 267-270 (1991).
[73]   B. Hensel, J.-C. Grivel, A. Jeremie et al., *Physica C* **205**, 329-337 (1993).
[74]   M. Dhallé, M. Cuthbert, M.D. Johnston et al., *Supercond. Sci. Technol.* **10**, 21-31 (1997).
[75]   Y.K. Huang, B. ten Kate and H.H.J. ten Kate, *Physica C* **309**, 197-202 (1998).
[76]   D.C. van der Laan, H.J.N. van Eck, B. ten Haken et al., *IEEE Trans. Appl. Sup.* **11** (1), 3345-3348 (2001).
[77]   D.C. van der Laan, H.J.N. van Eck, J. Schwartz et al., *Physica C* **372**, 1024-1027 (2002).
[78]   E.J. Kramer, *J. Appl. Phys.* **44** (3), 1360-1370 (1973).
[79]   R. Wesche, *Physica C* **246**, 186-194 (1995).
[80]   M. Tachiki and S. Takahashi, *Solid State Comm.* **70** (3), 291-295 (1989).
[81]   M. Tachiki and S. Takahashi, *Solid State Comm.* **72** (11), 1083-1086 (1989).
[82]   V. Hussennether, O. Waldmann and P. Müller, *Phys. Rev. B* **62** (14), 9808-9817 (2000).
[83]   Q.Y. Hu, H.W. Weber, H.K. Liu et al., *Physica C* **252**, 211-220 (1995).
[84]   M.P. Maley, P.J. Kung, J.Y. Coulter et al., *Phys. Rev. B* **45** (13), 75667569 (1992).
[85]   B. Lehndorff, M. Hortig and H. Piel, *Supercond. Sci. Technol.* **11**, 1261-1265 (1998).
[86]   O. van der Meer, B. ten Haken and H.H.J. ten Kate, *Physica C* **357**, 1174-1177 (2001).
[87]   J.E. Tkaczyk, R.H. Arendt, M.F. Garbauskas et al., *Phys. Rev. B* **45** (21), 12506-12512 (1992).
[88]   M.N. Cuthbert, M. Dhallé, J. Thomas et al., *IEEE Trans. Appl. Sup.* **5** (2), 1391-1394 (1995).
[89]   M. Dhallé, F. Marti, G. Grasso et al., *Physica C* **282**, 1173-1174 (1997).
[90]   M. Dhallé, D.C. van der Laan, H.J.N. van Eck et al., *IEEE Trans. Appl. Sup.* 13 (2), 3702-3705 (2003).
[91]   P.W. Anderson and Y.B. Kim, *Rev. Mod. Phys.* **36**, 39 (1964).
[92]   P.W. Anderson, *Phys. Rev. Lett.* **9** (7), 309-311 (1962).
[93]   M.R. Beasley, R. Labusch and W.W. Webb, *Phys. Rev.* **181** (2), 682-700 (1969).

[94]   Y. Yeshurun, A. P. Malozemoff and A. Shaulov, *Rev. Mod. Phys.* **68** (3), 911-949 (1996).

[95]   E. Zeldov, N.M. Arner, G. Koren et al., *Phys. Rev. Lett.* **62** (26), 3093-3096 (1989).

[96]   E. Zeldov, N.M. Amer, G. Koren et al., *Appl. Phys. Lett.* **56** (7), 680-682 (1990).

[97]   M.P. Maley, J.O. Willis, H. Lessure et al., *Phys. Rev. B* **42** (4), 2639-2642 (1990).

[98]   G. Fuchs, E.S. Vlakhov, K.A. Nenkov et al., *Physica C* **247**, 340-346 (1995).

[99]   T.T.M. Palstra, B. Batlogg, L.F. Schneemeyer et al., *Phys. Rev. Lett.* **61** (14), 1662-1665 (1988).

[100]   H. Yamasaki, K. Endo, S. Kosaka et al., *Phys. Rev. B* **49** (10), 6913-6918 (1994).

[101]   Schilling, R. Jin, J.D. Guo et al., *Phys. Rev. Lett.* **71** (12), 1899-1902 (1993).

[102]   M.V. Feigel'man, V.B., Geshkenbein, A.I. Larkin et al., *Phys. Rev. Lett.* **63** (20), 2303-2306 (1989).

[103]   M. V. Feigel'man, V.B. Geshkenbein and V.M. Vinokur, *Phys. Rev. B* **43** (7), 6263-6265 (1991).

[104]   M.F. Chisholm and S.J. Pennycook, *Nature* **351**, 47-49 (1991).

[105]   A.M. Campbell, *Physica C* **162**, 273-274 (1989).

[106]   J. Mannhart, P. Chaudhari, D. Dimos et al., *Phys. Rev. Lett.* **61** (21), 2476-2479 (1988).

[107]   J. Mannhart, *J. of Supercond.* **3** (3), 281-285 (1990).

[108]   Q. Li, Y.N. Tsai, Y. Zhu et al., *Appl. Phys. Lett.* **70** (9), 1164-1166 (1997).

[109]   K. Kishida and N.D. Browning, *Physica C* **351**, 281-294 (2001).

[110]   O. Eibl, *Physica C* **168**, 239-248 (1990).

[111]   O. Eibl, *Physica C* **168**, 249-256 (1990).

[112]   Y. Yan, M.A. Kirk and J.E. Evetts, *J. Mat. Res.* **12** (11), 3009-3028 (1997).

[113]   Umezawa, Y. Feng, H.S. Edelman et al., *Physica C* **198**, 261-272 (1992).

[114]   Umezawa, Y. Feng, H.S. Edelman et al., *Physica C* **219**, 378-388 (1994).

[115]   Attenberger, J. Hänisch, B. Holzapfel et al., *Physica C* **372**, 649-651 (2002).

[116]   J. Hänisch, A. Attenberger, B. Holzapfel et al., *Phys. Rev. B* **65**, 052507 (2002).

[117]   K. Ohbayashi, H. Fujii, A. Kuzuhara et al., *IEEE Trans. Appl. Sup.* **5** (2), 2816-2819 (1995).

[118]   M. Prester, *Supercond. Sci. Technol.* **11**, 333-357 (1998).

[119]   J.E. Evetts and B.A. Glowacki, *Cryogenics* **28**, 641-649 (1988).

[120]   V.M. Svistunov, A.I. D'Yachenko and V.Y. Tarenkov, *Physica C* **185-189**, 2429-2430 (1991).

[121]   A.I. D'yanchenko, *Physica C* **213**, 167-178 (1993).

[122]   R.L. Peterson and J.W. Ekin, *Phys. Rev. B* **37** (16), 9848-9851 (1988).

[123]   R.L. Peterson and J.W. Ekin, *Physica C* **157**, 325-333 (1989).

[124]   H. Küpfer, I. Apfelstedt, R. Flükiger et al., *Cryogenics* **28**, 650-660 (1988).

[125]   T. Wolf and A. Majhofer, *Phys. Rev. B* **47** (9), 5383-5389 (1993).

[126]   P. Muné and J. López, *Physica C* **257**, 360-366 (1996).

[127]   L.L. Daemen, L.N. Bulaevskii, M.P. Maley et al., *Phys. Rev. B* **47** (17), 11291-11301 (1993).

[128]   J.R. Clem, *Physica C* **153-155**, 50-55 (1988).

[129]   K.-H. Müller and A.J. Pauza, *Physica C* **161**, 319-324 (1989).

[130]   K.-H. Müller, D.N. Matthews and R. Driver, *Physica C* **191**, 339-346 (1992).

[131]   C.J. Lobb, D.W. Abraham and M. Tinkham, *Phys. Rev. B* **27** (1), 150-157 (1983).

[132]   K. A. Delin and A.W. Kleinsasser, *Supercond. Sci. Technol.* **9**, 227-269 (1996).

[133]   V. Ambegaokar and A. Baratoff, *Phys. Rev. Lett.* **10** (11), 486-489 (1963).

[134]   E. Sarnelli, P. Chaudhari and J. Lacey, *Appl. Phys. Lett.* **62** (7), 777-779 (1993).

[135]   A. Gurevich and L.D. Cooley, *Phys. Rev. B* **50** (18), 13563-135576 (1994).

[136]   X.Y. Cai, A. Gurevich, I-Fei Tsu et al., *Phys. Rev. B* **57** (17), 10951-10958 (1998).

[137]   A. Gurevich, *Phys. Rev. B* **65**, 214531 (2002).

[138]   D. Kim, P. Berghuis, M.B. Field et al., *Phys. Rev. B* **62** (18), 12505-12508 (2000).

[139]   J. Albrecht, S. Leonhardt and H. Kronmüller, *Phys. Rev. B* **63**, 014507 (2001).

[140]   K.E. Gray, D.J. Miller, M.B. Field et al., *Physica C* **341**, 1397-1400 (2000).

[141]   P. Berghuis, D.J. Miller, D.H. Kim et al., *IEEE Trans. Appl. Sup.* **11** (1), 3868-3871 (2001).

[142]   A. Gurevich, M.S. Rzchowski, G. Daniels et al., *Phys. Rev. Lett.* **88** (9), 097001 (2002).

[143]   D.T. Verebelyi, C. Prouteau, R. Feenstra et al., *IEEE Trans. Appl. Sup.* **9** (2), 2655-2658 (1999).

[144]   D.T. Verebelyi, D.K. Christen, R. Feenstra et al., *Appl. Phys. Lett.* **76** (13), 1755-1757 (2000).

[145]   M. Däumling, E. Sarnelli, P. Chaudhari et al., *Appl. Phys. Lett.* **61** (11), 1355-1357 (1992).

[146]   J.M. Huijbregtse, B. Dam, R.C.F. van der Geest et al., *Phys. Rev. B* **62** (2), 1338-1349 (2000).

[147]   M.M. Fang, V.G. Kogan, D.K. Finnemore et al., *Phys. Rev. B* **37** (4), 2334-2337 (1988).

[148]   Hensel, B. Roas, S. Henke et al., *Phys. Rev. B* **42** (7), 4135-4142 (1990).

[149]   W. Gerhäuser, G. Ries, H.W. Neumüller, *Phys. Rev. Lett.* **68** (6), 879-882 (1992).

[150] H.W. Neumüller, G. Ries, W. Schmidt et al., *Supercond. Sci. Technol.* **4**, S370-S372 (1991).

[151] J.R. Thompson, Y.R. Sun, H.R. Kerchner et al., *Appl. Phys. Lett.* **60** (18), 2306-2308 (1992).

[152] L. Krusin-Elbaum, J.R. Thompson, R. Wheeler et al., *Appl. Phys. Lett.* **64** (24), 3331-3333 (1994).

[153] L. Krusin-Elbaum, G. Blatter, J.R. Thompson et al., *Phys. Rev. Lett.* **81** (18), 3948-3951 (1998).

[154] C.J. van der Beek and P.H. Kes, *Phys. Rev. B* **43** (16), 13032-13041 (1991).

[155] T. Nishizaki, T. Naito, S. Okayasu et al., *Phys. Rev. B* **61** (5), 3649-3654 (2000).

[156] A.V. Bondarenko, A.A. Prodan, Yu T. Petrusenko et al., *Phys. Rev. B* **64**, 092513 (2001).

[157] J-i Shimoyama, *Supercond. Sci. Technol.* **13**, 43-50 (2000).

[158] D.R. Nelson, *Physica C* **263**, 12-16 (1996).

[159] B. Khaykovich, M. Konczykowski, E. Zeldov at al., *Phys. Rev. B* **56** (2), 517-520 (1997).

[160] A.K. Pradhan, S.B. Roy, P. Chaddah et al., *Supercond. Sci. Technol.* **9**, 743-749 (1996).

[161] S. Kokkaliaris, A.A. Zhukov, P.A.J. de Groot et al., *Phys. Rev. B* **61** (5), 3655-3664 (2000).

[162] M. Werner, F.M. Sauerzopf, H.W. Weber et al., *Phys. Rev. B* **61** (21), 14795-14803 (2000).

[163] G. Blatter, M.V. Feigel'man, V.B. Geshkenbein et al., *Rev. Mod. Phys.* **66** (4), 1125-1388 (1994).

[164] V.M. Vinokur, P.H. Kes and A.E. Koshelev, *Physica C* **168**, 29-39 (1990).

[165] M.V. Feigel'man, V.B. Geshkenbein and A.I. Larkin, *Physica C* **167**, 177-187 (1990).

[166] J.M. González-Calbet, A. Badía, M. Vallet-Regí et al., *Physica C* **203**, 223-230 (1992).

[167] Y. Yamaguchi, N. Shirakawa, G. Rajaram et al., *Physica C* **361**, 244-250 (2001).

[168] S. Watauchi, H. Ikuta, H. Kobayashi et al., *Phys. Rev. B* **64**, 064520 (2001).

[169] T. Motohashi, Y. Nakayama, T. Fujita et al., *Phys. Rev. B* **59** (21), 14080-14086 (1999).

[170] T.W. Li, P.H. Kes, W.T. Fu et al., *Physica C* **224**, 110-116 (1994).

[171] S.M. Green, Yu Mei, A.E. Manzi et al., *J. Appl. Phys.* **66** (8), 3703-3709 (1989).

[172] A.R. Moodenbaugh, D.A. Fischer, Y.L. Wang et al., *Physica C* **268**, 107-114 (1996).

[173] J. Wang, M. Wakata, T. Kaneko et al., *Phyicsa C* **208**, 323-327 (1993).

[174]   R.G. Buckley, J.L. Tallon, I.W.M. Brown et al., *Physica C* **156**, 629-634 (1988).

[175]   O. Peña, A. Perrin and M. Sergent, *Physica C* **156**, 489-493 (1988).

[176]   H.M. O'Bryan, W.W. Rhodes and P.K. Gallagher, *Chem. Mater.* **2**, 421-424 (1990).

[177]   J.T. Kucera, T.P. Orlando, G. Virshup et al., *Phys. Rev. B* **46** (17), 11004-11013 (1992).

[178]   D.E. Farrell, C. M. Williams, S.A. Wolf et al., *Phys. Rev. Lett.* **61** (24), 2805-2808 (1988).

[179]   D.E. Farrell, S. Bonham, J. Foster et al., *Phys. Rev. Lett.* **63** (7), 782-785 (1989).

[180]   T.T.M. Palstra, B. Bàtlogg, L.F. Schneemeyer et al., *Phys. Rev. B* **38** (7), 5102-5105 (1988).

[181]   J.D. Hettinger, A.G. Swanson, W.J. Skocpol et al., *Phys. Rev. Lett.* **62** (17), 2044-2047 (1989).

[182]   S. Zhu, D.K. Christen, C.E. Klabunde et al., *Phys. Rev. B* **46** (9), 5576-5580 (1992).

[183]   C.M. Friend, C. Wellstood, D. Vazquez et al., *Supercond. Sci. Technol.* **16**, 65-70 (2003).

[184]   Vostner, H.W. Weber, H.C. Freyhardt et al., *IEEE Trans. Appl. Sup.* **11** (1), 2715-2718 (2001).

[185]   M. Inoue, S. Nishimura, T. Kuga et al., *Physica C* **372**, 794-797 (2002).

[186]   T. Kiss, M. Inoue, S. Nishimura et al., *Physica C* **378**, 1113-1117 (2002).

Summary

The goal of this study is to investigate the mechanisms that are responsible for the dissipation in various polycrystalline high-temperature superconductors. The importance of grain connectivity for the conductors to sustain a large supercurrent is demonstrated. The question in how far poor grain connectivity reduces the critical current density and influences its behavior in magnetic field is addressed. The location of the dissipation mechanisms is revealed and the mechanisms are studied independently.

Several techniques are applied to study the effect of the grain structure on the overall critical current of the superconducting samples. The magnetic knife technique is introduced to obtain the spatial distribution in overall critical current density of YBCO coated conductors. The critical current density shows large variations across the width of the conductor, especially in samples that are produced with pulsed-laser-deposition.

The variations in macroscopic critical current density of YBCO coated conductors are related to their grain structure by combining the magnetic knife technique and magneto-optical imaging. Flux penetration at high-angle grain boundaries and into defects is visualized with a resolution of several micrometers and correlated to variations in the microscopic critical current density. A qualitative image of the current carrying capabilities of the conductor is obtained by integrating the intensity of flux that is trapped in superconducting colonies over a length scale of several millimeters along the conductor length.

Clusters of high-angle grain boundaries and large defects reduce the critical current density on a length scale of several millimeters. Current meanders around areas with high-angle grain boundaries and defects, resulting in a component transverse to the direction of the transport current. For this reason, current is also severely limited by defects that run along the sample length.

The combination of magneto-optical imaging and the magnetic knife shows a better grain connectivity in YBCO coated conductors that are produced with metal-organic-deposition, compared to those produced with pulsed-laser-deposition. A three-dimensional YBCO layer provides a supercurrent with additional current paths to avoid clusters of high-angle grain boundaries and defects. This results in a smaller variation in critical current density across the width and along the length of the conductor.

The location of the weak links in the current path of Bi-2223 tapes is studied by visualizing the damage to the grain structure, caused by applied strain. Experiments where the decrease in critical current is measured as function of longitudinal strain show that the critical current in low field decreases faster than the critical current in high field. This indicates that weak links, where dissipation at low field occurs, are more affected by strain than well-connected grains and are therefore mechanically weak. The location of

the weak links in the current path is obtained by visualizing the damage to the grain structure, caused by longitudinal strain, with magneto-optical imaging.

Studying the effects of strain, by visualizing cracks with magneto-optical imaging, relates the production process to the grain structure of polycrystalline high-temperature superconductors. The formation of colony boundaries that run over the entire width of filaments in Bi-2223 tapes is a direct result of intermediate rolling steps during the production process. Partly-healed microcracks form mechanically weak connections over the entire width of the conductor and act as weak links in the current path.

A difference in phase formation and the absence of intermediate deformation steps in the production of Bi-2212 tapes results in the formation of colony boundaries that do not run filament-wide. This is demonstrated by much slower crack propagation where filaments in Bi-2212 tapes do not break instantly when strain is applied. Cracks propagate rather slowly over the width of the filament when the applied strain is increased.

The grain structure of YBCO coated conductors is a direct result of the grain structure of the metallic substrate. The formation of cracks is not influenced by the superconducting layer, but is entirely determined by the substrate. Longitudinal strain affects colonies and colony boundaries in a similar way, which results in a slower degradation in critical current compared to Bi-2223 tapes, when the critical strain is exceeded.

Current flow in polycrystalline high-temperature superconductors is analyzed in the viewpoint of the parallel path model, which describes two separate dissipation mechanisms that limit the critical current density. According to the model, current at low magnetic field is limited by weak links, while the current at high magnetic field is carried by a backbone of strongly-linked grains, where the current is limited by intra-granular flux motion. Although multiple current paths in parallel are present in polycrystalline high-temperature superconductors, current flow can be accurately described as two paths in parallel. This is demonstrated for the case of Bi-2223 tapes, where the model is carefully tested on several experiments and many samples.

As a first test, the critical current density of Bi-2223 tapes is scaled as function of magnetic field, for different field angles. The results show that the critical current density can only be scaled as function of magnetic field parallel to the c-axis of the grains when the contributions of both current paths are taken into account separately. The differences between both current paths become evident. The mechanism that limits the critical current density in the strongly-linked backbone changes when the temperature changed, while that of the weakly-linked network does not. As a result it is concluded that the mechanisms are located at different parts in the grain structure.

The contribution of both current paths can be physically separated by preparing a weak-link-free powder from a Bi-2223 tape. An independent analysis of the mechanisms that limit the critical current in both current paths is possible. Dissipation in the strongly-

linked backbone is the result of flux motion within the grains and can be described in good agreement with classical flux creep theory. Dissipation in the weakly-linked network does not occur in Josephson weak links that are located at high-angle grain boundaries. The power-law dependence that describes the dependence of the critical current density on magnetic field according to Josephson behavior does not apply. The good agreement between experiment and classical flux creep theory shows that dissipation occurs at low-angle grain boundaries and is the result of inter-granular flux motion.

It is demonstrated that although both dissipation mechanisms in Bi-2223 tapes occur at different locations in the grain structure, they are not completely independent. An interaction between inter-granular Abrikosov-Josephson vortices and intra-granular Abrikosov vortices is demonstrated by studying the change in pinning, due to a variation in oxygen concentration of the grains. Both mechanisms show a similar dependence on oxygen concentration, although different characteristic time scales apply. Inter-granular pinning is reduced faster than intra-granular pinning when oxygen is removed. It is concluded that oxygen is first removed from parts of the grains close to the grain boundaries. Inter-granular pinning is reduced faster due to the interaction between inter-granular flux lines with intra-granular flux lines close to the grain boundaries. For the same reason, pinning at grain boundaries is restored before pinning within the grains, after oxygen diffused back into the tape.

Inter-granular flux pinning at low-angle grain boundaries and intra-granular flux pinning within the grains determine the behavior of the critical current density of polycrystalline high-temperature superconductors in general and not only in Bi-2223 tapes. This conclusion is reached when various high-temperature superconductors are studied, ranging from studies that reveal the influence of the grain structure of YBCO coated conductors on the overall critical current density, to the observed double step in the magnetic field dependence of the critical current of Bi-2223 tapes, Bi-2212 tapes and YBCO coated conductors. Although a comparable grain structure in a large variety of polycrystalline high-temperature superconductors result in a comparable behavior of the critical current density, differences in pinning strength between conductors occur due to different intrinsic properties, such as anisotropy.

The main conclusion of the research presented here is that poor grain connectivity in granular high-temperature superconductors not only reduces the effective cross-section of the current path, but is also responsible for the degradation of the critical current at low magnetic field. The overall critical current density can be largely raised by increasing grain connectivity, but also by shifting the boundary between strongly- and weakly-coupled grains to higher angles, by using proper doping.

Samenvatting

(Summary in Dutch)

Het doel van dit onderzoek is het bestuderen van de mechanismen die de maximale stroom begrenzen in verschillende hoge-temperatuur supergeleiders. Het onderzoek richt zich vooral op de invloed van korrelgrenzen op de kritieke stroomdichtheid van de geleiders. In hoeverre wordt het gedrag van de kritieke stroomdichtheid, als er bijvoorbeeld een magneetveld wordt aangelegd, bepaald door de korrelgrenzen? Om deze vraag te kunnen beantwoorden wordt eerst gekeken waar het verlies in de geleider optreedt, voordat de afzonderlijke verliesmechanismen onder de loep worden genomen.

Verschillende technieken om het effect van de korrelstructuur op de gemiddelde kritieke stoomdichtheid van supergeleidende samples te bestuderen, worden toegepast. Het magnetische mes wordt geïntroduceerd om de ruimtelijke verdeling van de algehele kritieke stroomdichtheid in YBCO dikke film geleiders te bepalen, waarna deze vergeleken wordt met de korrelstructuur van de geleider. De resultaten laten grote variaties in kritieke stroomdichtheid over de breedte van de geleider zien, voornamelijk in samples, die met behulp van gepulste-laser-depositie gemaakt zijn.

Door de combinatie van het magnetisch mes en de magneto-optische afbeeldingsmethode worden de variaties in kritieke stroomdichtheid van YBCO dikke film geleiders gerelateerd aan hun korrelstructuur. De combinatie van beide technieken laat zien, dat een opeenhoping van slecht aaneengesloten korrels resulteert in een lokale onderdrukking van de kritieke stroomdichtheid van de geleider. Grote defecten en groepen van korrels, die onder grote hoek met elkaar verbonden zijn, reduceren de kritieke stroomdichtheid op een lengteschaal van meerdere millimeters. Stroom zoekt zich een weg langs deze korrelgrenzen en defecten, hetgeen resulteert in een magnetisch veldcomponent die loodrecht staat op de richting van de transportstroom. Om deze reden wordt de stroomdichtheid van de geleider tevens onderdrukt door defecten, die in de lengterichting van de geleider lopen.

De combinatie van de magneto-optische afbeeldingsmethode en het magnetische mes toont aan, dat er een betere verbinding bestaat tussen korrels in YBCO dikke film geleiders, die geproduceerd zijn met metallisch-organische-depositie, vergeleken met geleiders die geproduceerd zijn met gepulste-laser-depositie. Door de betere verbinding wordt een kleinere variatie in de gemiddelde kritieke stroomdichtheid gemeten. Dit resultaat wordt verklaard aan de hand van de korrelstructuur van de geleider. In een relatief dikke YBCO laag onstaat een 3-dimensionaal netwerk van parallelle

stroompaden, waardoor de superstroom gebieden met slecht verbonden korrels kan omzeilen.

De locatie van zwakke koppelingen in het stroompad van Bi-2223 tapes wordt onderzocht, door de schade die veroorzaakt wordt door rek zichtbaar te maken met behulp van de magneto-optische afbeeldingsmethode. De kritieke stroom in laag magneetveld degradeert sneller als functie van rek, dan in hoog magneetveld. De combinatie van rek en de magneto-optische techniek laat zien dat het verlies in laag veld op de grens tussen zwak-gekoppelde korrels optreedt. Deze korrelgrenzen zijn tevens mechanisch zwakker, vergeleken met de korrelgrenzen die onderdeel zijn van het stroompad dat de stroom in hoog magneetveld draagt.

De invloed van het productieproces op de korrelstructuur van granulaire hoge-temperatuur supergeleiders wordt onderzocht met de magneto-optische afbeeldingsmethode, door de effecten van rek op de korrelstructuur te onderzoeken. De tussenliggende deformatiestappen in het productieproces van Bi-2223 tapes resulteert in korrelgrenzen die over de hele breedte van de filamenten lopen. De scheuren in de korrelstructuur, die gevormd worden door deze deformatie stappen, worden maar gedeeltelijk hersteld tijdens de laatste warmtebehandelingen. De aanwezigheid van deze scheuren zorgt voor een sterk gereduceerde stroomdichtheid en een snelle afname van de stroomdichtheid als functie van rek.

De grenzen tussen goed aaneengesloten korrels in Bi-2212 tapes lopen niet over de gehele breedte van de filamenten. Dit verschil met Bi-2223 tapes is te verklaren aan de hand van verschillen in de formatie van de Bi-2212 fase en de afwezigheid van tussenliggende deformatiestappen in het productieproces. Dit wordt aangetoond door een veel langzamere propagatie van scheuren, waarbij de filamenten in Bi-2212 tapes niet onmiddellijk breken, als de axiale rek wordt vergroot.

De korrelstructuur van YBCO dikke film geleiders is een direct gevolg van het metallische substraat. Het ontstaan van scheuren wordt niet beïnvloed door de structuur van de supergeleidende laag, maar volledig door de korrelstructuur van het substraat. In de lengterichting aangelegde rek beïnvloedt de grenzen tussen goed aansluitende korrels en de korrels zelf op een identieke manier, nadat de kritieke rek wordt overschreden. Dit resulteert in een langzamere degradatie van de kritieke stroom als functie van rek, vergeleken met Bi-2223 tapes.

De verschillende verliesmechanismen die optreden in granulaire hoge-temperatuur supergeleiders worden onderzocht, nadat de invloed van korrelgrenzen op de kritieke stroomdichtheid is aangetoond. Dit onderzoek is uitgevoerd met behulp van het parallelle pad model, waarin wordt aangenomen dat twee aparte verliesmechanismen het

gedrag van de kritieke stroom bepalen. Volgens dit model wordt de stroom in een laag magneetveld gelimiteerd door zwak-gekoppelde korrels, terwijl de stroom in hoog magneetveld gedragen wordt door een snelweg van goed aaneengesloten korrels. Het verlies in het netwerk van zwak-gekoppelde korrels vindt plaats op de korrelgrenzen, terwijl in het geval van de sterk-gekoppelde korrels, het verlies in de korrels zelf optreedt.

De toepasbaarheid van het parallelle pad model op het gedrag van Bi-2223 tapes wordt gedemonstreerd aan de hand van meerdere experimentele resultaten. Het model wordt getest door de kritieke stroom van Bi-2223 tapes als functie van magneetveld te schalen, voor verschillende veldhoeken. Het resultaat laat zien, dat de kritieke stroom alleen schaalt met het magneetveld parallel aan de c-as van krisalstuctuur in de korrels, als de bijdragen van beide stroompaden los van elkaar worden behandeld. Verschillen tussen beide stroompaden komen op deze manier naar voren. Het mechanisme dat verantwoordelijk is voor het verlies in het sterk-gekoppelde pad, verandert als functie van de temperatuur. Dit is niet het geval voor het verliesmechanisme in het zwak-gekoppelde netwerk. Het verschil in gedrag toont aan, dat de verliesmechanismen in beide stroompaden zich op verschillende locaties in de korrelstructuur bevinden.

De bijdrage van beide stroompaden kan fysiek van elkaar gescheiden worden, door van Bi-2223 tapes een poeder te prepareren, dat vrij is van zwak-gekoppelde korrels. Een onafhankelijke analyse van de verliesmechanismen van beide stroompaden is op deze manier mogelijk. Verlies in het sterk-gekoppelde pad wordt veroorzaakt door fluxbeweging in de korrels en kan in goede overeenkomst beschreven worden aan de hand van klassieke fluxpinning theorie. Verlies in het netwerk van zwak-gekoppelde korrels treedt niet op in Josephson koppelingen op de grens tussen korrels, die onder grote hoek met elkaar verbonden zijn. De goede overeenkomst tussen experiment en klassieke fluxpinning theorie laat zien, dat het verlies in het zwak-gekoppelde netwerk optreedt op de grens tussen korrels, die onder kleine hoek met elkaar verbonden zijn.

De koppeling tussen de verliesmechanismen van beide stroompaden wordt onderzocht. Beide mechanismen blijken niet volledig onafhankelijk van elkaar te zijn, ook al bevinden ze zich op verschillende locaties in de korrelstructuur. De interactie tussen inter-granulaire Abrikosov-Josephson veldlijnen en Abrikosov veldlijnen in de korrels wordt aangetoond. De verandering in maximale pinningkracht, die wordt veroorzaakt door een verandering in zuurstof concentratie in de korrels, wordt bestudeerd. Beide mechanismen laten een zelfde afhankelijkheid van zuurstof concentratie zien, al zijn verschillende karakteristieke tijdschalen van toepassing. Pinning op de korrelgrenzen wordt sneller beïnvloed als de zuurstof concentratie wordt veranderd, vergeleken met pinning in de korrels. Dit wordt verklaard aan de hand van een zuurstofgradiënt in de korrels en de bestaande interactie tussen magnetische veldlijnen op de korrelgrenzen en veldlijnen die zich dichtbij de korrelgrenzen in de korrels bevinden.

Het gedrag van de kritieke stroomdichtheid in polykristallijne hoge-temperatuur supergeleiders in het algemeen wordt bepaald wordt door pinning op korrelgrenzen en pinning in de korrels zelf. Deze conclusie is gebaseerd op onderzoek aan verscheidende hoge-temperatuur supergeleiders. Het onderzoek variëert van het bestuderen van de invloed van de korrelstructuur op de algemene kritieke stroomdichtheid in YBCO dikke film geleiders, tot de observatie van een dubbele stap in de veldafhankelijkheid van de kritieke stroom in Bi-2223 tapes, Bi-2212 tapes en YBCO dikke film geleiders. Al leidt een vergelijkbare korrelstructuur in verschillende poly-kristallijne supergeleiders tot een vergelijkbaar gedrag van de kritieke stroomdichtheid, toch treden er verschillen in pinning sterkte op. Dit wordt veroorzaakt door verschillen in intrinsieke eigenschappen, zoals anisotropie, tussen de verschillende materialen.

De hoofdconclusie van dit onderzoek is dat de verbinding tussen individuele korrels in granulaire hoge-temperatuur supergeleiders niet alleen de doorsnede van het stroompad bepaald, maar ook grotendeels verantwoordelijk is voor de degradatie van de kritieke stroomdichtheid in een laag magneetveld. De kritieke stroomdichtheid kan sterk verhoogd worden door de verbinding tussen korrels te vergroten. Ook kan een verschuiving van de grens tussen zwak- en sterk-gekoppelde korrels, door bijvoorbeeld een geschikte keuze van doping, leiden tot een verhoging van de kritieke stroomdichtheid.

Acknowledgements

The realization of the dissertation lying before you would not have been possible without the support that I received from numerous people.

During my PhD, I had the fortunate opportunity to divide my time between two pleasant but also stimulating institutes; the Low Temperature Division at the University of Twente and the National High Magnetic Field Laboratory in Tallahassee, Florida. I would like to thank Herman ten Kate, for making this possible and for his support throughout the years. Justin Schwartz provided me with a very challenging work environment in Florida. I'm very thankful for his flexibility in choosing the topic of my work.

Bennie ten Haken provided me with many challenges and discussions on how to proceed with my work, not only during my stay in Twente, but also during the time I spent in Florida. It was a pleasure working with Marc Dhallé, who always found time to encourage me with new ideas. Marc, your enthusiasm about the results of my experiments is contagious. I would like to thank Bert Metz for his support while working with the magnetic knife.

I enjoyed the friendship and technical support of Hans van Eck, who even followed me to the Sunshine State. I would like to thank Huub Weijers, Ulf and Bianca Trociewitz, Lucas Naveira and Angelo Caruso for the good times we had at and around the lab in Tallahassee as well as for their scientific and technical support. They always found time for a good cup of coffee. Michael Davidson, thank you for providing me with the microscope for the magneto-optical imaging experiments.

From my colleagues in Twente I would especially like to thank Harald van Weeren, Olaf van der Meer, Arno Godeke, Laura Vargas and Jan-Jaap Rabbers for their friendship and the pleasant company at conferences. Ans Veenstra-Lokin and Inke in de Wal-Van de Werfhorst, thank you for your help with all the paperwork and for arranging the various trips I took. Harrie Steffens provided me with a constant flow of helium during the long days of experimentation.

I would also like to thank the people who expressed their interest in my work by providing me with state-of-the-art samples. Currently finishing his PhD at the NHMFL, Jianhua Su spend a lot of time synthesizing Hg-based superconductors and was always willing to let me study his best samples. Judy Wu from the University of Kansas supplied the Hg- and Tl-based films. By sending me interesting samples, Dominic Lee of Oak Ridge National Laboratory and Cees Thieme of American Superconductor Corporation are partly responsible for my growing interest in YBCO coated conductors.

Degene aan wie ik het meest te danken heb zijn mijn familie en vrienden. Mijn ouders wil ik graag bedanken voor hun steun en toeverlaat. Sandra, heel erg bedankt voor het doorlezen van de Nederlandse tekst in mijn proefschrift. Ineke, bedankt voor je vertrouwen en steun in de laatste paar jaren. Mijn vrienden van de fietsclub, schaatsclub en motorclub, wil ik graag bedanken voor de grote hoeveelheid lol die we samen hebben beleefd en voor de te gekke reizen die we hebben gemaakt. Natuurlijk ook voor de mensen die ik niet genoemd heb: BEDANKT!

Danko